Preparatory Studies for FLEX

Contributions to the radiometric calibration and the atmospheric characterization

Dissertation to obtain the academic degree
Doctor rerum naturalium (Dr. rer. nat.)

Lena Jänicke

Berlin, January 2024

Institute for Meteorology,
Radiation and Remote Sensing Group

submitted to the Department of Earth Sciences of the
Freie Universität Berlin

Selbstständigkeitserklärung

Hiermit erkläre ich an Eides statt, dass ich die vorliegende Arbeit selbstständig und ohne fremde Hilfe angefertigt, keine anderen als die angegebenen Quellen und Hilfsmittel benutzt und die den benutzen Quellen wörtlich oder inhaltlich entnommenen Stellen als solche kenntlich gemacht habe. Diese Arbeit hat in gleicher oder ähnlicher Form noch keiner Prüfungsbehörde vorgelegen.

Berlin, den 31.01.2024

_____

Lena Jänicke

Abstract

European Space Agency's (ESA's) 8th earth explorer mission, the Fluorescence Explorer (FLEX), aims to deliver the fluorescence signal emitted by terrestrial vegetation. It is planned to launch the satellite FLEX in 2025. FLEX will carry the high resolution Fluorescence imaging spectrometer (FLORIS) which has a spatial resolution of 300x300 m^2 and a swath width of 150 km. FLORIS will measure the complete fluorescence spectrum between 500 and 780 nm with a high spectral resolution between 0.3 and 3 nm. To disentangle the small fluorescence signal from the top-of-atmosphere (TOA) measurement, the sensor must be very sensitive and precise. Therefore, a good calibration and validation is necessary. Within this thesis, a validation strategy for FLORIS is developed by analysing pre-studies for the FLEX mission. Furthermore, an aerosol layer height retrieval is developed which can be extended to improve the atmospheric correction within the fluorescence retrieval.

The Sentinel-3A and -3B tandem mission of 2018 was exploited to mimic the future tandem constellation of Sentinel-3 and FLEX. The spectral bands of the Ocean and Land Color imager (OLCI) on the Sentinel-3B satellite were shifted to a comparable band setting of FLORIS. This thesis presents a transfer function that enables the comparison of the radiance data of OLCI in FLEX configuration (OLCI-FLEX) and of OLCI in the nominal configuration. The transfer function overcomes the difference in spectral resolution by transferring information about the atmosphere and the surface from the spectral high resolution instrument to the lower resolution instrument. This information is used in a radiative transfer model to simulate OLCI-A measurement. The resulting simulated measurement at the nominal OLCI bands can be compared to the original OLCI-A measurement. The satellite-satellite comparison showed sensitivity to the known systematic measurement bias and also revealed processing errors.

It was also studied how the satellite-satellite validation can be complemented by comparison of the satellite products with ground-based measurements. Ground-based instruments can be operated at low costs and with high accuracy. However, differences in spatial resolution result only in comparable signals if the surface is homogeneous. Thus, a measure for homogeneity of the surface was defined to identify the best possible ground site within a study scene by exploiting airborne measurements. The uncertainty due to differences in spatial resolution and spatial

mismatch was also quantified. For the studied case, the validation uncertainty was small within the spectral range between 720 and 800 nm. The ground-based instrument should cover at least 13.5x13.5 m^2.

The fluorescence retrieval is based on a spectral fitting method that exploits the well known structure of the oxygen absorption band at 760 nm. The depth of the absorption lines is determined by the surface pressure. Additionally, a present aerosol layer changes the depth of the lines depending on the height of the layer. Hence, the aerosol layer height is an important information for the fluorescence retrieval. A retrieval algorithm of the aerosol layer height based on OLCI measurements in the oxygen absorption band was developed. This algorithm was applied to two test cases over the ocean and for known aerosol types. The found height was comparable to results from a similar instrument, the Tropospheric Monitoring Instrument (TROPOMI). Both algorithms estimated the aerosol layer height too low compared to simultaneous measurements from an active instrument, the Cloud-Aerosol Lidar with Orthogonal Polarization (CALIOP). To extent the OLCI algorithm also for land cases, the surface reflectance must be well characterized and the aerosol type must be estimated.

All in all, this study contributes valuable information for the development of a successful validation strategy of FLEX. This strategy should include the validation of the top of atmosphere radiance data by a comparison of FLORIS and OLCI. Especially within the oxygen absorption band at 760 nm, the application of a transfer function is necessary. Large uncertainty sources of the validation with ground-based measurements were quantified and recommendations for the choice of sites are provided. Finally, a first retrieval of the aerosol layer height from OLCI could be presented. This information can be used to improve the fluorescence retrieval.

Zusammenfassung

Die 8. „Earth Explorer" Mission der Europäischen Raumfahrtagentur (ESA), der „Fluorescence Explorer" (FLEX), hat das Ziel das Chlorophyllfluoreszenzsignal zu messen, welches von Pflanzen an Landoberflächen emittiert wird. Der Satellit soll voraussichtlich 2025 in seine Umlaufbahn gebracht werden. FLEX wird ein hochauflösendes, abbildendes Spektrometer, das „Fluorescence Imaging Spectrometer" (FLORIS), tragen, welches eine räumliche Auflösung von 300x300 m^2 und eine Schwadbreite von 150 km hat. FLORIS deckt den Wellenlängenbereich von 500 bis 780 nm ab. Die Kanäle haben eine Breite zwischen 0.3 und 3 nm. Damit kann FLORIS das gesamte Chlorophyllfluoreszenzspektrum erfassen. Um das kleine Fluoreszenzsignal vom Gesamtsignal unterscheiden zu können, muss FLORIS sehr empfindlich sein und eine hohe Messgenauigkeit haben. Dafür ist eine gute Kalibration und Validation nötig. Anhand von Vorstudien wird in dieser Arbeit eine Validationsstrategie für FLORIS entwickelt. Zusätzlich wird ein neu entwickeltes Fernerkundungsverfahren zur Bestimmung der Aerosolschichthöhe vorgestellt, welches in angepasster Form für die Atmosphärenkorrektur zur Bestimmung des Fluoreszenzsignals genutzt werden kann.

Die Tandemmission von Sentinel-3A und -3B im Jahr 2018 wurde genutzt, um die zukünftige Tandemkonstellation von Sentinel-3 und FLEX zu testen. Die Positionen und Breiten der spektralen Kanäle des Spektrometers „Ocean and Land Color Imager" (OLCI) an Bord des Satelliten Sentinel-3B wurden so verändert, dass seine Kanäle den Kanälen von FLORIS ähneln. Diese Arbeit präsentiert eine Transferfunktion, die es ermöglicht, die Messung von OLCI-B in der FLEX-Konfiguration und die Messung von OLCI-A zu vergleichen, trotz spektraler Unterschiede zwischen den Messungen. Eigenschaften der Atmosphäre und des Erdbodens, die aus der hoch aufgelösten Messung (OLCI-FLEX) bestimmt werden, werden zu den spektralen Stützstellen von OLCI-A transferiert. Diese transferierten Informationen werden in einem Strahlungstransportmodell genutzt, um Messungen von OLCI-A zu simulieren. Diese können mit der originalen OLCI-A Messungen verglichen werden. Der Vergleich der Datensätze aus der Tandemmission bestätigte bereits bekannte Unterschiede zwischen OLCI-A und OLCI-B. Zusätzlich konnten Hinweise für Fehler in der Prozessierung der OLCI-FLEX Daten gefunden werden.

Es wurde untersucht inwiefern die Satellit-Satellit-Validation mit einem Vergleich von Satelli-

tendaten mit Bodenmessungen komplementiert werden kann. Bodengestütze Messinstrumente können mit geringen Kosten und hoher Genauigkeit betrieben werden. Dafür können aber Unterschiede in der räumlichen Auflösung zu großen Unterschieden im Signal führen, wenn der beobachtete Boden nicht homogen ist. Basierend auf flugzeuggestützten Messungen, wurde ein Maß für die Homogenität der Erdoberfläche definiert. Für eine Fallstudie wurde ein bestmöglicher Standort für eine Bodenmessung identifiziert. Außerdem wurde die Unsicherheit der Validation bestimmt, die durch die Unterschiede in der räumlichen Auflösung sowie den räumlichen Versatz der Messungen entstehen. Für die gefundene Messstation waren diese Unsicherheiten nur im Wellenlängenbereich zwischen 720 und 800 nm klein. Außerdem sollte das Bodenmessinstrument eine Abdeckung von mindestens 13.5x13.5 m^2 haben.

Die Fluoreszenzbestimmung für FLORIS basiert auf einer spektralen Fit-Methode, welche die bekannte Struktur der Sauerstoffabsorptionsbänder bei 760 nm ausnutzt. Die Tiefe dieser Absorptionsbänder hängt vom Bodendruck ab. Außerdem beeinflusst die Höhe der Aerosolschicht die Tiefe der Absorptionslinien. Daher ist die Aerosolhöhe eine wichtige Größe, um das Fluoreszenzsignal richtig zu bestimmen. Es wurde ein Algorithmus entwickelt, um die Aerosolhöhe aus OLCI-Messungen abzuleiten. Dieser Algorithmus wurde an zwei Szenen über dem Ozean getestet, bei denen der Aerosoltyp bekannt war. Die bestimmten Höhen waren vergleichbar zu gleichzeitigen Messungen von einem ähnlichen Instrument, dem „Tropospheric Monitoring Instrument" (TROPOMI). Sowohl die Aerosolhöhe von OLCI als auch von TROPOMI waren niedriger als die Höhe, die von dem aktiven Instrument, dem „Cloud-Aerosol Lidar with Orthogonal Polarization" (CALIOP), gemessen wurde. Für die Anwendung des Algorithmus für FLEX muss dieser für Landoberflächen angepasst werden. Hierfür benötigt man die spektralen Eigenschaften des Erdbodens sowie die des vorliegenden Aerosoltyps.

Alles in allem liefert diese Arbeit wichtige Beiträge zur Entwicklung einer Validationsstrategie für FLEX. Diese Strategie sollte die Validation der Strahlungsdaten beinhalten. Für den Vergleich von FLORIS mit OLCI ist eine Transferfunktion für die Kanäle in der Sauerstoffabsorption bei 760 nm notwendig. Für die Validation der abgeleiteten Bodenreflektanz mit Hilfe von Bodenmessungen wurden große Unsicherheiten quantifiziert. Auf dieser Studie basierend, konnten Empfehlungen für die Wahl eines geeigneten Standortes formuliert werden. Zusätzlich konnte ein erstes Fernerkundungsverfahren zur Bestimmung der Aerosolhöhe aus OLCI-Daten vorgestellt werden. Diese Information kann die Fluoreszenzbestimmung verbessern.

Contents

1

Introduction

1.1 Scientific motivation

Climate change is driven by anthropogenic carbon dioxide (CO_2) emission [Calvin et al., 2023]. The increasing amount of greenhouse gases including CO_2 already led to a warming of the global surface temperature in 2011-2020 by 1.1°C compared to 1850-1900 [Calvin et al., 2023]. In 2015, 196 nations agreed to restrict the warming to 1.5°C in the Paris climate agreement [UN-FCCC, 2016]. Nevertheless, the reduction of CO_2 emissions is currently too slow [Calvin et al., 2023] as people cannot overcome social, economic and technical problems fast enough. Besides the emission of CO_2 by burning fossil fuels, the change of land-use by humans is the second largest anthropogenic source of CO_2 emission [Le Quéré et al., 2009]. In 2018, one quarter of greenhouse gas emission was due to land-use changes [Lamb et al., 2021]. This change of land-use includes e.g. deforestation [Le Quéré et al., 2009] and drainage of wetlands [Laine et al., 2019].

To assess the development of CO_2 content in the atmosphere, the carbon cycle must be observed on a global scale. The carbon cycle describes the uptake and emission processes of the different subsystems of the earth as shown in Figure 1.1. Carbon cannot be removed from the system, instead it undergoes a constant cycle of storage and emission which must be balanced for a constant earth temperature. Sources are either anthropogenic like burning of fossil fuels, agriculture and deforestation, or natural like soil, or volcanoes. Sinks are the oceans and their biomass and the terrestrial biosphere. Plants fix CO_2 during photosynthesis by transforming photon energy and CO_2 in sugars and oxygen.

The terrestrial biosphere is highly variable. With increasing temperature, the growing season is extended and more CO_2 can be up taken. On the other hand, extreme events like droughts, winds and fires, which are caused by the global warming reduce the uptake of CO_2 [Reichstein et al., 2013]. The stress due to the global warming affects not only large ecosystems but also agricultural fields which leads to crop failures as observed e.g. in the US [Kim and Mendelsohn, 2023]. Thus, food security is reduced by global warming [Calvin et al., 2023]. Food security is the second of the 17 United Nation's sustainability goals. However, its current status of achievement is "far from target" with negative trend [Miranda et al., 2023]. Hence, for estimating the climate change effects and observing them on the environment and humans security, global monitoring
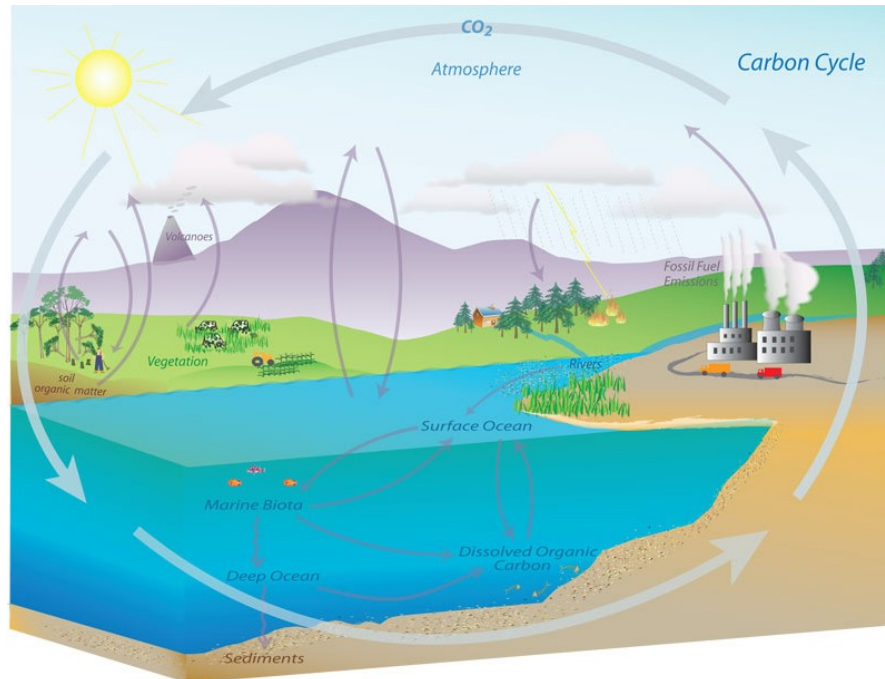
Figure 1.1   Illustration of carbon cycle taken from National Oceanic and Atmospheric Administration (NOAA) [2019]

of the terrestrial biosphere is important [Sellers et al., 2018]. Anderson et al. [2017] also stated that earth observation plays an important role for achieving the sustainability goals.

Plant activity can be monitored measuring the fluorescence signal. The fluorescence signal is a byproduct of photosynthesis. Energy, that is not used by the photo cycles, is partly emitted as fluorescence signal. Thus, it can serve as proxy for plant stress [Ač et al., 2015]. Stressed plants can be early detected by monitoring the fluorescence signal on a global scale with high spatial resolution [Campbell et al., 2008]. This allows for the timely implementation of counteractions. Such fluorescence signal observations could provide valuable information to detect and mitigate plant stress and therefore improve food security [Drusch et al., 2017].

One possibility for a global fluorescence observation will offer the Fluorescence Imaging Spectrometer (FLORIS), carried by the Fluorescence Explorer (FLEX) satellite operated by the European Space Agency (ESA) [Coppo et al., 2017, Drusch et al., 2017]. FLORIS is a high resolution spectrometer, that covers the spectral range between 500 and 780 nm with very high spectral resolution between 0.3 and 3 nm and a spatial resolution of 300x300 m^2. It aims to retrieve the complete fluorescence spectrum between 650 and 780 nm with peaks at 685 and 740 nm (see Figure 2.2) [Drusch et al., 2017, Kraft et al., 2012]. This information can offer further insight in photosynthesis. However, the retrieval of the fluorescence signal is extremely challenging as the signal is very small. At ground, the maximum fluorescence peak is approximately 2.5 $mWm^{-2}sr^{-1}nm^{-1}$ which is only 10–25% of the apparent surface reflectance at 685 nm and 2–6% at 740 nm [Campbell et al., 2008].

The instrument and in particular, its optical performance must be well characterized to enable the retrieval of the fluorescence signal [Nuzzi et al., 2023]. This characterization is realised by

several calibration and validation approaches. In-flight calibration and validation can be done by inter-comparison with other instruments on different platforms either by satellite-satellite, satellite-airplane or satellite-ground-based comparisons. Each of those validation strategies has its challenges and limitations, which are studied and partly resolved in this thesis.

The comparison of measurements from two satellite sensors for validation purpose is facilitated if those sensors observe a target under the same environmental conditions with the same geometry and the same spectral characterization. However, due to high costs of satellite missions, only few identical instruments are in space. One example is Sentinel-3. The two identical satellites, Sentinel-3A and -3B, flew in tandem constellation for four months in 2018. This constellation was very valuable for direct comparison of the instruments [Clerc et al., 2020, Lamquin et al., 2020]. The tandem constellation allowed the observation of the same target within 30 s. A similar constellation is planned for the FLEX mission with Sentinel-3 as tandem partner [Drusch et al., 2017]. Both, the Ocean and Land Color Imager (OLCI) on Sentinel-3 and FLORIS on FLEX have a similar spatial resolution but a different spectral characterization. By observing different parts of the spectrum with different spectral response functions, each instrument measures a different top-of-atmosphere (TOA) radiance even if observing the same target under the same environmental conditions. A transfer function to overcome the difference in spectral resolution was developed and applied in this thesis. One advantage of such comparison is the high number of sampling points which allows a robust statistical evaluation of measurement uncertainties. However, the measurements of neither instrument can be treated as reference standard measurement because they cannot be calibrated after the launch under laboratory conditions.

The comparison with airborne or ground-based measurements could close this gap, as in both cases instruments can be used whose calibration can be monitored under laboratory conditions. Overpasses with aeroplanes allow measurements of similar spatial resolutions to the satellite measurements. However, high operational costs limit the temporal resolution and thus, the number of simultaneous observations from aeroplane and satellite. In contrast, ground-based instruments can be operated constantly with low costs. Satellite and ground-based setups measure different signals as the light measured at the satellite has travelled one more time through the atmosphere than the light measured at the ground. The effect of the atmosphere can be corrected if the atmosphere is well characterized. A comparison between ground- and satellite-based measurements is only possible under cloud-free conditions which limits the number of match-ups. A major source of uncertainty is the difference in spatial resolution. Ground-based instruments detect only a signal from a small area whereas the satellite sensor measures an averaged signal over a larger area. This difference in signal must be quantified to enable validation of satellite measurements with ground-based instruments. In this thesis, the effect of difference in spatial coverage was quantified for a study case.

For the validation with ground-based or airborne measurements, the atmospheric correction is important. It is also crucial for the fluorescence retrieval from satellite measurements. Only with a well defined atmosphere, the signal originating from ground and from atmosphere can be disentangled [Cogliati et al., 2019]. Information about gas absorption and aerosol interaction is necessary for the atmospheric correction [Sabater et al., 2017]. The aerosol interaction depends

on the microphysical and optical properties of the aerosol. Within the oxygen absorption band, which serves as main input for the fluorescence retrieval, the height of the aerosol particles influences the signal. A method of retrieving the aerosol height from OLCI on Sentinel-3 was proposed. This information could be used in future for the atmospheric correction of FLEX to improve the fluorescence retrieval.

1.2 Aims and objectives

This thesis is a preparatory study for the FLEX mission. It focuses on the validation of the TOA radiance using satellite to satellite comparison as well as satellite to ground comparison. Additionally, a retrieval of the aerosol layer height from OLCI is developed to optimize the atmospheric correction for the fluorescence retrieval from FLEX.

This thesis evolved from an ESA project called "Sentinel3 FLEX Tandem Processing Experiment". The objectives of this project were the processing and evaluation of data from the Sentinel-3A and -3B tandem phase [ESA, 2021b]. As preparation for the FLEX mission, OLCI-B was reprogrammed to mimic FLORIS. Thus, a first set of real data is available for FLEX like experiments. Within the project, we delivered auxiliary data for the radiometric calibration, made consistency checks of the data set of OLCI-A, and OLCI-B in FLEX configuration and established a validation approach for this data which can be adapted for the future FLEX mission. While working on those topics, the following research questions arose which are answered within this thesis.

1. How can two TOA measurements from sensors with different spectral characteristics be compared?

2. Is there a systematic difference of the radiometry between OLCI-A and OLCI-FLEX?

3. Which surface and atmospheric parameters are necessary for an adequate description of the radiative transfer at wavelengths between 500 and 780 nm to enable comparison of sensors with different spectral response?

4. How do spatial resolution and geolocation mismatch compromise the comparison of ground truth and satellite surface reflectance measurements?

5. Is it possible to estimate the aerosol layer height from OLCI O_2A bands over ocean and how large is the uncertainty?

1.3 Thesis structure and author's contribution

This thesis is structured in six chapters. The current Chapter 1 motivates the scientific work and presents the structure of the thesis. Chapter 2 gives background information of the topic. The scientific work is presented in the Chapters 3-5. Chapter 3 describes the intercomparison

of radiances measured by two satellite sensors in tandem constellation with same spatial resolution but different spectral characteristics. Chapter 4 outlines a pre-study for validation comparing satellite retrievals of the surface reflectance with ground-based measurements. This study includes the selection of a optimal site for the ground-based measurements and the quantification of validation uncertainties due to surface heterogeneity within a test scene. Chapter 5 presents a first application of an aerosol layer height retrieval for ocean cases from OLCI's oxygen absorption bands. Those three chapters are closed and independent publications. Hence, some redundant information might occur. General information might be elaborated both in those chapters as well as in Chapter 2. Chapter 3 and 5 are published in peer-reviewed scientific journals and Chapter 4 is published in a revised version to such journal. In Chapter 6, the results from the studies are discussed and set in relation. The author's contribution to the different publications is the following:

Chapter 3: OLCI A/B tandem phase: Evaluation of FLEX like radiances and estimation of systematic differences between OLCI-A and OLCI-FLEX
Authors: Lena Katharina Jänicke, Rene Preusker, Marco Celesti, Marin Tudoroiu, Jürgen Fischer, Dirk Schüttemeyer, and Matthias Drusch
Status: *published*
DOI: `https://doi.org/10.5194/amt-16-3101-2023`

The idea of developing a transfer function was devised by J. Fischer, R. Preusker and L. Jänicke. L. Jänicke developed and implemented the approach. It is based on look-up tables (LUTs) of radiative transfer simulations by a matrix operator model (MOMO). All input parameters and variables were set and the simulations were run by L. Jänicke. The software of the 1D variational approach and the temporal evolution model of the spectral response were provided by R. Preusker. The OLCI-FLEX data was provided by the ESA. M. Celesti adjusted the level-1 processing for the OLCI-FLEX configuration based on auxiliary data processed by R. Preusker. OLCI-A and AERONET data were acquired by L. Jänicke. The data processing, application of the 1D variational approach including optimizing it, data analysis with the generation of all figures and the writing of the manuscript was done by L. Jänicke. The section about the linear interpolation was partly written by R. Preusker. L. Jänicke, R. Preusker and J. Fischer contributed to the interpretation of the results. L. Jänicke, R. Preusker, M. Celesti, M. Tudoroiu, J. Fischer, D. Schüttemeyer, and M. Drusch contributed to the study with fruitful discussions.

Chapter 4: Identification of an optimal ground-based validation site for FLEX and quantification of uncertainties using airborne HyPlant data - A case study in Italy
Authors: Lena Katharina Jänicke, Rene Preusker, Jürgen Fischer
Status: *published*
DOI: `https://doi.org/10.1016/j.srs.2024.100155`

The idea and the concept of the study was developed by L. Jänicke supported by R. Preusker and

J. Fischer. The HyPlant surface reflectance data were provided by ESA. The data processing, analysis and presentation was done by L. Jänicke. The manuscript was written by L. Jänicke and revised by R. Preusker and J. Fischer. All authors contributed to the interpretation of the results.

Chapter 5: Estimation of Aerosol Layer Height from OLCI Measurements in the O_2A-Absorption Band over Oceans
Authors: Lena Katharina Jänicke, Rene Preusker, Nicole Docter, Jürgen Fischer
Status: *published*
DOI: `https://doi.org/10.3390/rs15164080`

The idea of implementing an aerosol layer height retrieval for OLCI was developed by J. Fischer, R. Preusker and L. Jänicke. L. Jänicke implemented and optimized the retrieval. The underlying LUTs were built by L. Jänicke after running MOMO radiative transfer simulations. The aerosol models were provided by N. Docter. R. Preusker provided software of the 1D variational approach, the temporal evolution model of the spectral response and the harmonization. L. Jänicke selected the case study scenes and acquired OLCI, TROPOMI and CALIPSO data from open-source platforms. The data processing, data analysis, generation of figures and the writing of the manuscript was done by L. Jänicke. The harmonization method was described by R. Preusker. The strategy of estimating the uncertainty was developed by R. Preusker and L. Jänicke. R. Preusker and J. Fischer supported L. Jänicke by the data interpretation and the review process.

2
Fundamentals

2.1 Remote sensing of the earth system

Remote sensing is the observation of a target from distance (e.g. Earthdata NASA [2019]). Remote sensing of the earth system includes studies of its five subsystems, namely the atmosphere, biosphere, cryosphere, geosphere and hydrosphere. This thesis contributes to the investigation of the atmosphere and the biosphere. The observation from distance can be realized by sensors mounted on ground-based, airborne or satellite platforms. Remote sensing measurements can be classified in 1) active and 2) passive remote sensing.

1) Active remote sensing instruments emit a signal and detect its response. Examples are light detection and ranging instruments (LIDAR) and radio detection and ranging instruments (RADAR). LIDARs emit a laser beam pointing to the target and measure the reflected beam [Efremenko and Kokhanovsky, 2021, p.2]. The reflected beam is characterized by the time between emission and detection, the polarization and the spectral information. Depending on the wavelength of the laser, different information can be retrieved. The light of the Cloud-Aerosol LIDAR with Orthogonal Polarization (CALIOP) on the Cloud-Aerosol LIDARs and Infrared Pathfinder Satellite Observation (CALIPSO) satellite is reflected by aerosol and cloud droplets [Winker et al., 2009]. From the time between sent and captured signal, the distance to those particles can be calculated and thus, vertical profiles of clouds and aerosol can be estimated. The depolarization is used to distinguish spherical and non-spherical particles. LIDARs can be also used for estimating the wind speed by analyzing the spectral Doppler shift (e.g. ESA's Aeolus mission [Reitebuch, 2012]).

2) Passive remote sensing instruments measure the reflected solar radiation and the emitted thermal radiation from the earth system. The radiation is measured at different wavelengths. Such measurements can be conducted e.g. by imaging spectrometry (e.g. with OLCI, or the TROPOspheric Monitoring Instrument (TROPOMI)).

Either kind of those instrument types can be mounted on a geo-stationary satellite or a sun synchronous polar orbiting satellite. The geo-stationary satellites follow the rotation of
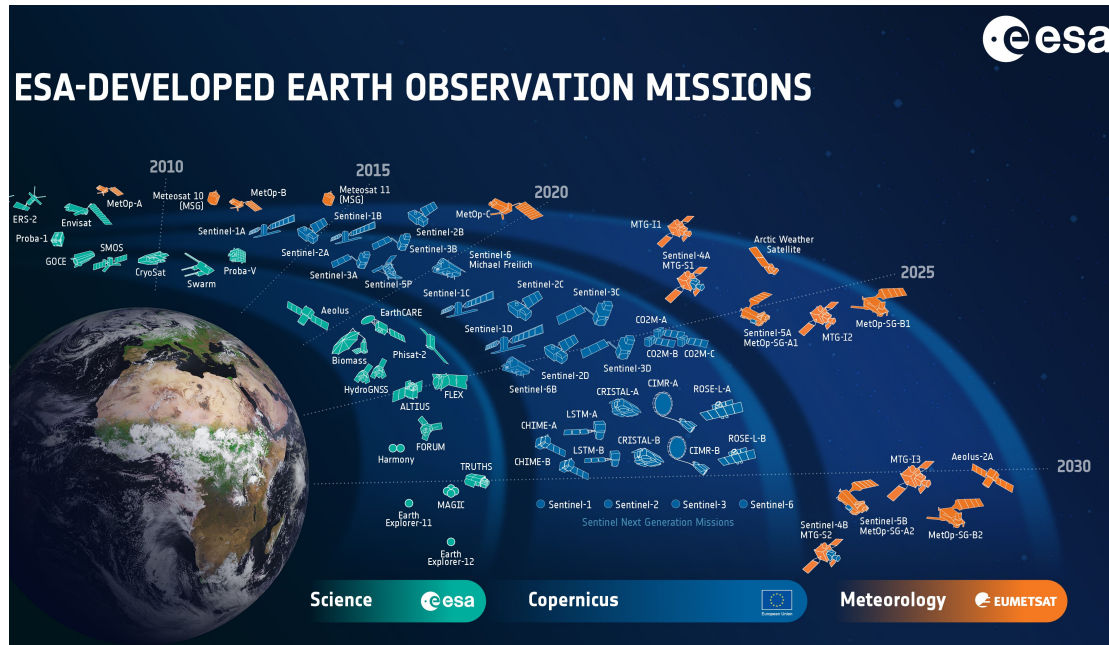
Figure 2.1   Past and future ESA earth observation satellite missions, taken from ESA [2023b]

the earth. Hence, they observe always the same area with high temporal resolution, which is important for weather forecasts. Sun synchronous satellites observe the same point on earth at same solar time. They have a constant orbit from pole to pole while the earth rotates. This constellation delivers a global coverage but with limited temporal resolution. The temporal resolution is determined by the swath and environmental conditions like cloud coverage. However, observations from satellite can fill the lack of data from remote places like the Arctic, oceans or sparsely populated areas [Petty, 2006, p.8], [Efremenko and Kokhanovsky, 2021].

The first satellite in space was Sputnik 1 launched in 1957 which was the starting point for remote sensing from satellite [Tatem et al., 2008]. Since then, the earth observing satellite fleet is constantly increasing and advancing. NASA [2022] counts in total 1720 space crafts in the field of earth sciences. ESA develops and operates numerous earth observing satellite missions which are shown as an overview in Figure 2.1. ESA's earth observation missions can be categorized in two groups: 1) the operational missions and 2) the scientific missions. Operational missions include the Copernicus program (see Section 2.1.2) and satellites that collect meteorological data. Those missions deliver quality controlled high level data which are used by society and science on a daily basis e.g. for air quality assessments, sea surface temperature determination, wild fire monitoring, sea level height observation, etc. The scientific missions, including the Earth Explorers, host scientific experiments to answer recent research questions [ESA, 2023a, 2015].
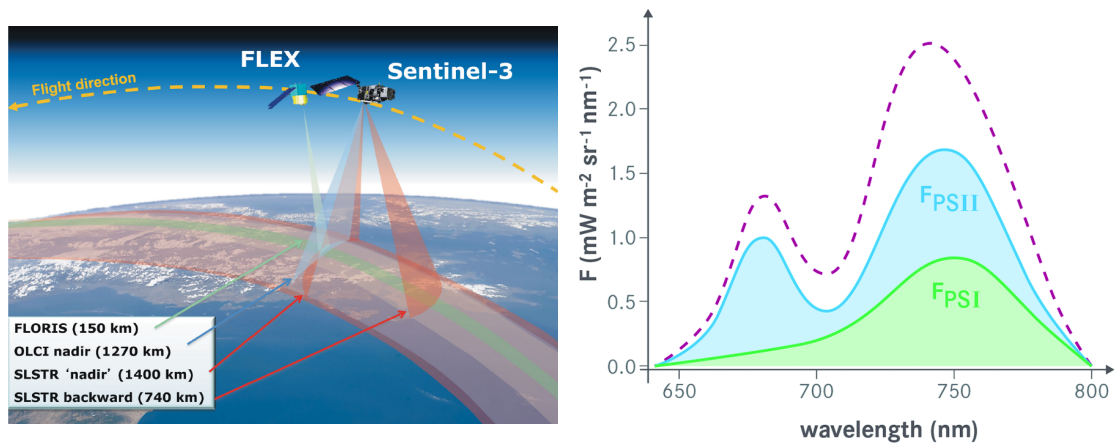
Figure 2.2   Left: Schematic overview of tandem constellation of FLEX and Sentinel-3; right: full fluorescence spectrum. Both images are taken from Drusch et al. [2017].

2.1.1 Fluorescence Explorer

The Fluorescence Explorer (FLEX) is part of the Earth Explorer fleet of ESA. FLEX will carry a spectrally high-resolution imaging grating spectrometer called Fluorescence Imaging Spectrometer (FLORIS) which covers the visible spectral range between 500 and 780 nm with a spectral resolution between 0.3 and 3 nm [Coppo et al., 2017]. From those TOA radiance measurements, the complete fluorescence spectrum emitted by plants on the earth surface will be retrieved [Drusch et al., 2017]. The fluorescence spectrum with its two peaks of light emitted during photo cycle 1 and photo cycle 2 is shown in Figure 2.2. The goal of the FLEX mission is to increase the understanding of photosynthesis, the carbon cycle and to support agricultural management and food security on a global scale [ESA, 2020b]. FLORIS has a spatial resolution of 300 x 300 m^2 and a swath width of 150 km. It will be on a sun synchronous orbit with a repeat cycle of 27 days [Drusch et al., 2017].

FLEX will fly in tandem constellation with Sentinel-3 (S3) observing the same targets within 6 to 15 s (see Figure 2.2). Two instruments on S3, namely OLCI and Sea and Land Surface Temperature Radiometer (SLSTR), provide information about the atmosphere which is used for the atmospheric correction of FLORIS [Sabater et al., 2014]. Especially, aerosol properties and the water vapour content affect the signal within the spectral range of FLORIS. They must be corrected to disentangle the signal that originates from the surface and the one from the atmosphere. Once the atmosphere is characterized, the surface reflectance can be retrieved and the fluorescence signal can be estimated. One method of estimating SIF is the Spectral Fitting Method (SFM) [Cogliati et al., 2019]. The SFM provides surface reflectance information and the full fluorescence spectrum. It is based on a radiative transfer model of the atmosphere (MODerate resolution atmospheric TRANsmission (MODTRAN)) and a model of the processes in the canopy (Soil Canopy Observation of Photosynthesis and Energy fluxes model (SCOPE)). The top-of-canopy (TOC) radiance is defined as sum of reflected light and the fluorescence signal. It is optimized in an iterative process based on a non-linear least square technique which searches

the minimum of a cost function. In total, 26 parameters are retrieved: 8 parameter characterizing the fluorescence spectrum and 18 describing the surface reflectance.

2.1.2 Sentinel-3

The European Union, the ESA and the European Organisation for the Exploitation of Meteorological Satellites (EUMETSAT) established a joint initiative to deliver high quality, open-access earth observation data from satellite and in situ measurements [Donlon et al., 2012]. This initiative is called Copernicus program (former Global Monitoring for Environment and Security (GMES)) [Copernicus, 2023a]. The data are freely available to the public and serve to inform, warn, answer open questions about the earth system and support policy. The core of the program are the services which provide processed data and information addressing the main society challenges:

1. Copernicus Marine Environmental Monitoring Service (CMEMS) provides warnings, forecasts about the oceans, monitoring of the evolution of state of the ocean such as ocean surface topography, sea surface temperature, ocean colour, sea ice condition [CMEMS, 2021, Donlon et al., 2012].

2. Copernicus Land Monitoring Service (CLMS) provides daily monitoring of land surfaces (e.g. water, soil, terrestrial pollution,...), land cover characteristics, bio physical vegetation parameters, active fires, burned areas, lakes, rivers, surface temperature [ESA, 2021a, Donlon et al., 2012]

3. Copernicus Atmospheric Monitoring Service (CAMS) determines and the monitors atmospheric composition [Donlon et al., 2012, ECMWF, 2021, Peuch et al., 2022]

4. Copernicus Emergency Management Service (CEMS) warns about and manages crisis situations like natural disasters and humanitarian crises [Copernicus, 2021b].

5. Copernicus Security Service (CSS) addresses Europe's security challenges e.g. maritime surveillance [Copernicus, 2021c].

6. Copernicus Climate Change Service (C3S) provides information about present, past and future climate [Copernicus, 2021a].

The satellite data about the earth atmosphere and surface are mainly collected by the Sentinel fleet with currently seven satellites in orbit, namely Sentinel-1, Sentinel-2, Sentinel-3A and Sentinel-3B, Sentinel-4, Sentinel-5P, and Sentinel-6 [ESA, 2023c]. Within this thesis, data from Sentinel-3 are used. S3 is designed as successor of the Environmental Satellite (ENVISAT) which carried the Advanced Along-Track Scanning Radiometer (AATSR) to estimate the sea surface temperature, the Medium Resolution Imaging Spectrometer (MERIS) for observations of ocean color and land reflectances, and the Radar Altimeter-2 (RA-2) to measure the topography [Donlon et al., 2012]. S3 carries updated and improved versions of those instruments:
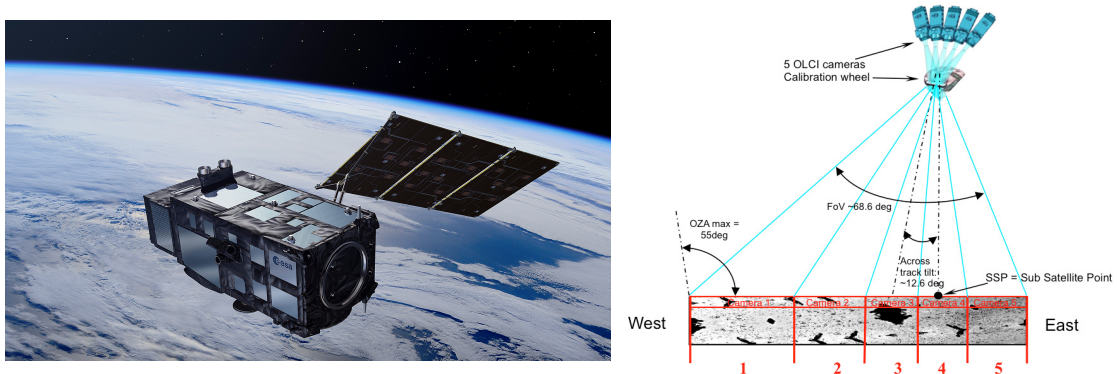
Figure 2.3   Left: Sentinel-3 satellite in orbit, taken from ESA and Carril [2023]; right: Schematic overview of OLCI's cameras and their observation angles taken from Neneman et al. [2020].

two instruments determining the altimetry (SRAL Radar altimeter and a microwave radiometer), OLCI, and SLSTR. A picture of S3 is shown in Figure 2.3. The two primary objectives of S3 are measuring the topography and providing visible and infrared measurements of land and ocean surface and atmosphere [Donlon et al., 2012]. Those data must satisfy high standards of quality and must be associated with quantified uncertainties to ensure consistency with EN-VISAT data. S3 delivers not only ocean data but contributes important information to CAMS. Each S3 satellite has a life time between 7 and 12 years. ESA plans at least four different S3 versions (S3A-S3D). Hence, a data record from S3 of at least 20 years is envisioned [Donlon et al., 2012]. Together with ENVISAT's data record of 10 years [Dragani et al., 2015], at least 30 years of data observing the earth system will be available for climate observations and other scientific analysis. However, due to the interruption of communication with ENVISAT in 2012, there is a data gap of 4 years between ENVISAT and S3. For continuity among the S3 fleet and for high spatial coverage, S3A and S3B are simultaneously in orbit. S3A was launched in February 2016, S3B in April 2018. Both satellites are in the same sun synchronous orbit with an altitude of 814.5 km, a local equatorial crossing time of 10:00 a.m. and an inclination of 98.65 degrees. S3A and S3B are placed 140 degrees apart of each other [Fernández, 2016]. Between June and October in 2018 during the commissioning phase of S3B, S3A and S3B flew in tandem constellation observing the same geographic targets under the same environmental conditions. This constellation enabled a comparison between the instruments on board of the two satellites to ensure a seamless continuity [Lamquin et al., 2020, Clerc et al., 2020].

OLCI delivers the optical measurements to fulfil S3 mission goals. From the observation of ocean and land surfaces, information of the surface temperature, surface reflectance and vegetation can be retrieved. Additionally, atmospheric parameters like the aerosol optical thickness can be estimated from OLCI measurements. OLCI is built of 5 identical cameras which enable simultaneous measurements within 21 bands between 400 and 1020 nm across a swath of 1270 km. The cameras are tilted westwards with nadir view at camera 4 to reduce the effect of sun glint (see Figure 2.3) [Donlon et al., 2012]. The highest possible spectral resolution is 1.25 nm. The separation of the light into the different wavelengths is realised by a concave

Figure 2.4   Left: Example aeroplane as measurement platform for HyPlant (Cessna Grand Caravan C208B Aircraft) taken from ESA [2020a]; right: image of HyPlant instrument with A pointing at the DUAL module, B at the FLUO module and C at the GPS/INS unit taken from Siegmann et al. [2019].

grating. The dispersed image is directed through an entrance slight on a charge-coupled device (CCD) array. The smallest pixel cover an area of 300x300 m^2 at nadir. With a satellite repeat circle of 27 days and two S3 satellites simultaneously in orbit, OLCI-A and -B achieve a revisiting of ocean pixels within 2 days.

OLCI can be operated in different modes with programmable band distribution. The calibration mode is executed regularly for spectral and radiometric calibration. For the calibration, OLCI is equipped with different diffuser plates. During the calibration mode, 46 micro bands are used as output. The level 1 (L1) output of the nominal operational mode are top of atmosphere radiances at 21 bands which are realised by binning the micro bands. The highest spectral resolution of the binned bands is 2.5 nm. During the commissioning phase of S3B, the programmable calibration mode of OLCI was used to mimic FLORIS measurements to develop a validation strategy. The data are evaluated in Chapter 3.

2.1.3 High-Performance Airborne Imaging Spectrometer

The High-Performance Airborne Imaging Spectrometer (HyPlant) is operated on an airplane (e.g. Figure 2.4) for the retrieval of surface information including SIF [Rascher et al., 2015, Siegmann et al., 2019]. It is built of two modules called DUAL and FLUO (see Figure 2.4). The DUAL module is built of two pushbroom imaging line scanners covering the spectral ranges between 373.6-975.3 nm and 980.49-2504.64 nm [Siegmann et al., 2019]. Within the visible spectral range, this sensor has a spectral sampling of 1.7 nm and a full width at half maximum (FWHM) of 3.65 nm. The signal-to-noise ratio of wavelengths between 500 and 800 nm is 510. The instrument was developed by Forschungszentrum Jülich in cooperation with Specim Ltd. (Oulu, Finland). The processing chain of the measurements includes georeferencing, radiometric calibration, atmospheric correction and the calculation of TOC radiance and reflectance as well as several reflectance indices and fluorescence maps [Siegmann et al., 2019]. The atmospheric correction is done with a commercial software called Atmospheric and Topographic Correction algorithm (ATCOR).

The spatial resolution of HyPlant depends on the flight height, the ground speed and the integra-

tion time. The field of view of one pixel is 0.084^o. The data used in this thesis were measured at a flight height of 3050 m and the pixel size was 4.5x4.5 m^2.

2.1.4 Calibration

Calibration of an imaging spectrometer is the quantification of the spectral response to a known signal input of an instrument [Goldberg et al., 2011], which enables to convert the raw signal (level 0) into radiometric units (level 1). For spaceborne instruments, calibration efforts are challenging as no direct interaction with the instruments is possible and laboratory conditions cannot be achieved. A valid characterization and uncertainty estimate is necessary when putting different measurements in relation [Goldberg et al., 2011, Niro et al., 2021]. Due to the limited life time of satellites, a combination of different instruments is needed to evaluate long time series. Changes in the climate can only be detected and quantified correctly with well calibrated instruments [Chander et al., 2013b]. An inter-calibration among satellites is necessary when the combination of those instruments is used to obtain high spatial and temporal resolution [Chander et al., 2013a, Niro et al., 2021]. Different instruments on one satellite are also used in synergy to increase the information content of their measurements. The synergy of data needs high consistency of the data which is ensured by onboard calibration or vicarious approaches [Thome et al., 2003]. Those approaches are necessary in addition to ground-based laboratory calibration efforts before launch, as harsh conditions during launch and the degradation due to radiation and space environment may change the characteristics of the instruments [Goldberg et al., 2011, Hewison et al., 2020]. Three main calibration activities are:

1) Radiometric calibration

The radiometric response is characterized including a relative and an absolute radiometric calibration. The relative calibration ensures that the signals among the bands are radiometrically consistent. Additionally, the absolute radiometric calibration characterizes the absolute values of each band. The relative and absolute uncertainty thresholds are defined in mission requirements documents. The radiometric signal is influenced by the instrument's dark current, noise and stray light.

2) Spectral calibration

For the interpretation of the radiometric data, an accurate description of the spectral response function including the position of the central wavelength and the width of the band is necessary. In orbit, the spectral characterization can be monitored using sharp spectral features, e.g. specific on-board diffuser plates or by observing sharp atmospheric absorption or solar features. The spectral characterization must be done for each detection unit as it can differ across track.

3) Geometric calibration

When comparing different data sets, the data must be assigned to a geo-coordinate system. This assignment can be assessed by observing well-known and distinct geographic features like coast lines. The definition of the observation angles is also important because it characterizes the path of the light through the atmosphere. Depending on the path, the interaction of light with atmosphere and surface components differ and thus, the TOA signal is changed. Hence, the observation geometry must be characterized within the geometric calibration. Furthermore, the pixel size must be determined.

For the calibration activities, both an on-board calibration set-up is used and the calibration information from ground-based calibration are validated against other measurements. The prelaunch calibration coefficients of instruments that do not have an integrated calibration set-up can be monitored and corrected by comparing with measurements from other well characterized instruments. The TOA radiance measurements of two satellite sensors can be compared under certain conditions. Both sensors must observe the same geographic target under the same environmental conditions [Goldberg et al., 2011]. Optimal conditions for satellite-satellite comparison offer a tandem constellation like the one during the commissioning phase of S3B and like the one planned for the FLEX mission. A tandem constellation enables a continuous comparison. For such comparison, differences in spectral and spatial resolution as well as observation geometries must be considered. Instruments with differences in spatial resolution should observe homogeneous targets e.g. deep convective clouds, deserts or the moon. Differences in spectral resolution can be compensated by spectral convolution of the high resolution instrument (if available), by applying spectral band adjustment [Chander et al., 2013b] or a transfer function which is developed during this study and described in Chapter 3. Satellite measurements can also be compared to ground-based or airborne measurements. Again, the measurements must be conducted simultaneously to ensure same environmental conditions. However, a direct comparison of the TOA radiance is not possible. Thus, an atmospheric correction based on radiative transfer simulations is necessary. Additionally, spatial and spectral differences must be considered as mentioned above. The difference in radiance due to differences in spatial resolution can be large depending on the surface type and the considered spectral range. Usually, the spatial resolution of ground based instruments is less than a few meters whereas FLORIS's or OLCI's spatial resolution is 300x300 m^2. The effect of the difference in spatial resolution on the surface reflectance validation is studied in Chapter 4. The comparison with ground-based and airborne measurements is also limited to the number of overpasses under cloud-free conditions. The advantage of this method is that the ground-based instruments can be easily calibrated. Thus, they are very reliable.

If two satellites have no simultaneous overpasses of one area, ground-based instruments can be used to determine the relative bias between the two satellite instruments. Such cross-calibration was done e.g. for the Moderate Resolution Imaging Spectroradiometer (MODIS) on the spacecrafts Aqua and Terra using surface reflectance measurements from the Radiometric

Calibration Network (RadCalNet) [Angal et al., 2021]. The measured surface reflectance was used together with atmospheric measurements to predict the TOA reflectance which was set in relation with Aqua and Terra.

OLCI has an integrated on-board calibration set-up. A rotating platform contains two white diffuser for the radiometric calibration, an erbium doped 'pink' diffuser plate for spectral calibration, a dark shutter plate for the dark current detection and an open baffle for the operational mode [ESA, 2016]. The bidirectional reflectance distribution function (BRDF) of the diffuser and their orientation must be characterized before launch. However, the diffusers degrade due to the sun exposure. Thus, OLCI carries two redundant diffuser plates: one that is used regularly (every 2-4 weeks) and one which is only used every three months to monitor the changes of the first diffuser [Bourg, 2014]. OLCI performs dedicated spectral calibration campaigns every three months in which its micro bands are reprogramed to cover different spectral features of the solar Frauenhofer lines, the atmospheric absorption or the pink diffuser [Rebhan et al., 2014]. The results of the calibration and other analyses are monthly published in product data quality reports.

Besides the on-board calibration modes, there have been numerous calibration and validation activities for OLCI. To ensure the smooth continuity between OLCI-A and OLCI-B, the tandem phase was used to determine a harmonization of the two TOA radiance spectra [Lamquin et al., 2020]. Furthermore, vicarious calibration missions took place e.g. using the moon as target to verify the stray light correction and the radiometric performance [Neneman et al., 2020]. Spectral calibration and spectral analysis showed that the positions of the central wavelengths change over time [Lamquin et al., 2020, Preusker, 2021]. Preusker [2021] developed a temporal evolution model, which estimates the central wavelengths for each detector, band and orbit number.

FLEX will also have an on-board calibration set-up for FLORIS. To retrieve the small fluorescence signal, calibration and validation is crucial [Nuzzi et al., 2023]. The spectral calibration will be made on ground before launch and it will be checked while being in orbit using vicarious techniques measuring distinct absorption features of the atmosphere and the sun [Coppo et al., 2017]. One part of the prelaunch calibration is the quantification of the stray light. The stray light correction is based on the method of Spatial Point Source Transmittance (SPST) [Nuzzi et al., 2023]. Maps of areas which are affected by stray light of a point measurement at different wavelengths are created in the laboratory. Those wavelength dependent maps are combined to reconstruct the incoming light field. With this superposition, a stray light correction will be realised.

The on-board calibration set-up of FLORIS is a rotating plate with a diffuser, a dark reference plate and the opening baffle for the operational mode [Coppo et al., 2017]. The radiometric calibration with the diffuser will be performed 7-15 days and the dark current measurement every 2-3 orbits. In addition, the tandem constellation with S3 fulfils the requirements for continuous satellite-satellite comparison. The difference in spectral response must be considered e.g. by a convolution of the high resolution measurements of FLORIS with OLCI spectral response functions or using a transfer function (see Chapter 3).
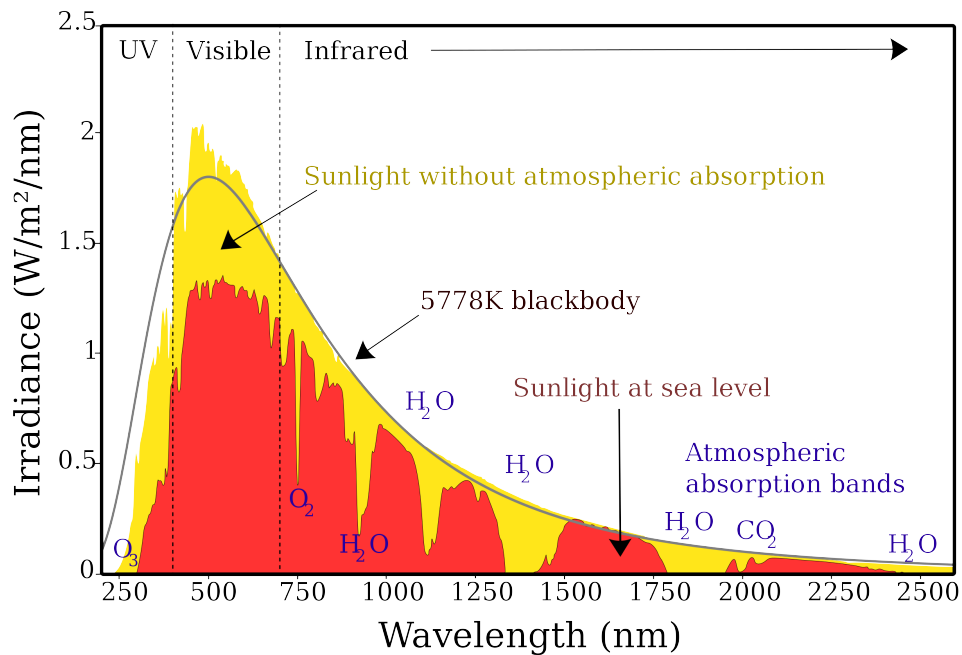
Figure 2.5   True solar spectrum at TOA irradiance in yellow and at bottom of atmosphere in red. Taken from Rohde [2013]

2.2 Radiative transfer in the earth system

To interpret radiation reflected from the earth and measured by satellite sensors, a deep understanding of the radiative transfer through the atmosphere and the interaction with the surface is necessary. The incoming solar spectrum can be approximated with Planck's law for black body radiation [Liou, 2002, p.11]

$$B_\lambda(T) = \frac{2hc^2}{\lambda^5(e^{hc/(k_B\lambda T)} - 1)}.$$ (2.1)

The black body radiation B scales with h Planck's constant, c speed of light, k_B Boltzmann constant and the body's temperature T. In case of the solar spectrum at TOA, a temperature of about 5800 K can be assumed. Planck's law for a body of this temperature approximates well the solar flux. However, it is not enough to describe the solar spectrum on a spectral scale. Both the solar spectrum described by Planck's law as well as the true solar spectrum as measured at TOA are shown in Figure 2.5. The true solar spectrum shows various absorption lines by atoms of the sun (e.g. hydrogen, magnesium or iron), called Frauenhofer lines [Liou, 2002, p. 54]. The maximum of the solar spectrum is between 380 and 700 nm which is our visible spectral range. The solar radiation interacts with constituents of the atmosphere and the surface. The light, which is backscattered to the satellite's instruments carries information about those components. This information can be extracted by describing and quantifying the light path.

2.2.1 Atmosphere

The interaction of light with particles and molecules in the atmosphere are scattering, emission and absorption. Those processes are characterized by the radiative transfer equation (RTE). It can be approximated for a plane-parallel atmosphere. The direction of propagation from zenith is $\mu = cos(\Theta)$ with Θ the propagation zenith angle and the vertical coordinate is the optical thickness τ. The optical thickness is determined by the volume extinction coefficient β_e and the thickness of the regarding layer. As vertical coordinate, it can be written depending on the height z [Petty, 2006, p.173]

$$\tau(z) = \int_z^\infty \beta_e(z')dz'. \tag{2.2}$$

The approximation of a plane-parallel atmosphere is valid for small propagation zenith angles because such light is not affected by earth curvature. The RTE describes the change of the incoming radiation $I(\mu, \phi)$ with zenith angle Θ and azimuth angle ϕ [Petty, 2006, p.325]:

$$\mu \frac{dI(\mu, \phi)}{d\tau} = I(\mu, \phi) - J(\mu, \phi) \tag{2.3}$$

The source function J summarizes the sources and sinks of radiation within the observed layer namely absorption, emission and scattering:

$$J(\mu, \phi) = (1 - \tilde{\omega})B - \frac{\tilde{\omega}}{4\pi} \int_0^{2\pi} \int_{-1}^1 p(\mu, \phi, \mu', \phi')I(\mu', \phi',)d\mu'd\phi' \tag{2.4}$$

B is the blackbody radiance characterized by Equation 2.1. The emission within the visible and near infrared (NIR) spectral range is negligible for typical temperatures of the atmosphere and the surface. The single scattering albedo $\tilde{\omega}$ is the ratio of volume extinction coefficient β_e and scattering coefficient β_s

$$\tilde{\omega} = \frac{\beta_s}{\beta_e}. \tag{2.5}$$

The scattering at molecules and particles is characterized by their particle specific phase function p which gives the probability of the light being scattered in a specific direction $(\mu'\phi')$. The scattering and absorption by gas molecules and aerosol particles are presented in the next sections.

The attenuation of the direct light beam within a layer between heights s_1 and s_2 depends on the optical thickness τ and it follows Beer's law

$$I_\lambda(s_2) = I_\lambda(s_1)e^{-\tau(s_1, s_2)}. \tag{2.6}$$

Gases

The constant constituents of the atmosphere are nitrogen (78%), oxygen (20%) and other gases (argon, carbon dioxide, methane,...) [Liou, 2002, p.67]. Additionally, the atmosphere contains varying amounts of water vapour and ozone depending on space and time [Liou, 2002, p.68]. All those gases absorb and scatter radiation.

Absorption by gas molecules within the considered spectral range is an energy transformation of the energy of the photons to transitions of the gas molecules in their electronic, vibrational or rotational state. All those energy levels are quantized and thus, the transition consumes energy at certain wavelengths. The result are distinct absorption lines. Between 400 and 800 nm, the most prominent absorption lines are caused by oxygen absorption at 680 and 760 nm, namely the oxygen B (O_2B) absorption band and the oxygen A (O_2A) absorption band. Further dominant absorption features are due to absorption by water vapour at 720 and around 800 nm. All absorption lines are not infinitesimal small but they have a certain width. The shape of the absorption lines is an effect of line broadening (natural, pressure and Doppler broadening). The natural line broadening due to the Heisenberg's uncertainty principle is negligible [Petty, 2006, p.260]. In the lower atmosphere, the pressure broadening has the strongest effect. Collisions with other molecules disturb the transitions which enables the absorption of photons with slightly smaller or larger wavelengths [Petty, 2006, p.260]. The Doppler broadening describes photon absorption allowing random translations of molecules in the stratosphere and the mesosphere.

Scattering of photons is not an energy conversion but a change in direction due to interaction with particles. Light, which is scattered in the direction of the observed light path, is added to the incident light beam. Within the visible spectrum, gas molecules are much smaller than the wavelengths of the photons. Thus, scattering at gas molecules can be approximated with Rayleigh scattering which is the dominant source within the visible spectrum under cloud-free conditions. The scattered radiance scales with the wavelength λ^{-4}

$$I(\lambda, \Theta) = \frac{I_0}{r^2} \alpha^2 \left(\frac{2\pi}{\lambda} \right)^4 \frac{1 + cos^2\Theta}{2} \tag{2.7}$$

Hence, blue light is scattered much stronger which is why the clear sky is blue. r is the radius of the particle, α determines the polarizability and I_0 is the intensity of the incoming light. Equation 2.7 describes scattering at a dipole. The incoming light is an electromagnetic field for the molecule in which it starts oscillating. The oscillating dipole emits a new electromagnetic wave with the same wavelength, the scattered light, which is linearly polarized. The Rayleigh phase function for incident unpolarized light, as it is true for sun light, can be calculated by normalizing Equation 2.7 [Petty, 2006, p.351]:

$$p(\Theta) = \frac{3}{4}(1 + cos^2\Theta). \tag{2.8}$$

The phase function shows that the light is scattered equally in the forwards and backwards whereas less light is scattered at 90 and 270 degrees (see Figure 2.6a) [Liou, 2002, p.90].
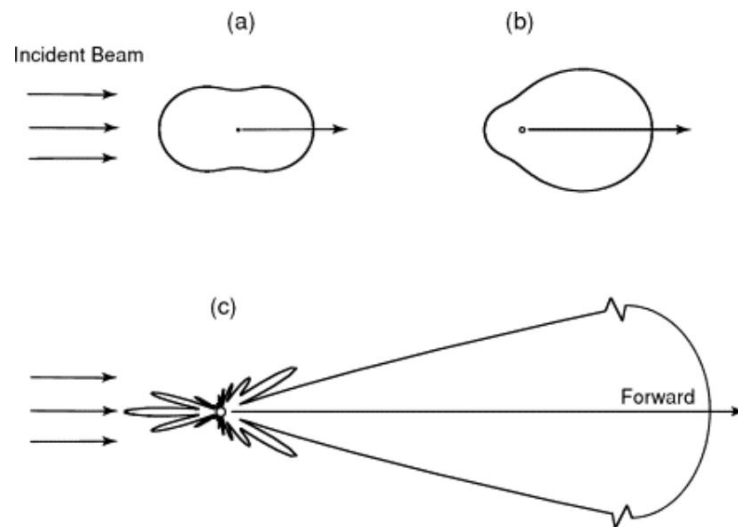
Figure 2.6   Scattering phase functions for scattering at spherical particles with different sizes: a) 10^{-4} μm, e.g. gas molecules following Rayleigh scattering, b) 0.1 μm and c) 1 μm following Mie scattering. Taken from Liou [2002]

Aerosol

Aerosol particles are particles originating usually from the earth's surface with diameters between few nanometers and tens of micrometers [Rees, 2012, p.98,100]. Dust, sea spray, and smoke can be uplifted under certain meteorological conditions or volcanic ash can be directly transported to the atmosphere. The particles have different optical properties, e.g. soot particle are strongly absorbing whereas dust particles are mainly scattering.

Due to their size in the order of the visible and NIR wavelength, interaction of aerosol particles with light is very complex. Scattering cannot be described with Rayleigh scattering. Instead, scattering and absorption at spherical particles can be approximated by Mie theory [Wiscombe, 1980]. Radiation that is scattered at particles larger than the wavelength has a large forward peak as shown in Figure 2.6. The amount of absorption depends on the imaginary part of the refractive index.

Mishchenko and Travis [1994] developed a spheroid model which accounts for scattering at particles with a complex shape like dust particles. The particles are randomly orientated which represents a dust particle distribution. Nevertheless, this model is an approximation as the true dust shape is more complex than a spheroid. Such approximation reduces computational time when modelling scattering with aerosol particles.
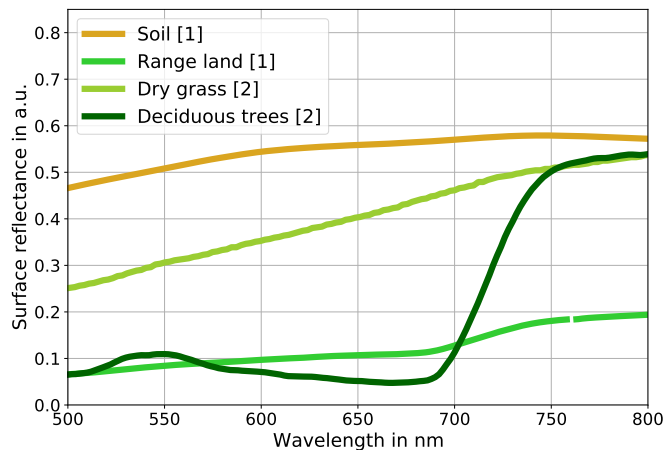
Figure 2.7   Surface reflectance between 500 and 800 nm of different surface types (soil, range land, dry grass and deciduous trees) based on data from [1] Clark et al. [2007] and [2] Baldridge et al. [2009].

2.2.2 Surface

The interaction of the earth's surface with radiation is reflection, absorption and emission depending on the wavelength.

Ocean surface

A smooth and homogeneous ocean surface would reflect light following the description of geometric optics by Fresnel [Petty, 2006, p.103]. However, wind increases the surface roughness and with this, the sharp reflection cone broadens. Cox and Munk [1954] studied this area of reflection called sun glint. They found a statistical description of the orientation of planes that are representative for the facets of waves. Once the orientation of each plane is known, geometric optics can be applied to each plane to describe the reflection at the ocean surface. The distribution of the planes depends on the wind speed. The rougher the surface, the stronger is the blurring and the larger is the sun glint area [Petty, 2006, p.103].

Land surface

The surface reflectance for vegetated surfaces depend on the angle of incident light and on the observation geometry. The angular distribution of the reflected light is described by bidirectional reflection functions (BRDF) [Petty, 2006, p.105]. An approximation of the land surface reflection can be Lambertian reflection distribution. Here, light is reflected in all directions equally. The spectral features of the surface reflectance depend on the surface type. Examples of surface reflectance spectra are shown in Figure 2.7. The most complex structure has the surface reflectance spectrum of vegetated surfaces with a strong increase of reflectivity between 680 and 740 nm, which is called red-edge.

2.3 Radiative transfer simulation with the matrix operator method

The path of radiation through the atmosphere can be simulated computationally using radiative transfer models. Within this thesis, the matrix operator model (MOMO) is used. MOMO was developed and advanced at the Freie Universität Berlin by Fischer and Grassl [1984], Fell and Fischer [2001], Hollstein and Fischer [2012], Doppler et al. [2014a]. It is a vector radiative transfer model which simulates polarized radiance in a spectral range between 200 nm and 100 μm for distinct viewing and sun geometries. The atmosphere is simplified to a plane-parallel atmosphere with homogeneous layers. Thus, the optical properties depend only on the vertical coordinate. The plane-parallel assumption neglects the earth curvature which is usually true for zenith angles smaller than 75 degrees [McCartney, 1976, p.105]. MOMO can be coupled with surface models including optical ocean models.

The matrix operator method was described in various publications (e.g. Redheffer [1962], Hulst [1963], Preisendorfer [1965], Twomey et al. [1966]). This description will follow the summary of Plass et al. [1973] and the description of Fell and Fischer [2001] and Hollstein and Fischer [2012] who describe its application within the MOMO code. MOMO is based on the RTE (Equation 2.3) and the interaction principle. For numerical treatment of the RTE, it is reshaped and discretized. A Fourier expansion is applied to the RTE to separate azimuth and zenith angle. The resulting Fourier terms are separated equations independent of the azimuth angle [Fell and Fischer, 2001]. Furthermore, the integrals of Equation 2.3 are transformed into sums at Gaussian quadrature points with Gauss Lobatto weights [Hollstein and Fischer, 2012]. Finally, the light field is split in upwelling and downwelling light and the RTE is expressed with matrices (see Hollstein and Fischer [2012]).

The interaction principle states that the light field at a border between two layers depends linearly on the transmitted and the reflected light. The transmission and reflection can expressed as operators. Hence, the downwelling (I_0^+) and upwelling (I_0^-) light fields at τ_0 are:

$$I_0^- = \mathbf{R_{01}}I_0^+ \mathbf{T_{10}}I_1^- + \mathbf{J_{10}} \tag{2.9}$$

$$I_0^+ = \mathbf{R_{10}}I_0^+ \mathbf{T_{01}}I_1^+ + \mathbf{J_{01}}. \tag{2.10}$$

I_1^+ is the upwelling light at τ_1. The reflection operator $\mathbf{R_{01}}$ quantifies the amount of radiance that is reflected upwards between the layer boundaries τ_0 (upper) and τ_1 (lower) and $\mathbf{R_{10}}$ vice versa. $\mathbf{T_{01}}$ and $\mathbf{T_{10}}$ are the transmission operators for downward and upward transmission, respectively. $\mathbf{J_{01}}$ and $\mathbf{J_{10}}$ describe the sources within the layer emitting light downward and upward. Those equations can be written in a matrix form similar to the RTE. Using a coefficient comparison, the transmission, reflection and source operators can be expressed by the phase matrix, source terms, Gaussian weights and quadrature points that describe the RTE.

The interaction principle is applied to the different layers. Additionally, the layers are split in sublayers with equal and very thin optical thicknesses. With such thin optical thickness, multiple

scattering can be neglected and only single scattering must be considered. The application of the interaction principle on adjacent layers is called doubling in case of the same optical properties (sublayers) and adding for layers with different optical properties. With the doubling method, the upwelling and downwelling light for the complete layer can be estimated and multiple scattering is considered. The adding method finally combines the different layers and provides the upwelling light at TOA.

The input for the RTE is the single scattering albedo and the phase function of the absorbing and scattering particles in each layer, namely aerosol, cloud particle and gases. For aerosol, a pre-calculated phase function, e.g. the spheroid model from Dubovik et al. [2006] can be used. MOMO also includes a module that calculates phase functions for spherical particles based on Mie scattering using particle mixtures with given size distribution, refractive indices, extinction coefficient and single scattering albedo. As shown in Section 2.2.1, scattering at aerosol creates a strong forward peak. The description of this peak in the Fourier space would require many Fourier terms. To reduce this number and increase the computational speed, a phase function truncation is applied. The forward peak is treated as unscattered light and thus, its radiance is added to the direct light beam.

The gas absorption and scattering depends on the vertical profile of the atmosphere. Temperature, pressure and humidity profiles must be given. Such profiles can be either directly measured by e.g. radiosondes, or meteorological model outputs or standard profiles are used. According to those profiles, the gas concentration is defined which scales the absorption. The module "Coefficients of Gas Absorption" (CGASA) [Doppler et al., 2014a] simulates gas absorption spectra based on a common data base. In this study, the HITRAN data base was used [Gordon et al., 2017]. Within the visible spectral range, the absorption lines are simulated by a line-by-line model using a Voigt profile for the central line and a Lorentz profile for the wings of the absorption line [Doppler et al., 2014a].

MOMO calculates the radiances monochromatically. The simulation of a high resolution spectrum output of CGASA would require thousands of model runs. Thus, the k-binning method is applied to reduce the number of simulations [Doppler et al., 2014b]. Many wavelength sampling points have approximately the same absorption coefficient. Those absorption coefficients are binned in k bins. Each k-bin has an according weight so that the weighted coefficients add up to the total absorption within in the considered spectral range. This spectral range is predefined either as rectangular response function or as the instrument response function. In this thesis, MOMO simulations were performed to estimate OLCI's TOA radiance. Due to OLCI's large number of spectral response functions, rectangular response functions were chosen with a width that includes all spectral responses of the according band. The resulting radiance for a single response function could be calculated by adding weighted radiances for each k-bin with modified weights according to the considered response function.

2.4 Optimal estimation

Information about earth's atmosphere and surface from TOA radiances can be gained by comparing measurements with radiative transfer simulations. The radiative transfer model calculates the light path for given atmospheric and environmental parameters. When simulation and measurement agree, a set of parameters is found that describes the atmospheric and surface state during the measurement. As all satellite sensors have only limited amounts of bands and limited accuracy, their information content is also limited. Hence, it is not possible to determine all parameters. Furthermore, the radiance can have no sensitivity to some atmospheric parameters. In other words, there is not only one set of parameters that lead to the same result than the measurement but many. Consequently, some parameters must be known as fixed input for the simulations.

The best set of parameters can be found by simulating TOA radiances in an iterative way changing the input parameter for each step. The disadvantage is that many simulations must be performed multiple times which increases the computational time. Instead, the best set of parameters can also be found by interpolating in a large set of precalculated simulations so called look-up tables (LUTs). Those LUTs contain a wide range of possible combinations of state parameters at defined sample points. The choice of combinations depends on the study case and scene.

The interpolation within the LUTs replaces forward modelling using a radiative transfer model. A fast way of generating the best matching TOA simulation is the *one dimensional variational approach* (1Dvar) or *optimal estimation* as described by Rodgers [2000]. This approach starts with a set of fixed parameters and a priori parameters. A cost function is calculated which considers the measurement and a priori uncertainty. The state update during the optimization is selected following the steepest gradient of the cost function. The iteration stops when the change of parameters from one step to the other is significantly smaller than their anticipated uncertainty or a defined maximum number of iterations is reached. The underlying equations are presented in Section 3.3.7 and 5.3.5.

The measurement and a priori uncertainties are expressed as error co-variance matrices with diagonal elements being the squares of the uncertainties and the off-diagonal elements express correlations among the uncertainties. Those uncertainties are part of the retrieval error covariance matrix. Furthermore, uncertainties of the fixed parameters should be considered in the retrieval uncertainty. Such fixed parameters can be observation and sun angles, environmental parameters or instrumental parameters like the central wavelength. The uncertainty of the observation and sun geometry is determined in the geometric calibration. The environmental parameters, like the surface pressure or the wind speed, can originate e.g. from forecasts of the European Centre for Medium-Range Weather Forecasts (ECMWF). All uncertainties must be translated in the same measurement space and can be then added up as retrieval uncertainty [Rodgers, 2000]. The transfer from parameter to measurement space is realized by multiplying the parameter error covariance matrix with the corresponding Jacobian matrices consisting of partial derivatives with respect to the parameters. The partial derivatives of the radiance I with

respect to the parameter x are approximated numerically with

$$\frac{\delta I}{\delta x} = \frac{I(x + \Delta x) - I(x)}{\Delta x} \tag{2.11}$$

under the assumption of a small Δx. The LUTs are also used for sensitivity studies. The effect of changes in the parameter on the TOA radiance can be quantified by determining the Jacobians.

3

Estimation of systematic differences between OLCI-A and OLCI-FLEX

Authors Lena Katharina Jänicke[1], Rene Preusker[1], Marco Celesti[2], Marin Tudoroiu[3], Jürgen Fischer[1], Dirk Schüttemeyer[2], and Matthias Drusch[2]

---

[1]Institute of Meteorology, Freie Universität Berlin (FUB), Carl-Heinrich-Becker-Weg 6-10, 12165 Berlin, Germany
[2]HE Space for ESA - European Space Agency, ESTEC, PO Box 299, NL-2200 AG Noordwijk, The Netherlands
[3]ESA-ESRIN, Largo Galileo Galilei 1, 00044 Frascati (Rome), Italy

3.1 Abstract

During the tandem phase of Sentinel-3A and -3B in summer 2018 the Ocean and Land Color Imager (OLCI) mounted on Sentinel-3B satellite was reprogrammed to mimic ESA's 8th Earth explorer the Fluorescence explorer (FLEX). OLCI in FLEX configuration (OLCI-FLEX) had 45 spectral bands between 500 nm and 792 nm. The new data set with high spectral resolution measurements (band width: 1.7-3.7 nm) serves as preparation of the FLEX mission. Spatially co-registered measurements of both instruments will be used for the atmospheric correction and the retrieval of surface parameters e.g. the fluorescence or the leaf area index. For such combined products, it is essential that both instruments are radiometrically consistent. We developed a transfer function to compare radiance measurements from different optical sensors and to monitor their consistency.

In the presented study, the transfer function shifts information gained from high-resolution "FLEX-mode" settings to information convolved with spectral response of the normal (lower) spectral resolution of the OLCI sensor. The resulting reconstructed low resolution radiance is representative for the high resolution data (OLCI-FLEX) and it can be compared with the measured low resolution radiance (OLCI-A measurements). This difference is used to quantify systematic differences between the instruments. Applying the transfer function, we could show that OLCI-A is about 2 % brighter than OLCI-FLEX for most bands of the OLCI-FLEX spectral domain. At the longer wavelengths (>770 nm) OLCI-A is about 5 % darker. Sensitivity studies showed that the parameters affecting the quality of the comparison of OLCI-A and OLCI-FLEX with the transfer function are mainly the surface reflectance and secondarily the aerosol composition. However, the aerosol composition can be simplified as long it is treated consistently in all steps in the transfer function.

Generally, the transfer function enables direct comparison of instruments with different spectral responses even with different observation geometries or different levels of observation. The method is sensitive to measurement biases and errors resulting from the processing. One application could be the quality control of the FLEX mission, presently it is also useful for the quality control of the OLCI-FLEX data.

3.2 Introduction

Sentinel-3 is part of the European Copernicus program which provides Earth observation data for scientists and policy makers [Jutz and Milagro-Pérez, 2020]. The program is designed amongst others to deliver long-term climate records. Sentinel-3 carries the Ocean and Land Color Imager (OLCI), a push-broom spectral imager with 21 bands between 400 and 1020 nm [Donlon et al., 2012]. Currently, two twin Sentinel-3 satellites with a similar design but different manufacturing dates and instrumental characterization are in orbit, namely Sentinel-3A (since 2016) and Sentinel-3B (since 2018).

During the commissioning phase of Sentinel-3B in 2018, a smooth continuity was guaranteed by a tandem phase of Sentinel-3A and -3B [Clerc et al., 2020]. Both satellites flew in the same

orbit observing the same geographic target within 30 s. The measurements were taken with the same geometrical and environmental conditions. Thus, a comparison of the radiance data was possible [Lamquin et al., 2020].

Contributing to a deeper insight into plants activity and their response to environmental changes, ESA's eighth Earth Explorer Fluorescence Explorer (FLEX) will be launched in 2025 [Van Wittenberghe et al., 2021]. It will carry a high resolution Fluorescence Imaging Spectrometer FLORIS which measures the radiance between 500 and 780 nm [Drusch et al., 2017, Coppo et al., 2017]. Its band characterization is summarized in Table 3.1. FLEX will fly in tandem formation with Sentinel-3 and the OLCI sensor (onboard of Sentinel-3) will deliver the necessary information for performing the atmospheric correction of FLORIS [Drusch et al., 2017, Coppo et al., 2017].

This tandem constellation was mimicked during the tandem phase of Sentinel-3A and -3B for 24 acquisition scenes (5 minutes each). OLCI-B was reprogrammed to measure in 45 bands between 500 and 792 nm. An overview of the spectral resolution of the different data sets is shown in Table 3.1. For a meaningful usage of the OLCI-B data in FLEX configuration (OLCI-FLEX), the quality of the data must be estimated. A comparison with OLCI-A is most promising as the tandem constellation allowed measurements under the same conditions. However, OLCI-FLEX has a different spectral response which does neither allow a direct comparison nor a convolution with the spectral response of OLCI-A. To overcome this limitation, we developed a transfer function which enables the comparison of OLCI-A and OLCI-FLEX radiance measurements. It is applied for vegetated cloud free land pixels, as the main objective of FLEX mission is to retrieve fluorescence emitted by plants. The spectral signature of vegetated surfaces is very complex and thus, a method to compensate the differences in spectral response among OLCI-A and OLCI-FLEX is particularly important for those targets.

Lamquin et al. [2020] showed a systematic bias between OLCI-A and OLCI-B in the tandem constellation data, with slight discrepancies depending on the nature of the targets. The bias of OLCI-FLEX with respect to OLCI-A will be estimated by using our transfer function on vegetated pixels. The bias should be consistent with the findings of Lamquin et al. [2020]. Furthermore, this comparison is a test of the calibration of FLORIS. Its calibration will partly rely on inter-calibration with OLCI. Niro et al. [2021] stated that Level 1 data consistency throughout the complete ESA fleet is of "utmost importance for the interoperability" of different mission products. For FLEX, an inter-operational product is planned and thus, a consistency with its tandem partner is necessary. This consistency is checked for OLCI-A and OLCI-FLEX using the transfer function.

An example for inter-calibration is the validation of Moderate Resolution Imaging Spectroradiometer (MODIS) Terra and Aqua shown by Angal et al. [2021]. Radiative transfer simulations were used to simulate TOA reflectance based on ground-based measurements. However, for this comparison well defined surface and atmosphere descriptions are necessary. The difference in spatial resolution between ground-based and satellite-based instruments results in differences in surface description and inserts uncertainties.

The direct inter-comparison of TOA radiances is possible under the condition of simultaneous

overpasses, similar spatial resolution and observation geometry. Under those conditions, only the spectral resolution differences must be considered. A spectral adjustment was introduced by Chander et al. [2013b] who used a third high-resolution instrument to calculate a spectral band adjustment factor. However, the third instrument introduces also uncertainty, that must be determined. Furthermore, the number of samples meeting all requirements is very limited. In contrast, a comparison of instruments flying in tandem with similar spatial resolution is possible for a large number of targets allowing a robust quality control.

Our transfer function allows such comparison for instruments with the same spatial resolution but different spectral response. The application of the method on the OLCI-A/OLCI-FLEX data set enabled us to quantify a systematic bias between OLCI-A and OLCI-FLEX. The method and its application is presented in this paper. In Section 3.3 the method is presented including the description of the input data (3.3.2), the radiative transfer simulations (3.3.4) and the 1D-variational approach (3.3.7). In Section 3.4, the results are shown. We present the sources of uncertainty in Section 3.5. In Section 3.6, we discuss the results and draw the conclusion in Section 3.7.

3.3 Methods

3.3.1 Description of the transfer function

To compare the top-of-atmosphere (TOA) radiance of OLCI-A and OLCI-FLEX, we developed a transfer function allowing the comparison of their level 1B (L1B) data on a common spectral setting. A schematic overview of the transfer function is given in Figure 3.1. The transfer function is based on two sets of consistent radiative transfer simulations: one set simulating OLCI-FLEX and the other one OLCI-A measurements. Information about atmosphere and surface is retrieved from the higher resolution OLCI-FLEX data with an 1D variational approach (1Dvar). The information is shifted to the band characteristics of OLCI-A (light green arrows) and a forward model simulates the corresponding TOA-radiance that is based on information gained from OLCI-FLEX. The reconstructed radiance, based on the information of OLCI-FLEX but with same spectral response as OLCI-A, can be compared with measured OLCI-A. The method is applied pixelwise. The reconstructed spectrum will be referred to as OLCI-B-to-A-reconstructed (OLCI-B2AR) from now on. To summarize the method, we shift the OLCI-FLEX radiance (measured by OLCI-B) to the band characteristics of OLCI-A using radiative transfer simulations and the OLCI-A spectral response functions.

The used data are level 1B (L1B) data from OLCI-FLEX and OLCI-A. The L1 data include radiances, observation geometry, band characterization, inband solar irradiance, water vapour content, ozone concentration and information about the surface (sea surface pressure, altitude, temperature). In addition to the satellite data, AERONET data are used to characterize the aerosol (see 3.3.2) [Giles et al., 2019]. The input parameter for the transfer function are aerosol information, the measurement geometry and the OLCI-FLEX radiances which are corrected for water vapor and ozone as part of the preprocessing (3.3.3). The core of the transfer function
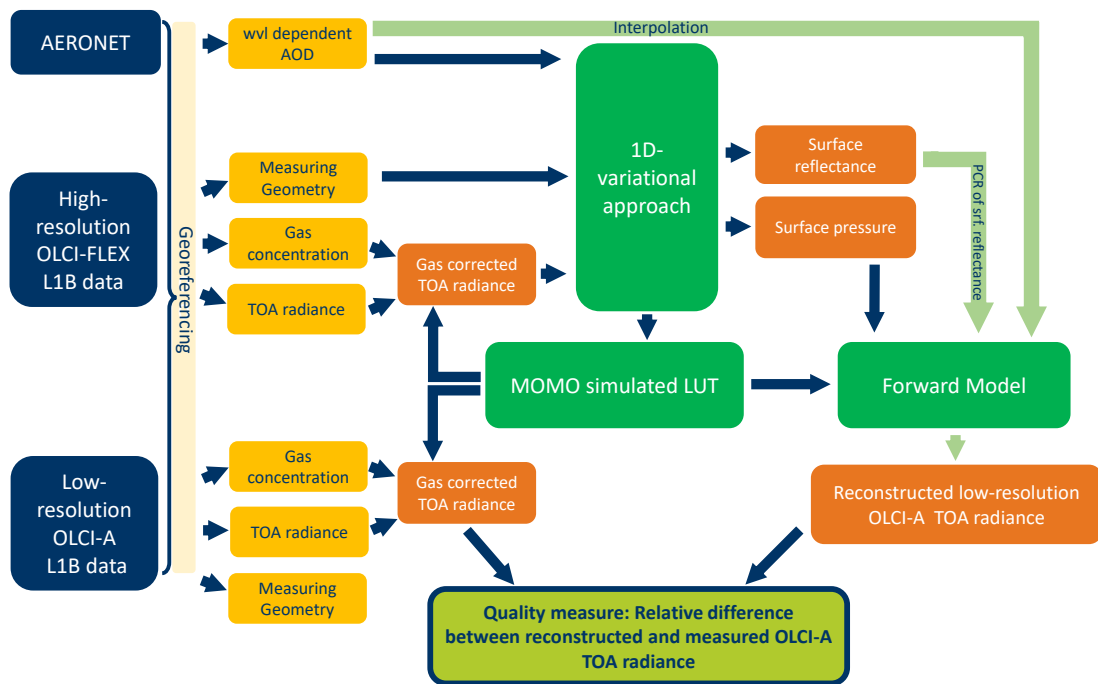
Figure 3.1 Schematic overview of transfer function for OLCI-FLEX and OLCI-A. In blue boxes: data sources, in yellow: measured input data characterizing the environment, in orange: processed data, in green processors. The light green box with blue frame is the result of the process. The dark blue arrows point in the direction of the data and the light green arrows symbolize the spectral interpolation from OLCI-FLEX bands to OLCI-A bands.

is the 1Dvar and the forward model which are based on look-up tables (LUTs). The output of the 1Dvar is the surface reflectance and the surface pressure. The aim of the transfer function is not to find a physically perfect state of the atmosphere and the surface but to find a state that explains as best as possible each pixel-wise measurement of OLCI-FLEX. This requirement allows to reduce the degrees of freedom of the transfer function. The detailed description of the radiative transfer model and its input is given in Sections 3.3.4 and 3.3.5.

A principle component regression (PCR) is used to shift the surface reflectance to band characteristics of OLCI-A, as described in Section 3.3.8. The aerosol information from AERONET is shifted using linear interpolation. Together with the measurement geometry of OLCI-A, its band characteristics and the optimized surface pressure, the shifted surface and aerosol information serve as input for the forward model. The resulting OLCI-B2AR radiance is representative for the OLCI-FLEX measurement. The difference between the reconstructed and measured OLCI-A radiance quantifies the bias between the two data sets. As OLCI-FLEX is just a different setting of OLCI-B, the found bias quantifies the bias between OLCI-A and OLCI-B. Thus, the results can be compared with the comparison of the two instruments by Lamquin et al. [2020].
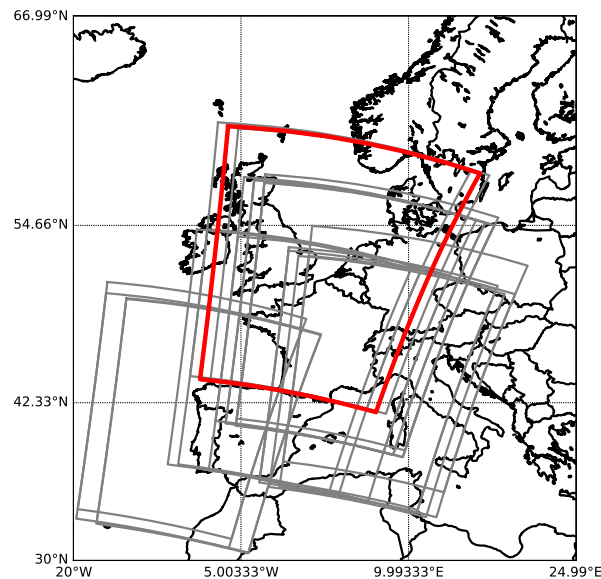
Figure 3.2   Map of Europe with frames of 22 OLCI-FLEX acquisition scenes in grey. In red, the frame of OLCI-FLEX scene on 2nd July 2018.

3.3.2 Data

Besides the L1b radiance of OLCI-A and OLCI-FLEX, additional parameters are needed as input for the transfer function. Most information is taken directly from the OLCI L1 data sets or related data like the spectral response functions for the 24 acquisition scenes. We focus on the 22 scenes over central Europe as shown in Figure 3.2. In addition, two scenes were located over North America.

OLCI's spatial coverage of 1270 km is realised by 5 cameras with charged coupled devices (CCD) with 740 x 520 detectors each [ESA, 2016]. 740 rows are aligned across track resulting in a pixel size with a width of about 300 m and 520 detector rows are aligned along track to measure all 21 spectral bands simultaneously. Each of the 740 detector rows has their own spectral response function per band. The detector and camera information are necessary to identify the according spectral response function. The spectral responses of OLCI-FLEX and OLCI-A will be quantified by central wavelength and full width at half maximum (FWHM). The response functions of OLCI-A are taken from ESA [2016]. The ones for OLCI-FLEX were generated assuming Gaussian response of a single detector. The FWHMs of the detectors are taken from pre-launch characterization. The central wavelengths are taken from the temporal evolution model of the wavelength characterization (see Section 3.3.3).

Pixel selection

The transfer function is applied for land pixels, because the mission is primarily designed for land applications. They are classified based on the quality flag set of OLCI-A L1-b data. Furthermore, the quality flags marking bright, invalid and saturated pixels are used from that data set. If one band is saturated in a pixel, this pixel is not used for the transfer function. Cloudy

pixels are also filtered out by applying the flag bright pixel as first estimate. For a further classification of clouds, the IDEPIX routine is used. It is implemented in Sentinel Application Platform SNAP [Wevers et al., 2022]. Here, the flag "Cloud buffer" is applied for a more conservative treatment of clouds. Within the processing, other quality criteria are implemented e.g. for cases of failures in the 1Dvar or the PCR.

Band characterization OLCI-FLEX

The 45 FLEX like bands are distributed in the visible spectral range between 500 and 792 nm. The oxygen absorption bands have a high coverage with bands every 1.25 nm. The bandwidths are limited by the elementary spectral band of OLCI which is nominally 1.7 nm wide. The other bands are distributed over the spectral range with widths up to 3.7 nm by combining elementary bands. The nominal central wavelengths and bandwidths of OLCI-FLEX bands are listed in Table 3.1.

The L0-to-L1b-processing of the 45 OLCI-FLEX bands is based on the regular OLCI OL1 processor, which expects 21 input bands. Thus, the 45 bands were split in three subsets with 21 bands each (called FX1, FX2, FX3)[ESA, 2021b, ACRI-ST, 2019]. Each subset covers the visible wavelength range between 500 and 792 nm with equally distributed sample points to achieve a best possible stray light correction during L1b processing.

For the transfer functions, the 21 bands of the set FX1 are the basis of the used data set. Bands which are not part of FX1 data sets are used from the data sets FX2 and FX3. The radiances of duplicated bands are very similar. Thus, the transfer function is only applied to one selection of bands.

Band characterization OLCI-A

For the comparison with OLCI-FLEX, 12 OLCI-A bands in the same spectral range have been selected namely Oa05-Oa16. Their nominal band widths vary between 2.5 and 15 nm. Their nominal central wavelengths and band widths are given in Table 3.1.

Table 3.1 Overview of band distribution, nominal central wavelength and bandwidth of FLORIS, OLCI-FLEX and OLCI-A.

	FLORIS		OLCI-FLEX		OLCI-A	
Band	FWHM	Spectr. sampl.	Central wvl	FWHM	Central wvl	FWHM
500-600	3	2	500.625, 531.875, 535.625	3.7	510	10
			538.125	1.7		
			540.625	3.7		
			543.125	1.7		
			545.625, 550.625, 570.625, 585.625	3.7	560	10
600-677	3	2	600.625, 615.625, 620.625	3.7	620	10
					665	10
					673.75	7.5
677-686	0.6	0.5	681.87, 683.125, 684.375, 685.625	1.7	681.25	7.5
686-697	0.3	0.1	686.875, 688.125, 689.375	1.7		
			696.875	1.9		
697-740	2	0.65	706.875, 710.625, 721.875, 734.375	1.7	708.75	10
740-759	0.7	0.5	746.875, 755.625, 756.875, 758.125	1.7	753.75	7.5
759-769	0.3	0.1	759.375, 760.625, 761.875, 763.125, 764.375	1.7	761.25	2.5
			765.625	2.0	764.375	3.75
			766.875, 768.125	1.7	767.5	2.5
769-780	0.7	0.5	769.375, 770.62, 771.875,	1.7	778.75	15
			773.125, 774.375, 775.625, 776.875	1.7		
			791.875	3.7		

Table 3.2   Classification of surface based on NDVI and randomly chosen surface spectra.

NDVI	Surface Type	Source
<0	Flagged out	-
0-0.1	Soil (Halloysite)	USGS speclib06a
0.1-0.2	Dry grass	ASTER
0.2-0.3	Range land	USGS speclib06a
>0.3	Deciduous Forest	ASTER

Aerosol information

The AOD is taken from the closest AERONET station to each pixel. For each scene, all stations with valid measurements are selected and the distance to each pixel is calculated with the great circle distance measure. The mean over one day of the measured AOD from the closest station is used as fixed aerosol prior knowledge. The spectral resolution of the AERONET measurements is low. Usually there are only three sample points in the visible range with measurements at 500, 675 and 870 nm. We assume that the AOD varies with λ^{-1}. To calculate the AOD at the central wavelength of OLCI-FLEX pixel,the AOD is fitted with a λ^{-1}-function. With this method, the measured spectral extinction of the present aerosol is considered in the transfer function. Other aerosol parameters like the single scattering albedo (SSA) and the phase function are not adapted in the transfer function. Instead, a fixed aerosol model is used in the radiative transfer function (see Section 3.3.5). The precise knowledge about those aerosol properties is not necessary. The effect of this simplification is discussed in Section 3.5.1.

Surface information

Information about surface pressure and surface type is needed for the simulation of TOA radiances. The sea level pressure and the altitude are given in the Sentinel-3 data sets. Using the barometric height formula, the surface pressure is approximated. For a linear temperature gradient of 0.65 K temperature decrease per 100 m, the surface pressure p is

$$p = p_0 \cdot \left(1 - \frac{0.0065 \cdot h}{T} \right)^{5.2555}, \tag{3.1}$$

with p_0 sea level pressure in hPa, T temperature at surface in Kelvin and h altitude in meter. The first guess of the surface reflection for the 1Dvar is selected based on the normalized difference vegetation index (NDVI). The NDVI is calculated using L1B TOA radiances with

$$NDVI = \frac{I_{791} - I_{681}}{I_{791} + I_{681}}. \tag{3.2}$$

Based on the NDVI, the surface is classified in surface types as shown in Table 3.2. For each surface type, a surface reflectance spectrum is chosen randomly from the data bases measured

by Advanced Spaceborne Thermal Emission Reflection Radiometer ASTER [Baldridge et al., 2009] or United States Geological Survey USGS [Clark et al., 2007].

3.3.3 Preprocessing

The preprocessing includes the georeferencing to find matching pixels, the gas correction of the TOA radiance, the normalization of the radiance using the inband solar irradiance and the application of the temporal evolution model of the central wavelength developed by Preusker [2021].

Georeferencing

For the georeferencing, we used the same method that was suggested by Lamquin et al. [2020]. They showed that the reprojection of both OLCI-A and OLCI-B on the same regular grid results in a valid georeferencing of OLCI-A and B for the tandem phase data. We reprojected OLCI-A and OLCI-FLEX data on the same regular grid with a resolution of $0.01°$ on the basis of their high-resolution longitude and latitude position taken from the *geo_coordinates.nc* files.

Gas correction

The gas concentrations of water vapour and ozone are provided in the OLCI L1b data set. The data originate from forecasts of the European Centre for Medium-Range Weather Forecasts (ECMWF). The gas corrected TOA radiance $I_{gas_{corr}}$ can be calculated by scaling the measured TOA radiance I_{meas} with the gas transmission:

$$I_{gas_{corr}} = \frac{I_{meas}}{exp(-c \cdot \tau(cwvl, fwhm) \cdot amf)}.$$

(3.3)

The gas optical thickness τ is calculated in the k-binning model. The spectral high resolution output of the k-binning model is convolved with the spectral response functions of OLCI-FLEX and OLCI-A, which results in a central wavelength (cwvl) and FWHM dependence of τ. The scaling factor c is the ratio of the provided gas concentration and the gas concentration used for the k-binning model. The path length of the light is approximated by the air mass factor amf. It is calculated using the sun zenith angle (SZA), viewing zenith angle (VZA):

$$amf = \frac{1}{cos(SZA)} + \frac{1}{cos(VZA)}.$$

(3.4)

The gas correction in this simplified way is possible since the interaction of absorption and scattering is weak.

Time-evolution of band characteristics

OLCI's spectral characteristics are regularly monitored in-flight using spectral campaigns. The procedures use the programming capability of OLCI to define 45 bands around stable spectral features, to characterize the spectral dispersion of each camera system with respect to the spectral and the spatial (across track) dimension. Simulations of OLCI measurements in the 45 bands are optimized for best agreement with the spectral features, as a function of assumed bandwidth and band centre wavelength of an individual CCD element. Depending on the used spectral feature the achieved accuracy for the central wavelength is in the order of 0.1-0.2 nm, the precision (repeatability) is better than 0.05 nm. The regularity of the spectral campaigns allows a precise quantification of the temporal evolution of the spectral response for each individual CCD-element on each camera CCD, at least for the investigated spectral features. It emerges that all cameras show a tiny but distinct evolution. Both, the single CCD-row bandwidth and the across track variability ('smile') of the central wavelength remain almost constant for all cameras of OLCI-A and -B, but the central wavelengths of all pixels move almost homogeneously with a decreasing rate. Since launch, four of the five cameras of OLCI-A and -B respectively, have drifted up to 0.3 nm towards longer wavelengths. One camera (camera 5 for OLCI-A and camera 3 for OLCI-B) has drifted by 0.3 nm to shorter wavelengths. The dependency of the central wavelength on the orbit can be described with the following model [Preusker, 2021]:

$$cwl = a + b * ln(orbit) + c * ln(orbit)^2. \tag{3.5}$$

The coefficients a, b and c are published for OLCI-A and OLCI-B band sets for any band, pixel and orbit in `https://sentinel.esa.int/documents/247904/2700436/LUT.zip`. With those coefficients, the central wavelength can be calculated for an arbitrary orbit of OLCI-A or -B.

The temporal evolution of the OLCI-FLEX spectral characterization is based on the spectral shift of the OLCI-B band Oa12 at 753.75 nm (nominal). Its temporal shift is applied for all OLCI-FLEX bands within the O_2A absorption band. This approach is valid because of the homogeneous behaviour of the temporal evolution across the spectrum.

The central wavelengths of OLCI-A are also shifted using the described model and the corresponding LUTs.

3.3.4 Radiative transfer simulations

The radiative transfer simulations used to build LUTs for the transfer function were computed using the radiative transfer model "Matrix Operator Model" (MOMO) developed at Freie Universität Berlin [Hollstein and Fischer, 2012, Fell and Fischer, 2001]. It is a doubling and adding model based on a layered description of a plane-parallel atmosphere which can be coupled with an ocean-optical model or any surface bidirectional reflectance function. It solves the matrix form of the radiative transfer equation after discretizing it. Scattering functions of aerosol particles are calculated with the Mie algorithm [Wiscombe, 1980]. Gas absorption is implemented

using a k-binning description of line-by-line models [Doppler et al., 2014b].

3.3.5 Radiative transfer input

Atmospheric profile

The simulated atmosphere is divided in plane-parallel layers. Molecules and particles are distributed homogeneously within each layer. The vertical distribution of the atmospheric gases is based on a standard vertical temperature, pressure and humidity profile defined by AFGL Atmospheric Constituent Profiles [Anderson et al., 1986].

For the simulation of the OLCI-FLEX and OLCI-A measurements, the *mid-latitude summer* profile was used as all acquisition sites are in Europe and the campaign took place from 14th June till 14th August 2018. The standard profile is interpolated to build a model of the atmosphere that contains up to 23 layers with level borders every 50 hPa. The surface pressure is either 700, 800, 900, 1013 and 1050 hPa. Lower surface pressures reduce the number of levels.

Gas absorption

For the description of the wavelength dependent gas absorption processes, we use the HITRAN16 database [Gordon et al., 2017]. For the oxygen (O_2) absorption, we use the cross sections of Drouin et al. [2017]. All relevant atmospheric gases except of ozone and water vapour are considered in the simulations. Due to the weak interaction of absorption and scattering in the considered bands, the effect of those gases on the TOA radiance can be corrected by a simple transmission correction (see 3.3.3). The interaction between absorption of O_2 and scattering is strong in the oxygen absorption bands. Thus, TOA radiances must be calculated for different O_2 amounts. O_2 is a well mixed gas in the atmosphere and it scales with the surface pressure. The MOMO simulations are done for atmospheric profiles with different surface pressures to consider the effect of the O_2 interactions.

Aerosol model

A continental aerosol model from the OPAC database [Hess et al., 1998] is used for the simulations. The aerosol particles contain insoluble particle, water soluble particles and soot. The

Table 3.3 Information about aerosol components, refractive indices is given at 550 nm.

	Insoluble	Water soluble	Soot
Size Distribution Coeff. a	0.471	0.306	0.0118
Size Distribution Coeff. b	2.51	2.24	2.00
Refractive index (real)	1.53	1.399	1.75
Refractive index (imag.)	-0.8E-02	-0.199E-02	-0.44
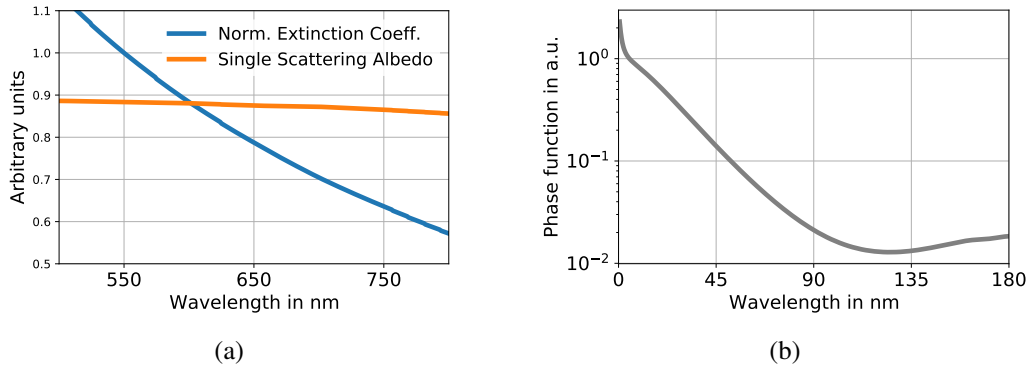
Figure 3.3   (a) Wavelength dependence of normalized extinction coefficient (blue) and SSA (orange) for the defined continental aerosol for reference wavelength 550 nm. (b) Angle dependent phase function at 550 nm for same continental aerosol.

refractive index and size distribution are given for a relative humidity of 80 %. The size distribution of each component is a log-normal distribution. Its coefficients and their refractive indices are given in Table 3.3. From those parameters the extinction coefficient and SSA are calculated. The wavelength dependence of the extinction coefficient is typical for a continental aerosol (Figure 3.3a). Using Mie-scattering theory, the phase function is developed for 171 different scattering angles between 0 and 180° (Figure 3.3b). The spectral dependence of the phase function $p(cos\Theta)$ can be described with the asymmetry parameter g:

$$g(\lambda) = \frac{1}{2} \int_{-1}^{1} p(cos\Theta) dcos\Theta \tag{3.6}$$

For the radiative transfer simulations, the aerosol particles are placed homogeneously distributed in the layer closest to the surface. All simulations are done with a reference AOD at 550 nm ranging from 0.05 to 0.8.

Using one aerosol model is possible as our method does not require a perfect description about the atmosphere. The effect of this simplification is discussed in Section 3.5.1.

Surface reflectance

The spatial resolution of OLCI is about 300 x 300 m^2 at nadir. The covered surface is most likely a mixture of different surface types in our study areas in Europe. It is simplified as isotropic reflector with surface reflectances between 0.01 and 0.81. An isotropic reflector reflects the light in all directions with the same probability. In reality, most surfaces have a distinct angular dependent probability function for the reflection of light.

3.3.6 Radiative transfer output

The output of MOMO is the diffuse up- and downwelling radiance at each layer for the simulated atmosphere and each representing rectangular band. The radiances are sun and viewing

angle dependent. For each k-term, the radiance and a weight is calculated. The radiances have the unit sr^{-1} for an associated solar constant of one.

The simulated upwelling radiances are convolved with the spectral response functions of OLCI-A [ESA, 2016] and of OLCI-FLEX. The spectral response functions of OLCI-FLEX are approximated with Gaussian functions. This approximation does not hold for OLCI-A spectral response functions. Thus, the actual response function shapes are used to convolve the simulations for the OLCI-A LUTs.

3.3.7 1D-variational approach

The information needed to describe the atmospheric state is determined by an 1D-variational approach (1Dvar). It finds the most probable state that describes the radiance measurement starting from *apriori* knowledge. The approach is implemented following Rodgers [2000].

The 1Dvar is an iterative process comparing a forward simulated radiance $F(X)$ with the measured radiance Y (with capital letter referring to vector and matrices):

$$G(X_i) = F(X_i) - Y \tag{3.7}$$

The state vector X_i is adjusted in each step i using the Gauss-Newton method:

$$\begin{aligned} X_{i+1} = X_i - (\mathbf{S_a}^{-1} + \mathbf{K_i}^T \mathbf{S_e}^{-1} \mathbf{K_i})^{-1} (\mathbf{K_i}^T \mathbf{S_e}^{-1} \cdot G(X_i) \\ - \mathbf{S_a}^{-1} \cdot (X_a - X_i)) \end{aligned} \tag{3.8}$$

The difference between forward model and measurement is weighted with the measurement error co-variance matrix $\mathbf{S_e}$ and the Jacobian $\mathbf{K_i}$. Furthermore, the difference between parameter state vector and *apriori* knowledge X_a is taken into account evaluating also the *apriori* error co-variance matrix $\mathbf{S_a}$. Using the Jacobians, the next step is selected in the direction of the largest gradient. The iteration stops when either the maximum number of iteration (10) is reached or the increment weighted by retrieval error co-variance matrix $\hat{\mathbf{S}}$ is small (Equation 3.10). The retrieval error co-variance matrix is given by

$$\hat{\mathbf{S}} = (\mathbf{S_a}^{-1} + \mathbf{K_i}^T \mathbf{S_e}^{-1} \mathbf{K_i})^{-1}. \tag{3.9}$$

It is weighted with the step width between two following states, giving the stop criterion:

$$(X_i - X_{i+1})^T \cdot \hat{\mathbf{S}}_{\mathbf{i}}^{-1} \cdot (X_i - X_{i+1}) > n \cdot \varepsilon \tag{3.10}$$

$\varepsilon = 0.01$ and n is the number of parameter state dimensions. This method can be applied under the assumption of Gaussian probability density functions of uncertainty and bias-free measurements, priors and models.

Table 3.4   Dimensions of LUTs.

	Surface refl.	**Surface pr.**	**AOD$_{550}$**	**Central wvl**	**FWHM**
Minimum	0.01	700 hPa	0.055	Band$-$0.5 nm	Min FWHM
Maximum	0.81	1050 hPa	0.94	Band$+$0.5 nm	Max FWHM
	SZA	**VZA**	**ADA**		
Minimum	0.0^o	0.0^o	0.0^o		
Maximum	88.49^o	88.49^o	180.0^o		

Look-up tables and interpolation

The parameters used in the 1Dvar and the forward model are the surface reflectance, surface pressure, the AOD, central wavelength, FWHM, SZA, VZA and azimuth difference angle (ADA). Simulations with variations of those parameters are stored in LUTs. Their dimensions are summarized in Table 3.4. The parameter dimensions of the LUTs are regularly spaced, allowing a fast indexing and interpolation for the forward operator. The step widths are given in Table 3.4. The N-dimensional interpolation of X^* in a regular parameter space $[p_1, p_2, ..., p_n]$ is divided into the following two steps:

1. Normalization of the input variables:

$$p_i^* = \frac{p_i - p_i^l}{p_i^u - p_i^l} \tag{3.11}$$

   where p_i^u and p_i^l is the nearest lower and the nearest upper parameter entry in the LUT.

2. Interpolation by a weighted sum of the 2^N enveloping neighbours in the LUT:

$$\begin{aligned} X^*(p_1, ..., p_n) = {} & (1 - p_1^*)(1 - p_2^*)...(1 - p_n^*)X^{l,l,...,l} \\ & + (0 - p_1^*)(1 - p_2^*)...(1 - p_n^*)X^{u,l,...,l} \\ & + ... \\ & + (0 - p_1^*)(0 - p_2^*)...(0 - p_n^*)X^{u,u,...,u} \end{aligned} \tag{3.12}$$

Optimization of OLCI-FLEX radiances

The 1Dvar is applied to the gas corrected OLCI-FLEX radiance measurement to find best possible characterization of the atmosphere and the surface. The atmosphere is parameterized with the surface pressure from the L1b data of OLCI-A and the standard vertical profile used in the radiative transfer simulations (see Section 3.3.5). The surface reflectance is optimized pixelwise and bandwise using the 1Dvar approach. A randomly selected surface reflectance spectrum according to the classified surface is used as *apriori* knowledge. This approximation is very rough and therefore, it is handled with a large *apriori* error of 1. All other state parameters,

namely band characterization (central wavelength and FWHM), wavelength dependent AOD, surface pressure, and measurement geometry (SZA,VZA, ADA), are kept constant and are taken from the sources described in Section 3.3.2. The measurement error co-variance contains the signal-to-noise ratio of OLCI which is approximately 1:200. The retrieved spectral dependent surface reflectance is used in the next step of the transfer function as input of the PCR, which is described in the next section.

3.3.8 Spectral interpolation of surface reflectance

OLCI-FLEX bands do not cover all spectral features of the surface reflectance needed to reconstruct the surface reflectance at the lower resolution OLCI-A. An interpolation of the surface reflectance at nominal OLCI-A bands at 510, 560, 665, 673.75 and 681.25 nm is not possible due to the gaps in the OLCI-FLEX spectrum (see Table 3.1). We decided to use a principal component regression (PCR) to fill the missing gaps. A set of high resolution surface reflectance spectra from the spectral libraries USGS [Clark et al., 2007] and ASTER [Baldridge et al., 2009] are decomposed into eigenvectors. Depending on the NDVI of each pixel the data base for the PCR is chosen. For a low NDVI (<0.2), all spectra in the USGS soil data base are used The range land spectra from USGS vegetation data base are used for pixels with NDVI between 0.2 and 0.3 and all vegetation spectra except of the range land spectra from USGS plus the grass and forest spectra from the ASTER data base are used for pixels with high NDVIs (>0.3). The found eigenvectors are called principal components since a linear combination of those can reconstruct an arbitrary surface reflectance spectrum. The decomposition into eigenvectors and the linear regression to find the linear coefficients are made using the Python library scikit-learn [Pedregosa et al., 2011]. For each pixel, a set of 4 and a set of 6 principal components are found. The set with the minimum mean squared error between reconstructed and input surface reflectance is chosen. If no valid reconstruction can be found, the pixel is flagged. Similarly, Vidot and Borbas [2014] found that six principal components is the optimal input to reconstruct hyperspectral surface reflectance spectra from seven MODIS bands.
The PCR is used to transfer the surface reflectance retrieved at OLCI-FLEX bands to OLCI-A bands Oa05 (510 nm), Oa06 (560 nm), Oa08 (665 nm), Oa09 (673.75 nm) and Oa10 (681.25 nm). The other OLCI-A bands are transferred by a linear interpolation of the OLCI-FLEX bands.

3.3.9 Forward simulation

The found information of the surface and the atmosphere serve as input for the forward model that reconstructs OLCI-A TOA radiance measurements. All wavelength dependant information is shifted from the OLCI-FLEX bands to the OLCI-A bands. A combination of PCR and linear interpolation shifts the surface reflectance to the OLCI-A bands. The AOD originating from AERONET is also interpolated. The mean surface pressure from the 1Dvar, band characteristics
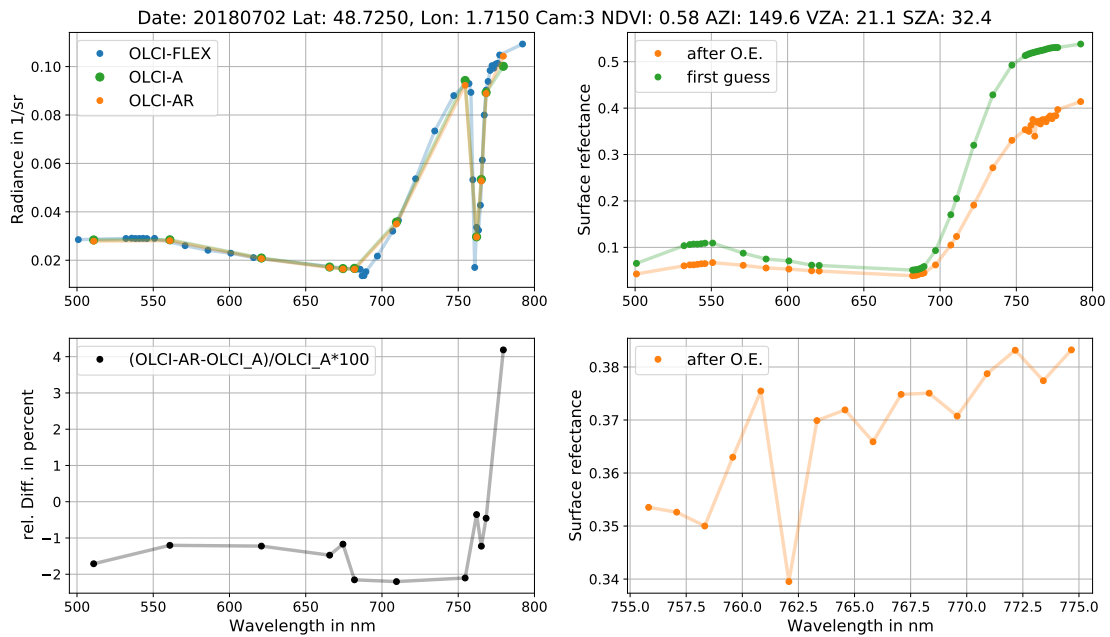
Figure 3.4   Results of transfer function for one reprojected pixel on the 2nd July 2018. Upper left: gas corrected measurements and OLCI-B2AR; upper right: first guess of the surface reflectance and the one from the 1Dvar approach (after optimal estimation OE); lower left: relative difference between reconstructed and measured OLCI-A radiance, lower right: optimized surface reflectance in O_2A absorption band.

of OLCI-A (central wavelength, FWHM) and measuring geometry serve as input for the forward model without further transformation. The output of the forward model is a TOA radiance at the OLCI-A bands that is based on information gained from OLCI-FLEX and thus, which is representative for the OLCI-FLEX measurement. The forward model is applied band and pixelwise.

3.4 Results

3.4.1 Transfer function applied on single pixel

We applied the transfer function pixelwise. The results for an example pixel west of Paris from the 2nd July 2018 is shown in Figure 3.4. We chose the pixel due to the good agreement of the measured radiances at the first glance and the small spatial distance of 140.5 m between the pixel centres of OLCI-FLEX and OLCI-A. The good agreement indicates that the measurements are not affected by an heterogeneous surface or atmosphere. In the upper left plot, the gas-corrected TOA radiances are given. The spectral distribution of the bands shows the discussed gaps of OLCI-FLEX bands between 500 and 520 and between 650 and 680 nm. The OLCI-B2AR radiances, created by applying the transfer function on OLCI-FLEX, differ slightly from the measured radiance OLCI-A. Only in the last band, OLCI-A and OLCI-B2AR and OLCI-FLEX radiances deviate more. We use the relative difference between OLCI-A and the OLCI-B2AR

to quantify the agreement between the two data sets.

$$\Delta I = \frac{I_{OLCI-B2AR} - I_{OLCI-A}}{I_{OLCI-A}} * 100. \tag{3.13}$$

The difference is shown in the lower left subplot of Figure 3.4. The negative difference between the OLCI-B2AR and OLCI-A data indicates that the radiance measured by OLCI-A is brighter than the one measured by OLCI-FLEX. Only at longer wavelength (780 nm), OLCI-FLEX is brighter. The relative difference between 550 and 680 nm is approximately one percent. Between 681.25 and 753.75 nm, we can observe a decrease of the relative difference to two percent and a strong gradient for the bands within and behind the O_2 absorption band.

The information about the surface that describes the state observed by OLCI-FLEX is given in the right subplots of Figure 3.4. The surface reflectance has a strong red-edge and a smooth spectrum as typical for vegetated surfaces. Only in the oxygen band, the surface reflectance shows small oscillations (see lower right plot in Figure 3.4). Reasons for oscillations in O_2 band can be errors in spectral characterization of OLCI-FLEX and OLCI-A, in the surface pressure and the instrument measurement uncertainty. Most probably it is a combination of all three reasons, which are not entangled in the scope of this paper.

3.4.2 Statistical evaluation of relative difference between satellites

A large range of relative differences between OLCI-B2AR and OLCI-A radiances can be observed when studying different pixels. It depends on the validity of the geo-referencing and the quality of the PCR. To reduce the effects of these uncertainties, a statistical evaluation of many pixels is necessary. The median value of the relative difference is calculated for different parameters for land pixels of the OLCI-FLEX scene on the 2nd July 2018. The median is chosen because it is less sensitive to outliers. The area covered in this scene is shown with the red frame in Figure 3.2.

Median by camera

The first statistical evaluation is done by taking the median of all pixels for each camera in our study scene. Each camera data set contains more than 200 000 measurements. Figure 3.5 shows the median relative difference for each camera for all valid land pixels measured by OLCI-FLEX and OLCI-A. The median is negative with values of about 2 %. Only camera 5 shows a smaller relative difference of about 1 %. These results confirm that overall OLCI-FLEX measures darker radiances than OLCI-A. Only at the 780 nm, the difference reaches positive values of more than 4 %.

To quantify the representativity of the median we use a bootstrap method: 1 000 random subsets of about 20 000 pixels were selected to calculate the median. The minimum and the maximum median value serve as lower and upper error bound in the plot. The resulting error bars at 680 nm
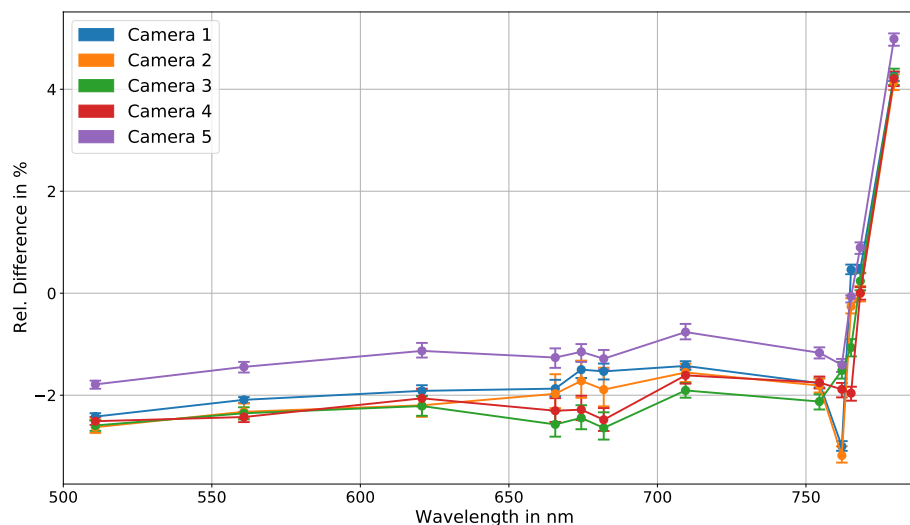
Figure 3.5   Median relative difference between OLCI-B2AR and OLCI-A radiance for each camera. All valid pixel of 2nd July 2018 were used, which gives about 200 000 pixels per camera.

are slightly larger which is due to the lack of knowledge about the surface reflectance at those bands. This gap is filled with the PCR which introduces an uncertainty.

The medians for the cameras allow a visualisation of the wavelength dependent difference. We can observe a slight increase with the wavelength between 500 and 750 nm. Small features within the oxygen band at 760 nm (O_2A band) indicate errors in the description of the band characterization or the atmospheric parameters. The strong gradient in the relative difference behind the O_2A band is not expected.

In Figure 3.5, we observe that camera 3 and camera 5 show almost no absorption feature of the O_2A band. Whereas camera 1 and 2 have the strongest absorption features. This observation is even more striking in Figure 3.7. From that observation, we conclude that the assumed spectral response functions are very accurate for camera 3 and 5. Reasons for the absorption features in camera 1,2 and 4 are either the spectral characterization or the occurrence of aerosol types which are not represented by the simulated aerosol model. The effect of a wrong aerosol model is discussed in Section 3.5.1.

Median by detector index

The camera effects are studied in more detail with the median of the relative difference for each detector which is presented in Figure 3.6. Every 10 detectors are binned together. The median is only taken for bins with more than 1000 entries. The representativity is shown in the shaded areas. It is estimated with the bootstrap method described before. In 100 iterations, the median was calculated for subsets of one tenth of data points. The minimum and maximum median are the borders of the shaded area.
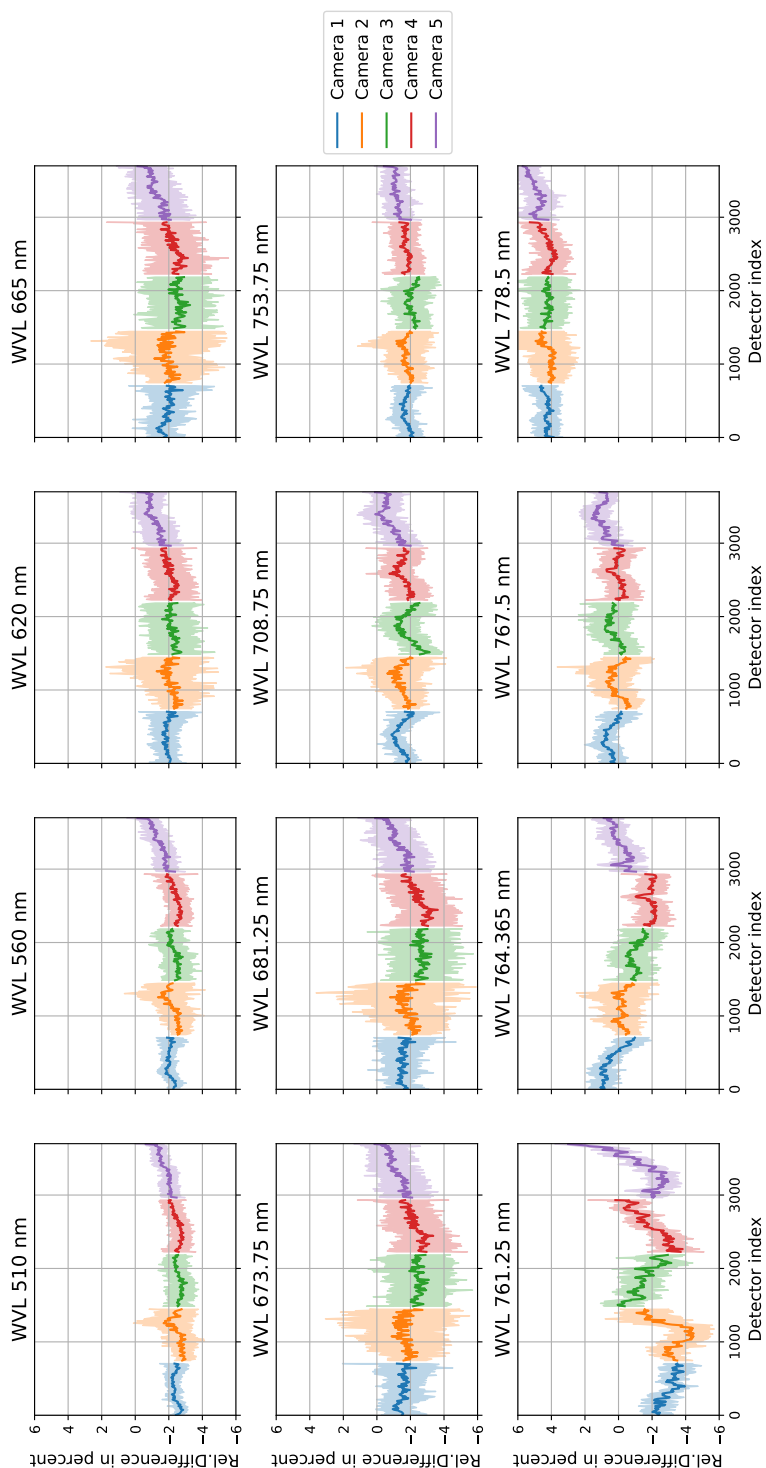
Figure 3.6   Median over detectors of relative difference between OLCI-AR and OLCI-A radiance. Every 10 detector indices were binned together, each bin has at least 500 entries. Each subplot gives one OLCI-A channel. The 740 detectors of each camera are serially numbered from west to east: detector indices 0 till 740 belong to camera 1, 741 till 1480 to camera 2,... The different cameras are colour coded. Shaded area shows representativity.

The variation in the relative difference across the field of view is strongest for camera 5. The drift of relative difference in camera 5 explains the difference of the median over the camera compared to the other cameras seen in Figure 3.5. However, across the cameras we observe a good continuity with only small discrepancies between the cameras.

Further camera effects can be observed for all cameras at 708.75 nm. This band is influenced by water vapour absorption. The relative difference between OLCI-B2AR and OLCI-A radiances are larger at the camera edges. The same effect can be observed at 767.5 nm which lies within the weaker part of the oxygen absorption band. The bands at 761.25 and 764.375 nm are in the spectral area with sharp oxygen absorption lines. Here, the largest variations in the median can be observed.

The largest uncertainty shows camera 2 especially in the nominal bands 665, 673.75 and 681.25 nm, which confirms the observations in Figure 3.5.

Overall, the relative difference is about 2 % over most detectors and wavelengths. Only at the end of the studied spectrum, the relative difference becomes positive with values of up to 5 %. The results of the median for the individual detectors agree with camera median.

Transfer function applied on time series

The tandem phase of OLCI-FLEX and OLCI-A lasted three months from May 2018 till August 2018. All scenes were recorded over a similar part of Europe (see Figure 3.2). Nevertheless, the underlying surface changed over time as the tandem phase was during the crop harvesting season. Additionally, observations of OLCI-A showed that the instrument is ageing most strongly during the first months after launch. The tandem phase of OLCI-FLEX and OLCI-A was during the commissioning phase of OLCI-B just after its launch. Hence, a time-dependent study of the difference between OLCI-FLEX and OLCI-A is necessary. The transfer function was applied on scenes at the beginning, in the middle and the end of the mission and for scenes with a small cloud coverage.

Figure 3.7 shows the comparison of the median relative differences over camera for four selected days. For all four days, the spectral shape of the relative difference is similar for all cameras. The largest deviations among the different days are between 660 and 680 nm. As discussed before, it is the spectral region in which the method shows its largest uncertainty due to the lack of bands in the OLCI-FLEX setting. Within the spectral region, the validity of the transfer function depends on the quality of the PCR which differs from pixel to pixel. This feature is most prominent on the 24th of June especially in camera 4. However, we cannot observe a systematic time dependence of the relative difference. Hence, the effect is due to coincidence of other differences among the scenes, e.g. covered area or cloud coverage. A small difference between all days and the 2nd of August can be observed in camera 1. However, the time step to the next study scene is only three days. Within such short period, we do not expect such a change in the camera characterization.

Overall, the deviation in relative difference shows no systematic features in the different cameras over time. Hence, the difference between OLCI-FLEX and OLCI-A has no significant time
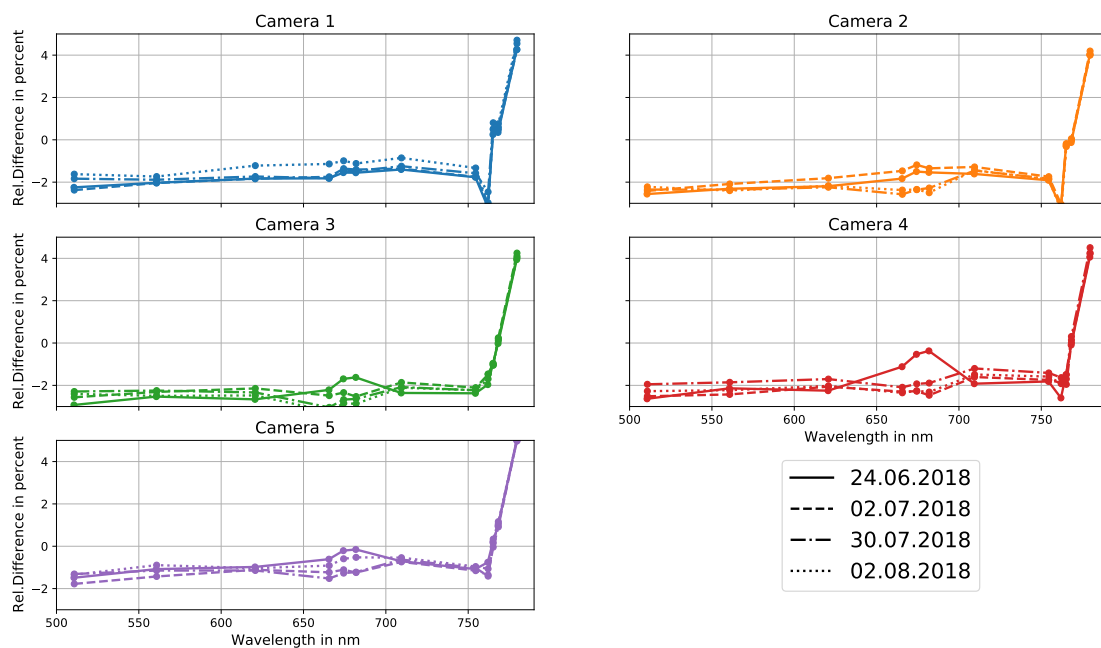
Figure 3.7   Median of rel. Difference between OLCI-B2AR and OLCI-A radiances over all valid of scenes at selected days of the campaign.

dependency within the studied time period. This result shows the quality of used time-evolution model of the band characterization. The wavelength does change over time by maximum 0.1 nm, if this change was not considered, we would have seen a time dependence in the relative difference.

3.5 Sources of uncertainty

The sources of uncertainty affecting the method of the transfer function are discussed qualitatively in the following section. Besides the uncertainty introduced by simplifications and assumptions of the radiative transfer model, uncertainty is primarily introduced by the uncertainty of the input data for the inversion and the forward model, namely the radiance, surface pressure, measurement geometry, spectral response, the total column water vapour, ozone concentration, co-registration, and aerosol parameters. Most data are used from the level 1 files of OLCI-A (Section 3.3.2).

The uncertainty of radiance is estimated with a signal to noise ratio of 200 and it is considered in the diagonal elements of the measurement co-variance matrix. We assume no co-variances. The uncertainty of measurement geometry, the band characterization, water vapour and ozone content are not propagated within the transfer function. Nevertheless, the effect of band characterization is qualitatively discussed in Section 3.5.3.

The systematic uncertainty introduced by errors in the misalignment are already discussed in Section 3.4.2. By taking the median over a large data set, the uncertainty due to misalignment is minimized. The good representativity of the median is shown by the small error bars gained
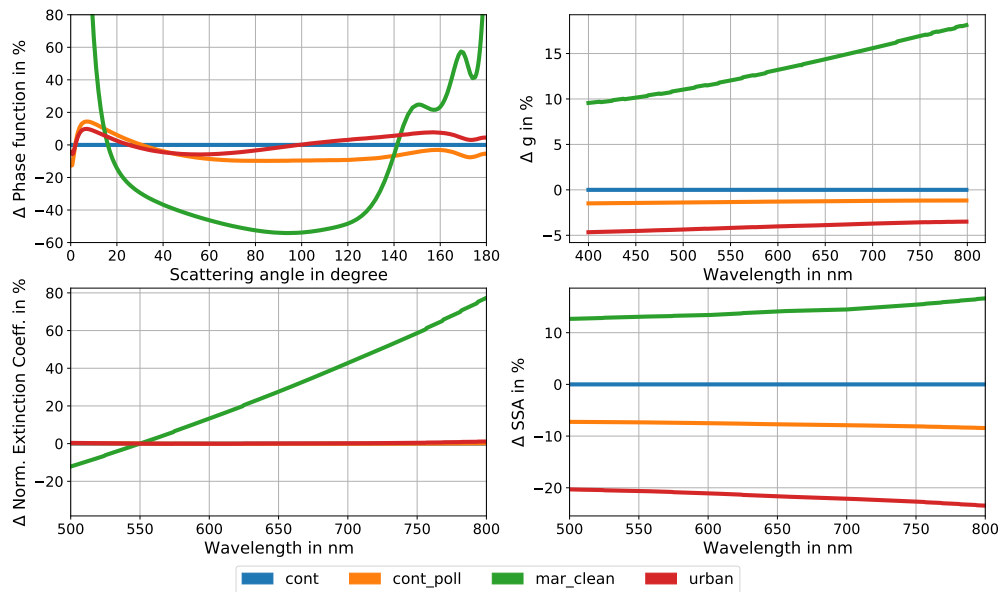
Figure 3.8   Aerosol properties of input aerosol types for sensitivity study. Properties are relative to properties of continental aerosol (see Figure 3.3). The different types are continental, continental polluted, maritime clean and urban aerosol as defined in OPAC data bank.

in the bootstrap method. It implies an accurate determination of the bias between OLCI-A and OLCI-FLEX.

The effect of the fixed aerosol model and the rough assignment of AERONET data to the pixels and the coupled errors in AOD are discussed in the next section. We also show their impact on the quality of the surface reflectance in Section 3.5.2. Additionally, the effect of the PCR is discussed briefly.

3.5.1 Aerosol-model sensitivity

Two simplifications in the description of the aerosol can induce uncertainties. Firstly, we fix the phase function and the SSA according to a single aerosol model. Secondly, the AOD and the spectral extinction of the aerosol is approximated with data from the closest AERONET station. The following sensitivity study shows the effect of the fixed aerosol phase function and SSA and a wrong spectral AOD on the transfer function and on the reconstructed spectra. Simulated high-resolution spectra with different aerosol models serve as input of the transfer function which is based on fixed aerosol model. The output of the transfer function, the reconstructed spectrum, is compared to the matching simulated low-resolution spectrum. From the comparison, we can estimate the error induced by the simplification of using a fixed aerosol type. The fixed aerosol model is a continental aerosol as shown and described in Section 3.3.2.
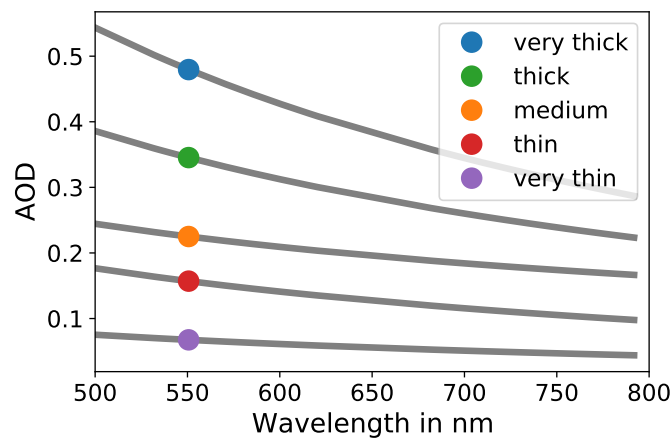
Figure 3.9   The spectral aerosol extinction taken from different AERONET stations. The reference AOD at 550 nm is marked with a coloured circle. Each spectrum will be referred to as optical very thick ($AOD_{550} = 0.48$), thick ($AOD_{550} = 0.35$), medium ($AOD_{550} = 0.23$), thin ($AOD_{550} = 0.16$) and very thin ($AOD_{550} = 0.07$).

Experimental set-up

We created two scenarios showing the effect of

1) wrong phase functions and SSA but correct spectral extinction of the aerosol.

2) wrong phase functions and SSA and wrong spectral extinction of the aerosol.

Both scenarios are based on the same set of simulated radiances.

As scatterer, we chose four different predefined aerosol models of the OPAC data source [Hess et al., 1998] namely *continental*, *continental polluted*, *urban* and *maritime clean* aerosol. Those models cover the variety of strong and less absorbing aerosols with different phase functions which we would expect in summer over Europe. We assume a vegetated surface and a surface pressure of 1013 hPA.

In Figure 3.8, the aerosol properties of the chosen aerosol models are shown relative to the continental aerosol. The maritime clean aerosol differs most strongly from the continental aerosol in three parameters, phase function, asymmetry parameter, and the normalized spectral extinction coefficient. The urban aerosol is strongly absorbing, which can be seen in the relative difference of SSA.

Both scenarios are set up for different optical thicknesses of the aerosol. Five different AOD spectra retrieved at different AERONET stations within Europe on the 2nd of July 2018 were chosen. The spectra are shown in Figure 3.9. We forced the chosen aerosol models to follow the measured spectral extinction shown in Figure 3.9. As a result, we got 20 aerosol extinction spectra which serve as input for the simulations. For each spectrum, we simulated an OLCI-FLEX and OLCI-A radiance spectrum.

We applied the transfer function on the 20 simulated OLCI-FLEX spectra. The LUTs are the same as described in Sections 3.3.5 and 3.3.7 with the continental aerosol model used. The two scenarios differ in the aerosol input parameters for the inversion of OLCI-FLEX spectra and the
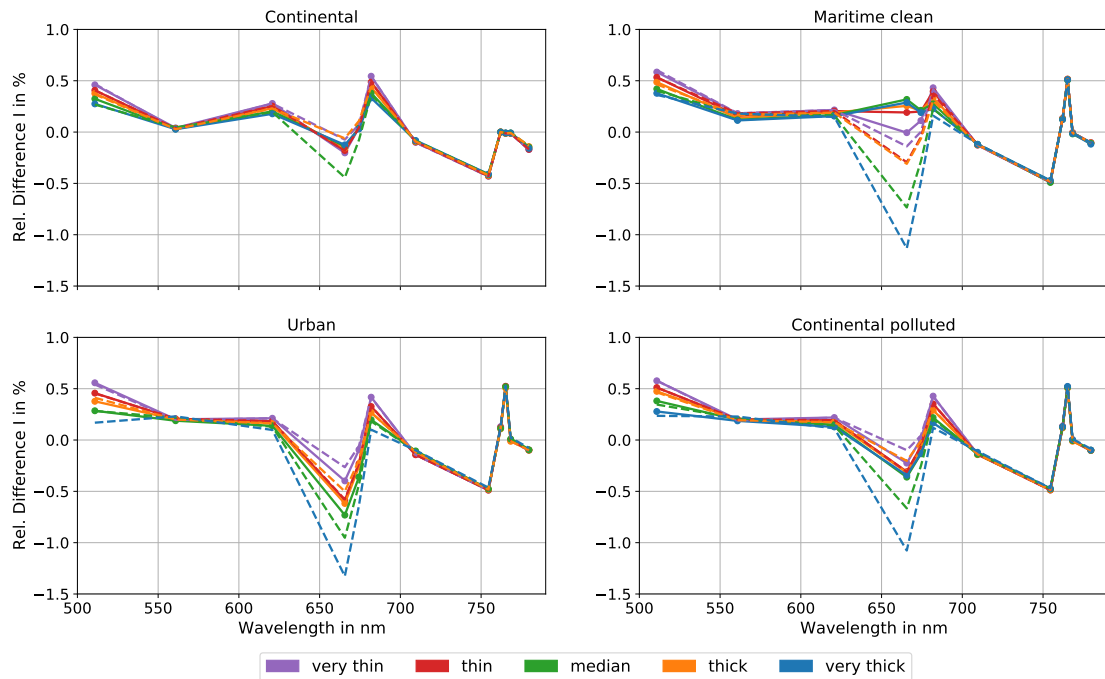
Figure 3.10   Relative difference of radiance after transfer function applied to simulations with different aerosol types. The transfer function was applied using different input parameter. Solid lines: scenario 1, dashed lines: scenario 2. The reference AOD is given in Figure 3.8.

forward model. In both scenarios, the *apriori* knowledge about the surface was a surface reflectance spectrum of vegetated land with a slight different spectral shape compared to the truth. The difference between the scenarios is the choice of the aerosol input. In scenario 1, the correct spectral extinction of the aerosol serves as input for the inversion and the forward model. In reality that means, that the measured spectral AOD from the AERONET station represents the present aerosol but the usage of the continental aerosol model in the LUT induce errors due to its phase function and SSA. The input for scenario 2 is the spectral extinction of the "thin" aerosol with a reference AOD at 550 nm of 0.16. In 16 cases, this aerosol description does not represent the actual spectral extinction of the aerosol.

Results

The difference between simulated OLCI-A spectra and reconstructed OLCI-A spectra which are based on simulated OLCI-FLEX spectra are shown in Figure 3.10 for both scenarios. It is calculated using Equation 3.13. Scenario 1 is plotted in solid lines and scenario 2 in dashed lines. The relative difference between the output of the transfer function and the simulated OLCI-A radiance has the same order of magnitude for all cases.

The cases with the continental aerosol in scenario 1 serve as control case. They are shown in the upper left plot. In those cases, we do not insert any errors in the description of the continental aerosol neither in the AOD nor the phase function or the SSA. Nevertheless, the relative differ-

ence is not as expected zero for all bands. The deviation of the relative difference in the intensity shows the residual error made within the transfer function. It originates from the interpolation of the surface reflectance from OLCI-FLEX bands to OLCI-A bands as shown in Figure 3.11 and discussed in the next section 3.5.2.

From the other cases of scenario 1, we can estimate the effect of the difference in the phase function and the SSA (see upper right and lower subplots in Figure 3.10). The three cases are based on a different aerosol model but the correct spectral extinction. The major difference to the control case with the continental aerosol model is within the oxygen absorption band. The results of the three cases with wrong aerosol model show the same deviations in relative difference from zero where the control case shows a relative difference of zero. This deviation shows that the oxygen absorption band is sensitive to the aerosol model, but the choice of aerosol model is not important. The choice of aerosol model affects the bands between 665 and 681.25 nm. Here, the gaps in the band distribution of OLCI-FLEX are filled with additional knowledge from the PCR (see Section 3.5.2). The largest absolute relative difference in intensity are shown by the results with the urban aerosol model. This aerosol model is most absorbing and thus, its effect on the TOA radiance is strongest. This effect is only visible between 665 and 681.25 nm. For all cases, the relative difference is increased slightly with the AOD for the 665 nm band. The other bands show rather a decrease with the AOD. With an increasing AOD, the TOA radiance is less sensitive to the underlying surface. Thus, the errors in the interpolation affecting the signal less and the relative difference decreases with the AOD. Only between 665 and 681.25 nm, the error due to the interpolation increases with the AOD.

Scenario 2 shows very similar results. The largest differences between scenario 1 and 2 are again at between 665 and 681.25 nm. With the optical thickness, the effect of the wrong aerosol model used in the LUTs is increased.

Over all, even for this scenario the relative differences between the reconstructed OLCI-A radiance and the true OLCI-A radiance do not exceed 0.5 % in all bands but those which are in the gaps of OLCI-FLEX. Here, only for the cases with a thick or very thick aerosol the relative difference goes up to 1.2 %. However, in the studied scene, less than 1 % of all pixels had a reference AOD at 550 nm of more than 0.3. Hence, the cases of a thick or very thick aerosol layer occur only rarely.

In contrast to the results of the measurements during the tandem phase, we cannot observe a systematic bias over all bands for the cases of our sensitivity studies. Thus, we conclude that the difference between OLCI-B2AR and OLCI-A shown for the 2nd July 2018 (Figure 3.5 and 3.6) is not an artefact of the transfer function but a systematic difference between OLCI-FLEX and OLCI-A.

3.5.2 Surface reflectance sensitivity

The sensitivity of the description of the surface on the transfer function is studied based on the data simulated for the two scenarios of the aerosol sensitivity study. We studied the optimized surface reflectance found for the 20 cases described above. The surface reflectance retrieved
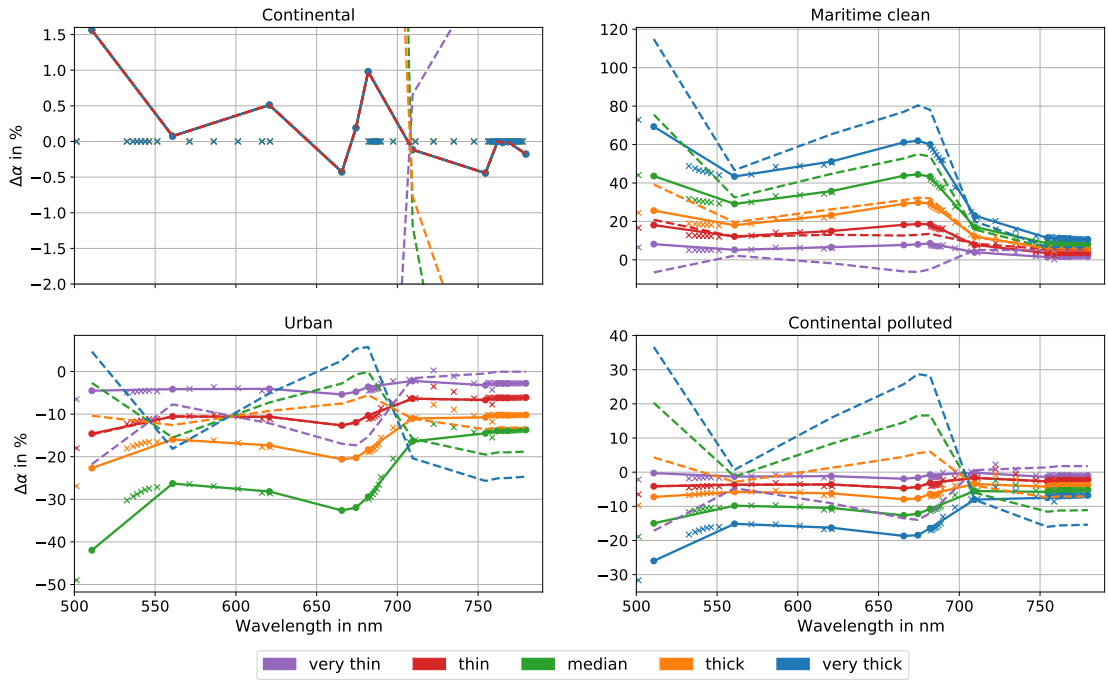
Figure 3.11   Relative difference of optimized/PCR surface reflectance compared to truth for simulations with different aerosol types. The different subplots show optimized surface reflectances with different AOT input. Solid lines: scenario 1, dashed lines: scenario 2. The reference AOD is given in Figure 3.8. Crosses mark difference between retrieved surface reflectance at OLCI-FLEX bands and truth.

for the OLCI-FLEX bands is interpolated to OLCI-A bands as described in Section 3.3.8. The difference of the interpolated surface reflectance to the truth (input for simulations) at OLCI-A bands is shown in Figure 3.11. It is calculated with

$$\Delta \alpha = \frac{\alpha_{OLCI_{AR}} - \alpha_{Truth}}{\alpha_{Truth}} * 100. \tag{3.14}$$

α represents the surface reflectance. The solid lines represent the case, where the aerosol is perfectly known (scenario 1) whereas the dashed lines show the deviation of the true surface reflectance for a retrieval based on a wrong AOD (scenario 2). Additionally, the retrieved OLCI-FLEX surface reflectance is shown for scenario 1 with cross like symbols.

Looking at the crosses in the upper left plot of Figure 3.11, the performance of the surface reflectance retrieval can be assessed. The surface reflectance was optimized under perfect conditions. Perfect conditions mean, that we know the correct spectral response functions, the aerosol, surface pressure, gas concentration, measurement geometry, and co-location. Only the *apriori* knowledge of the surface reflectance deviated from the truth. In this case, the OLCI-FLEX surface reflectance is retrieved without error. In contrast, the interpolated OLCI-A surface reflectance deviates from zero with up to 1.5 % at 510 nm. This deviation shows the limits of the transfer function for the OLCI-FLEX data set. Due to the band distributions of OLCI-FLEX and OLCI-A, a PCR is necessary to allow the interpolation which inserts this residual error. The PCR

especially fills the large gaps between 500.625 and 531.875 nm and 620.625 and 681.875 nm. For the cases of a wrong aerosol characterization, the retrieved surface reflectance at OLCI-FLEX bands deviates strongly from the truth for all three aerosol models. The strongest deviations are noticed in the case of the maritime clean aerosol whose optical properties deviate strongest from the continental aerosol model (see Figure 3.8). Accordingly, the interpolated OLCI-A surface reflectance deviates from the truth. Those effects increase with the AOD. Across the spectrum the absolute difference in the surface reflectance (not shown here) follows the shape of the surface reflectance with an increase at the red-edge. With the larger values of the true surface reflectance for wavelengths of 700 nm and more, this dependency is not shown for the relative difference due to its scaling.

In scenario 2, the relative difference of the OLCI-B2AR surface reflectance is also large. However, it shows slightly different features than in scenario 1. With a wrong characterization of the aerosol extinction, the effect of the other aerosol optical properties is either overcompensated (e.g. in case of the *Continental polluted* model) or increased (e.g. *maritime clean* model).

All in all, the large errors made for the surface reflectance are not translated in the relative difference between OLCI-B2AR and OLCI-A TOA radiances, because errors in surface reflectance and aerosol balance each other as long as they are used consistently.

The goal of the transfer function is not a perfect atmospheric correction and surface retrieval but the estimate of the bias between radiances of two satellites with different spectral responses. This goal is fulfilled as discussed in the previous sections.

3.5.3 Wavelength sensitivity

The central wavelength of OLCI's bands is known with an uncertainty of 0.1-0.2 nm. Figure 3.12 shows the effect of a 0.1 nm wavelength shift on the relative difference between reconstructed and measured OLCI-A for data from 2nd July 2018 which were presented in the previous sections. The central wavelengths were shifted plus and minus 0.1 nm. Afterwards, the complete transfer function was applied on the measured data, and the relative difference in radiance was compared with the relative difference presented in Figure 3.5 by taking the difference of the relative differences. We studied several combinations of wavelength shifts. The most pronounced shifts are presented here. In the first presented case, the OLCI-FLEX central wavelengths are shifted plus 0.1 nm and the OLCI-A wavelengths minus 0.1 nm. In the second case, we shifted the wavelengths vice versa with minus 0.1 nm for OLCI-FLEX and plus 0.1 nm for OLCI-A.

The wavelength shifts especially affects the gas absorption bands. Within the oxygen absorption band (O_2A band) around 760 nm, the difference is up to 6 %. Even though the OLCI-A bands do not cover the O_2B band between 686 nm and 688 nm, they are indirectly affected by the wavelength shift, because OLCI-FLEX bands cover the O_2B bands. A shift of wavelength results in a different retrieved surface reflectance and thus, a different reconstructed OLCI-A surface reflectance and TOA radiance. The nominal OLCI-A band at 710 nm is affected by the wavelength shift quite strong. It is located in the red edge. A small change in wavelength results in a large difference in the TOA radiance. Shifts with other combinations than the presented
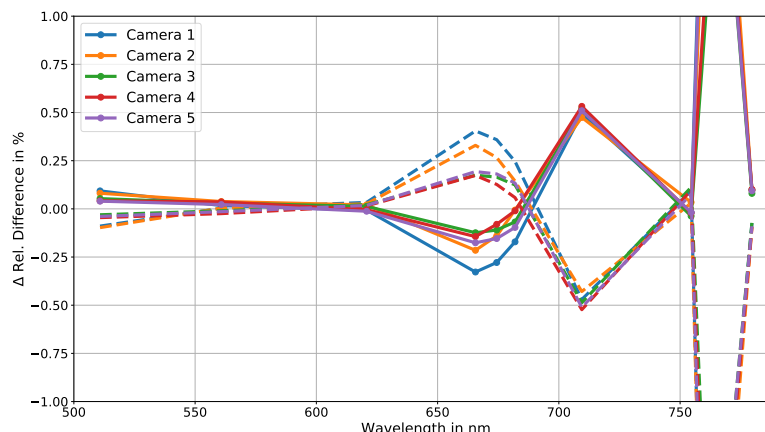
Figure 3.12   Difference of relative difference between reconstructed and measured OLCI-A with the correct central wavelength and shifted central wavelengths. OLCI-FLEX central wavelengths are shifted plus 0.1 nm and OLCI-A is shifted -0.1 nm for the solid lines. Dashed lines show the effect of a wavelength shift of minus 0.1 nm for OLCI-FLEX and plus 0.1 nm for OLCI-A. The y-axis is cut off at +/- 1 % with original maximum values of +/- 5 %.

cases show similar results.

All in all, the effect of the wavelength shift is mostly visible in absorption bands and is generally small with up to 0.5 % difference. Only the O_2A band is affected strongly. However, the difference between OLCI-FLEX and OLCI-A of about two percent throughout all cameras and most considered bands does not result from the wavelength uncertainty of 0.1 nm.

3.6 Discussion

3.6.1 Discussion of the results

The application of the transfer function on the OLCI-A/OLCI-FLEX data set of summer 2018 resulted in a direct comparison of the two data sets. We observed a relative difference in measured TOA radiance between OLCI-FLEX and OLCI-A of about 2 %. OLCI-A measured higher radiances than OLCI-FLEX. A similar difference was observed by Lamquin et al. [2020] when comparing OLCI-A and B with their original band settings. We also found a difference of about 5 % with different sign at 778.75 nm for the OLCI-FLEX-OLCI-A comparison which is not observed by Lamquin et al. [2020]. Thus, we conclude that it was not caused by an absolute calibration issue between OLCI-A and OLCI-B but by the processing from L0 to L1 of the OLCI-FLEX data. We found the same or a better continuity of the bias across the cameras, especially between Camera 4 and 5, compared to Lamquin et al. [2020]. This improvement could be the result of the improved spectral characterization of OLCI-A and OLCI-B using the time evolved spectral model. Furthermore, we observed artefacts for weak absorption bands (708.75

and 767.5 nm) across the field of view of each camera (see Figure 3.6). Those artefacts can have different reasons which neither of them is proven. Amongst other the artefacts might result from instrumental effects like a line filling due to straylight, a wrong characterization of the absorbing gas within the method or spectral characterization. Our observations are an interesting finding and should be investigated in further studies. This effect was not observed for the OLCI-A/OLCI-B comparison by Lamquin et al. [2020].

The median relative difference is a very robust measure of the overall difference between OLCI-FLEX and OLCI-A. A bootstrap method showed a high representativity of the median. Between 660 and 680 nm, where the PCR was necessary, the representativity is lower.

The results within O_2 absorption bands between 755 and 770 nm have been considered separately. The fine and deep absorption lines of O_2 must be described very accurately. The band characterization must be exact with tolerances of less than 0.1 nm. If there are small shifts in the central wavelength or the band width the characterization is not suitable for the band and the according radiance. Furthermore, only with a correct estimate of the surface pressure the depth of the O_2 absorption lines can be simulated correctly. We use the surface pressure from the L1B data which has an uncertainty of ± 10 hPa. In our results, we observe two effects within the O_2 absorption bands. In the strong absorbing bands at 761.25 and 764.375 nm of OLCI-A, the median difference between OLCI-A and OLCI-B2AR fluctuates across the detectors, which could be a result of imprecise wavelength characterization. The fluctuations are much smaller than the ones observed by Lamquin et al. [2020], who did not use the time-dependent wavelength characterization. Hence, the used characterization of the oxygen absorption band is an improvement. The second effect visible in the results is the strong gradient of the relative difference with the wavelength starting at 761.25 nm. This effect cannot be explained by the O_2 band, as both strong and weak absorbing bands (764.375 and 767.5 nm) show a similar relative difference which differs from the overall bias between OLCI-A and OLCI-FLEX of about minus 2 %. The last OLCI-A band at 778.5 nm is not influenced by O_2 absorption but it shows a relative difference of plus 5 %. The change in sign of the relative difference with the wavelength at the edge of the spectrum probably originates in the processing form L0 to L1 of OLCI-FLEX. The uncertainty and sensitivity analysis showed that the identified measurement and model uncertainties have only a small effect on the result of the transfer function. They cannot explain the relative difference between OLCI-A and OLCI-FLEX radiances. Thus, we could identify actual systematic differences of measurement from the two instruments during the special configuration.

3.6.2 Discussion of the method

The application of the transfer function on the OLCI-FLEX and OLCI-A data from the Sentinel-3 tandem phase showed a sensitivity to a confirmed systematic bias between OLCI-FLEX and OLCI-A. Additionally, we could reveal processing issues. The success of the transfer function relies on accurate radiative transfer simulations, an accurate spectral characterization and the accurate description of the environment.

The parameter with the strongest impact is the surface reflectance. The surface reflectance especially that of vegetated ground has many spectral features which influence the radiance measurements strongly. To transfer the surface reflectance from one band setting to the other, the spectral features covered by both instruments must be measured by the high-resolution instrument. As this was not the case for OLCI-FLEX setting, for OLCI-A bands between 660 and 680 nm additional information was introduced using a PCR. The quality of the PCR determines the quality of the transfer function and introduces uncertainty to the method.

Besides the surface, the atmospheric conditions influence the radiance measurement and thus, the quality of the method. Gas absorption lines are distinct spectral features that affect only bands with central wavelength close to those features. Within the visible spectrum, water vapour and oxygen absorption are most prominent. The depth of the absorption lines depends on the total column water vapour and the surface pressure. Both terms must be well characterized to eliminate misinterpretation of differences that are only caused by errors in the atmospheric characterization.

In contrast, the aerosol description is less important as it is smooth within the visible spectral range. A wrong characterization of the aerosol results in an over- or underestimation of the surface which is continuous over the complete spectrum. Due to the consistency of the assumptions about the environment among OLCI-FLEX and OLCI-A data sets, the possible misinterpretation of the surface has only a small effect on the validity of the estimated bias.

The sensitivity study showed a residual error in the relative difference of up to 0.5 % which originate from the interpolation of the surface. This uncertainty will be reduced when the transfer function is applied to the FLEX mission. The interpolation will be more accurate due to the high resolution and high spectral coverage of FLORIS.

The presented method has two limitations: 1) no pixel by pixel comparison and 2) a direct uncertainty measure is only possible for the lower resolution band set. Instead of a pixel wise comparison, we performed a statistical evaluation to mitigate the effects of imprecise co-location and missing information between 660 and 680 nm. The study area of Europe is characterised by a heterogeneous surface. Slight misalignment of the pixel causes different TOA signal due to the difference in the surface. Those uncertainties can be reduced taking medians over large numbers of pixels. Homogeneous areas such as deserts or oceans could be studied and used for a pixel by pixel comparison. The OLCI-FLEX data set from the tandem phase in 2018 did not cover such areas. Thus, the transfer function could not be applied on measurements over deserts or oceans.

The second limitation is that the uncertainty estimate of the lower spectral resolution instrument cannot be transferred back to the high-resolution spectrum. Thus, only an overall estimate of the agreement of the two instruments is possible. In case of OLCI-A and OLCI-FLEX, OLCI-A is a very well characterised and validated instrument. A bias between OLCI-A and OLCI-B is known. Consequently, we assume that the radiometric calibration of OLCI-FLEX is correct and the observed difference to OLCI-A corresponds to the difference between OLCI-A and OLCI-B. The exception is the bias for wavelengths larger than 760 nm.

3.7 Conclusions

In this article, we showed systematic differences between OLCI-A and OLCI-FLEX during the tandem phase of Sentinel-3A and -3B, consistent with known radiometric differences between OLCI-A and OLCI-B. The comparison is sensitive to measuring errors and processing issues. In this paper, we showed the application of the transfer function for comparing measurements of satellites flying in tandem formation. An advantage of a tandem mission is the observation of the same geographic target under the same environmental conditions. Further tandem missions are planned for which the transfer function could be applied. One of them is another Sentinel-3 tandem mission. This mission could be used to study the settings of FLEX even further. With reprogrammed band settings that better cover the original OLCI settings, the PCR can be omitted and the surface reflectance can be described more robust. An other tandem mission is the coming FLEX-Sentinel-3 mission. The transfer function can be used for the quality control of especially the lower resolution bands between 500 and 677 nm. The higher resolution bands can be most probable directly convolved with OLCI spectral response functions to be comparable with the corresponding OLCI radiance measurements.

The method is not limited to tandem missions. Satellite-satellite comparisons for satellites with different overpass times can be compared too. The requirements for such comparison are a well described atmosphere and surface for both overpasses, an accurate spectral characterization of both instruments and knowledge about the observation and sun angles that need to be considered in the radiative transfer simulations. Additionally, bidirectional surface reflectance effects must be taken into account. When all those requirements are fulfilled, the transfer function allows a comparison among satellites with different spectral settings which can be conducted anytime and which does not need certain target areas. A constant quality check between two instruments with different band settings is possible and thus, an inter-operational product can be generated and quality controlled. With such inter-operational products, we can exploit the potential information content of the existing satellites even further [Niro et al., 2021].

Beside the comparison of between satellite-satellite data, further applications of the transfer function are possible. It can be applied to transfer information gained at TOA from satellites down to BOA data or vice versa. Thus, a comparison of satellite based with ground-based or aeroplane-based radiance measurements is possible. During the Sentinel-3A and B tandem phase in 2018, simultaneous experiments were realized comprising both ground and airborne measurements. The introduced transfer function could be applied on this data set to increase the level of quality control of the described data set.
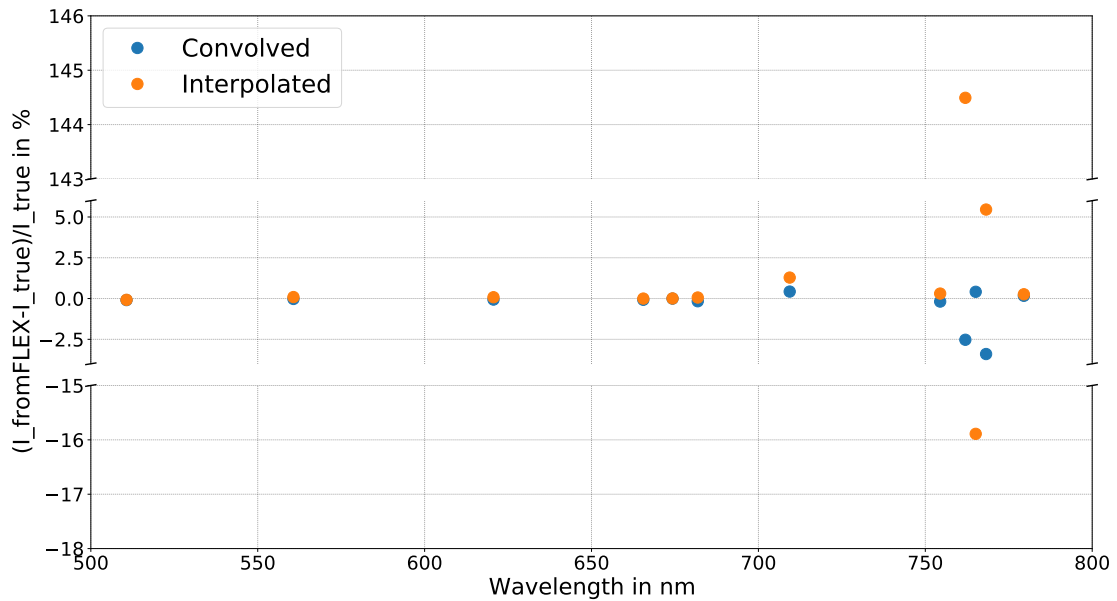
Figure 3.13   Difference between "true" OLCI TOA radiance and OLCI radiance reconstructed from FLEX TOA radiance by convolution with OLCI spectral response function (blue) and by interpolation (orange). "True" OLCI TOA radiance is high resolution transmission from HITRAN convolved with OLCI spectral response function.

3.8 Addendum

The following section is not part of the published paper. For the sake of completeness, a small study on the band distribution of FLORIS is presented. The study focuses on the suitability of the band distribution to compare FLORIS L1 data with OLCI L1 data. The tandem constellation of S3 and FLEX will enable a comparison of the TOA radiance for validation purpose. OLCI and FLORIS will have the same spatial but different spectral resolutions. The spectral characterizations of OLCI and FLORIS are shown in Table 3.1. The spectral sampling of FLORIS varies between 0.1 and 2 nm and its band widths ranges between 0.3 and 3 nm [Coppo et al., 2017]. We tested whether it is sufficient to interpolate or to convolve the FLORIS measurements to OLCI's spectral response functions in order to overcome the difference in spectral responses.

For this test, the high resolution transmission spectra of water vapour and oxygen from HITRAN 2016 [Gordon et al., 2017] are convolved with the spectral response functions of OLCI and of FLORIS. Those spectra serve as truth. Then, the FLORIS transmission spectrum is transferred to an OLCI spectrum by either interpolating or by convolving with spectral response functions from OLCI. The difference between the convolved/interpolated OLCI spectrum and the "true" OLCI spectrum is shown in Figure 3.13.

Within the spectral range between 500 and 700 nm, both convolution and interpolation of the FLORIS data could translate the transmission at the FLORIS bands to transmission at OLCI spectral bands with differences compared to the truth smaller than 0.2 %. Interpolation within the oxygen band results in large differences of up to 145 % between the transmission from FLORIS and the true OLCI spectrum. The convolution results in errors of up to 3.5 %. The
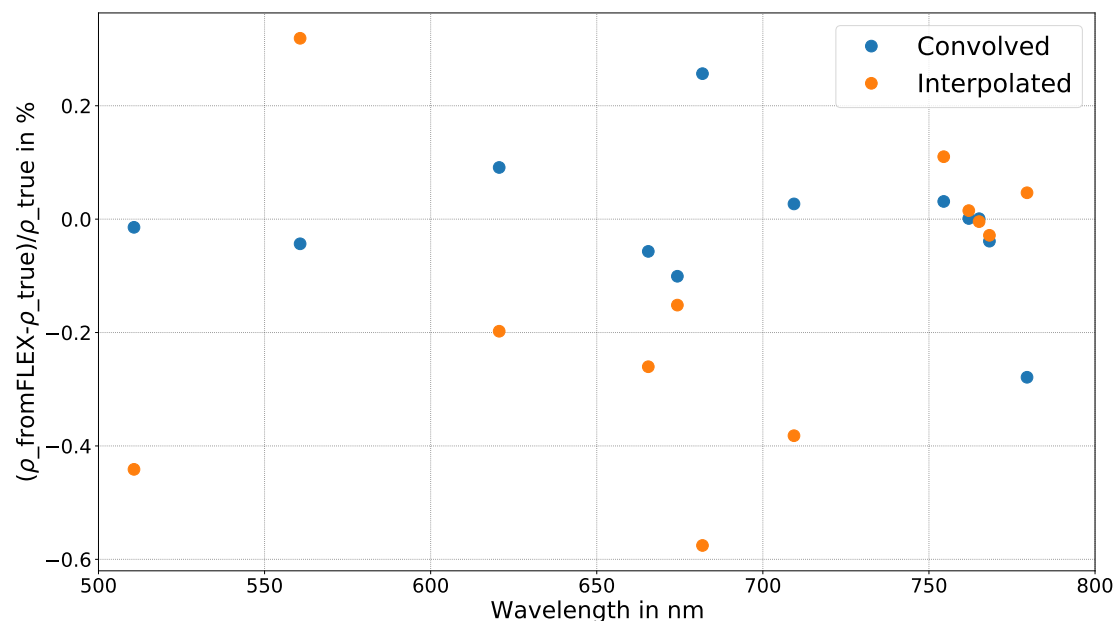
Figure 3.14   Difference between "True" OLCI vegetated surface reflectance and OLCI surface reflectance reconstructed from FLEX surface reflectance by convolution with OLCI spectral response function (blue) and by interpolation (orange). "True" OLCI vegetated surface reflectance is high resolution spectrum from ASTER [Baldridge et al., 2009] convolved with OLCI spectral response function.

strong and sharp absorption lines of the oxygen A band could not be reproduced by the spectral sampling of 0.1 nm of FLORIS. Thus, the spectral resolution of FLORIS in the O_2A band is not high enough to enable a comparison between OLCI and FLORIS for validation purpose by transferring the measurements neither by interpolation nor by convolution. Instead, a transfer function as presented in Chapter 3 must be applied. The spectral resolution of FLORIS is adequate to either convolve or interpolate transmission from FLORIS band settings to OLCI band settings for the OLCI bands between 500 and 700 nm.

For a successful satellite-satellite comparison of sensors with different spectral response using a transfer function, the distribution of the high resolution bands at the different features of the surface reflectance spectrum of vegetated surfaces is important. Figure 3.14 shows the difference between a surface reflectance spectrum of deciduous forest from the ASTER data base [Baldridge et al., 2009] at OLCI bands and at OLCI bands reconstructed from the FLORIS surface reflectance spectrum by interpolation and convolution. The interpolation of the FLORIS surface reflectance results in differences to the truth between 0.2 and -0.6 %. When convolving the FLORIS spectrum with OLCI spectral response function, the uncertainty is less than 0.3 %. In Section 3.5.2, we showed that differences in the surface reflectance description are directly translated in differences in TOA radiance if not compensated with an according aerosol description. Hence, additional information about the surface from a PCR is not necessary when comparing OLCI with FLORIS TOA radiances. The uncertainty of an insufficient description of the surface measured at the high resolution instrument as shown for the OLCI-A/OLCI-FLEX comparison (see Figure 3.10 and 3.11) is reduced by the high resolution measurement of FLORIS.

4

Ground-based validation of the surface reflectance

---

[1]Institute of Meteorology, Freie Universität Berlin (FUB), Carl-Heinrich-Becker-Weg 6-10, 12165 Berlin, Germany

4.1 Abstract

The Fluorescence Explorer (FLEX) satellite will carry the high resolution Fluorescence Imaging Spectrometer (FLORIS) that measures the complete fluorescence spectrum emitted by chlorophyll of terrestrial vegetation. A validation approach for the small fluorescence signal is to compare the retrieved surface reflectance with ground-based measurements. However, the difference in spatial resolution of the satellite and ground-based instruments and a geolocation mismatch will result in differences in the detected signal and thus, in uncertainties of the validation strategy.

We define requirements of representativeness for a validation ground site in vegetated areas. Based on those requirements, we identify a suitable position within a case study in central Italy using surface reflectance data from the airborne High-Performance Airborne Imaging Spectrometer (HyPlant) measured in summer 2018. The representativeness is quantified by the relative difference between the single HyPlant pixel representing a ground-based measurement and the averaged signal of several HyPlant pixels that mimics a FLORIS pixel. With this measure, we quantify the validation uncertainty due to spatial resolution and geolocation mismatch. The effect of the temporal evolution of the surface properties on the validation uncertainty due to spatial resolution is investigated.

We select the ground site position by minimizing the validation uncertainty due to spatial resolution. Especially for wavelengths larger than 700 nm, this uncertainty is smaller than 2 % for all different reference areas. The largest differences between ground-based like measurement and satellite-like measurement of the surface reflectance is due to geolocation mismatch. The uncertainty due the geolocation mismatch is very large for wavelengths smaller than 720 nm and moderate for wavelengths larger than 720 nm. Thus, the surface reflectance at the chosen position for the validation site is not homogeneous enough for validation purpose. Considering a reference area of 13.5x13.5 m^2, we quantify temporal stable and small uncertainties for the spectral range between 720 and 800 nm. For an all-embracing validation of the surface reflectance of vegetated areas, the chosen site is not appropriate.

4.2 Introduction

European space agency's (ESA's) 8th Earth Explorer satellite, the Fluorescence Explorer (FLEX), will deliver the complete fluorescence spectrum [Drusch et al., 2017]. The fluorescence signal is a small signal emitted by plants which is a by-product of photosynthesis. Thus, it is a proxy of plant growth and productivity. The estimation of plant activity on a global scale can contribute to quantify carbon dioxide sinks and to monitor food supply. To retrieve fluorescence from TOA radiance measurements, the instrument must be well calibrated and the atmosphere must be well characterized. Hence, validation of the measurements is important to avoid misinterpretation of the signal [Rossini et al., 2022, Buman et al., 2022]. Validation is necessary as many uncertainty sources are not known or quantified [Wu et al., 2019].

Possible validation strategies are comparing satellite-satellite measurements as done by [Jänicke

et al., 2023] or comparing satellite with ground-based or airborne measurements. In any case, the same environmental conditions must be observed by similar measurement set-ups. However, satellite sensors have a coarse spatial resolution compared to ground-based measurements (e.g. FLEX: 300x300 m^2 [Drusch et al., 2017]). This difference in spatial resolution must be considered within the validation of the TOA signal. Gao et al. [2023] quantified the uncertainty due to heterogeneity and different spatial resolutions for a study case in China. They compared the surface reflectance from different surface types measured at a spatial resolution of 2x2 m^2 and at 30x30 m^2. Du et al. [2023] presented recently the first approach of direct validation of fluorescence products from space. Nevertheless, they could not resolve issues of uncertainties due to difference in spatial scale [Du et al., 2023].

One possible validation for FLEX is estimating the uncertainty of the surface reflectance. The surface reflectance signal contains the fluorescence signal. The atmospheric correction can be also assessed by the quality of surface reflectance [Sabater et al., 2017]. A valid atmospheric correction is the key component of the fluorescence retrieval [Cogliati et al., 2015]. Furthermore, for climate change studies accuracy of surface reflectance should be better than 5% [Ohring et al., 2005]. With validation, the uncertainty of the surface reflectance can be quantified.

Wu et al. [2019] summarized possibilities of handling the difference in spatial resolution using ground-based measurements for satellite validation. Those possibilities are: 1) The gap of information can be bridged with airborne measurements. 2) An upscaling method can be applied. 3) The surface reflectance can be measured at several ground-based sites within one satellite pixel and a multi-point-to-point method can be applied. 4) A point-to-area consistency analysis can be performed. 5) The triple collocation error model can be applied. All methods have their disadvantages, e.g. upscaling maps must include the seasonal and man-made changes of landscape and, measuring at difference sites is labour intense and difficult to synchronize with satellite observations [Wu et al., 2019]. The possibility of applying the multi-point-to-point method for the FLEX fluorescence product validation is evaluated by Rossini et al. [2022]. They used High-Performance Airborne Imaging Spectrometer (HyPlant) data from Italy to estimate the number of ground sites which are necessary to enable validation of satellite fluorescence product. 3-13.5 sample points within one satellite pixel are needed for an accurate validation [Rossini et al., 2022]. However, they did neither investigated the uncertainty due to geolocation mismatch nor the spectral dependence of the uncertainty. De Grave et al. [2021] validated another vegetation parameter, the leaf and canopy chlorophyll content, based on upscaling a map derived from HyPlant measurements.

Commonly, validation efforts are done over homogeneous areas like deserts, dried lakes, oligotrophic oceans or deep convective clouds. However, validation over homogeneous sites is not representative for world wide large number of heterogeneous areas. Thus, more validation stations at heterogeneous places are necessary [Wu et al., 2019]. Furthermore, to validate vegetation indices like fluorescence, vegetated validation sites are needed which are usually heterogeneous areas [Buman et al., 2022].

During the Sentinel-3A and -3B tandem phase, the Ocean and Land Colour Imager (OLCI) on Sentinel-3B was reprogrammed to mimic FLEX [ESA, 2021b]. Simultaneously, ground-based

(Fluorescence box (FLOX)[JB Hyperspectral Devices GmBH, 2023]) and airborne (HyPlant [Siegmann et al., 2019]) radiation measurements were collected to validate the satellite data and help interpreting them during the ESA-funded FLEXSense campaign [ESA, 2024]. The experimental sites were chosen to observe vegetated surfaces close to measurement infrastructure which constrains other environmental parameters. Those sites were in western Germany close to Jülich, southern France at Haute-Provence Observatory (OHP), western Spain at Majadas de Tiétar, northern Switzerland close to Lägeren and central Italy near Grosetto. All those stations are surrounded by characteristic European inhomogeneous landscape with small patches of forest and agricultural fields. To use this dataset for validation purpose and to define requirements for validation strategy for FLEX, the impact of inhomogeneity is studied in this paper. Inhomogeneity reduces the representativeness of a ground-based measurement with respect to the satellite pixel. Furthermore, the uncertainty of the geo-referencing of the satellite pixel could result in large differences between satellite measurement and ground-based measurement which is more pronounced for inhomogeneous sites. In this study, we select an exemplarily representative place for a ground station and characterize the uncertainty of the surface reflectance validation with ground-based measurements due to the difference in spatial resolution and in geolocation mismatch. Furthermore, the temporal evolution of the uncertainty is investigated. With this study, we want to contribute in finding a validation strategy for FLEX which is not yet defined [Rossini et al., 2022]. We evaluate, if a direct comparison of surface reflectance measured at the selected ground site with the surface reflectance retrieved from satellite measurements is possible after quantifying the discussed uncertainties. Additionally, the associated TOA radiance is simulated for the example case. From this simulation, the effect of the difference in the surface reflectance from satellite and ground-based measurement due to their difference in spatial resolution on the TOA radiance is assessed.

The methods are presented in Section 4.3. The methods section includes the description of the data, the radiative transfer simulations, and the definition of the requirements for the selection of a suitable ground site. In Section 4.4, the results are presented. The results are summarized and discussed in Section 4.5. A conclusion is drawn in Section 4.6.

4.3 Methods

The goal of this work is to support the choice of a validation ground site in order to maximize its representativeness. The accuracy of the surface reflectance validation with ground-based measurements depends on the representativeness of the surface reflectance of the ground site area with respect to the surface reflectance of the georeferenced satellite pixel. The difference between the surface reflectance retrieved from satellite and ground-based measurements due to their difference in spatial resolution induces an uncertainty for the validation of the surface reflectance. This uncertainty is estimated using airborne measurements of the surface reflectance with HyPlant. HyPlant has a high spatial resolution and due to the scanning with the aeroplane, the spatial coverage is also high. We use averages of many HyPlant pixel over satellite pixel-
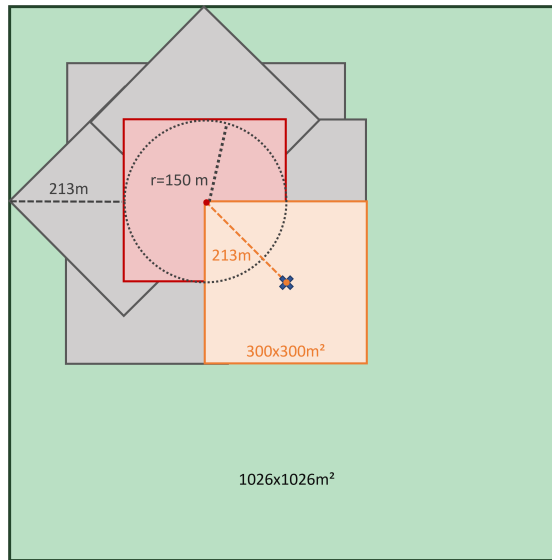
Figure 4.1   Schematic overview of possible position of satellite pixel with a coverage of 300x300 m^2 with respect to a ground site marked with the cross. The orange centre of the orange square matches the ground site perfectly. The red square shows one of the satellite pixel which is furthest away from ground site. The grey circle gives the geolocation uncertainty of the red pixel (150 m). All grey squares show possible true positions of the red pixel. The green square of the size 1026x1026 m^2 shows the needed homogeneous area to cover all those possible positions.

like areas and compare them to areas observed by a few HyPlant measurements which mimic ground-based measurements. Thus, we can compare measurements of the same radiometric and spectral set-up but different spatial resolutions without introducing other uncertainties due to calibration, georeferencing and observation geometry. In the following, we refer to the averaged HyPlant measurement that covers a satellite-pixel like area as satellite surface reflectance or satellite measurement even though it originates from HyPlant. Likewise, the HyPlant measurement that mimics the ground truth is called ground-based surface reflectance or ground-based measurements.

Besides the spatial resolution of the satellite pixel, also its geolocation determines the measured signal. Within the georeferencing of the satellite pixel to the ground site, usually the satellite pixel with the closest geolocation to the ground site is selected. Due to its spatial resolution, the centre of the closest satellite pixel can have a distance of about 210 m to the ground site when assuming a satellite pixel of 300x300 m^2. Furthermore, the geolocation of the satellite pixel has an uncertainty. The Fluorescence Imaging Spectrometer (FLORIS) carried by FLEX should have an uncertainty in geolocation of maximum 0.5 pixel [Drusch, 2018]. Thus, the signal from the satellite pixel associated to the ground site measurement might originate from an area with a centre that has a distance of up to 360 m for a FLEX like pixel. Figure 4.1 shows schematically a ground site (marked as cross) and possible georeferenced satellite pixels (in orange and red). The centre of the orange satellite pixel matches the ground side perfectly. The centre of the red pixel is one of the possible georeferenced pixels that is furthest away from the ground

site. Its geolocation uncertainty is given as grey cycle which marks all possible true positions of the centre of the red pixel. Some of the according pixels are indicated as grey squares. They can also be twisted. To validate any georeferenced satellite measurement with the ground-based measurement, the ground site must be representative for an area of 1026x1026 m^2 (green area in Figure 4.1).

In Figure 4.1 as well as in this study, we assume a square point spread function. We refer to the distance between the true centre of the satellite pixel and the ground site as geolocation mismatch. The difference in the surface reflectance due to the geolocation mismatch also results in an uncertainty of its validation comparing satellite and ground-based measurements.

This uncertainty is also estimated in this study. Here, the centre of the satellite-like areas are shifted from the exemplary ground site. We determine the surface reflectance for satellite-like areas from HyPlant measurements with distances between the ground site and their centre of up to 205 m. Those surface reflectances are then compared with the surface reflectance at the ground site.

The representativeness can change over time. In order to achieve the aim of this study, the flight lines of different days are evaluated and the uncertainty of the validation due to difference in spatial resolution is compared.

The effect of the discussed uncertainties on the TOA radiance is also studied. The difference in surface reflectance due to the difference in spatial resolution is translated in a difference in TOA radiance by simulating a TOA radiance. One simulated TOA radiance spectrum is based on the ground-based surface reflectance and the other simulation is based the satellite surface reflectance. Again, all surface reflectance measurements are taken from HyPlant measurements.

4.3.1 Data

In this study, we use aeroplane overpasses over a ground-based site in the north-west of Grosseto in Italy on 10/06/2018, 19/07/2018, 30/07/2018 and 31/07/2018. On each day several flight lines were performed at a flight height of 3050 m above ground. The aeroplane carried the HyPlant instrument developed by Forschungszentrum Jülich in cooperation with Specim Ltd. (Oulu, Finland). HyPlant is a high resolution spectrometer whose two modules cover a spectral range between 370 and 2510 nm [Siegmann et al., 2019]. We study only the visible and near infrared range between 500 and 800 nm which can be compared with future FLORIS measurements. The aperture of a single pixel is 0.084 degrees which results in a spatial resolution of 4.5x4.5 m^2 for the given flight height.

We study the temporal stability of the validation uncertainty by taking the flight line from the 30/07/2018 at 11:35 local time as reference measurement. The overpasses from 10/06/2018 at 13:14, 19/07/2018 at 12:46 and 31/07/2018 at 13:01 are evaluated to show the temporal variability of the surface reflectance. The true colour image of the flight line from the 30/07/2018 is shown in Figure 4.2.

The surface reflectance has been calculated using the processing chain based on an atmospheric
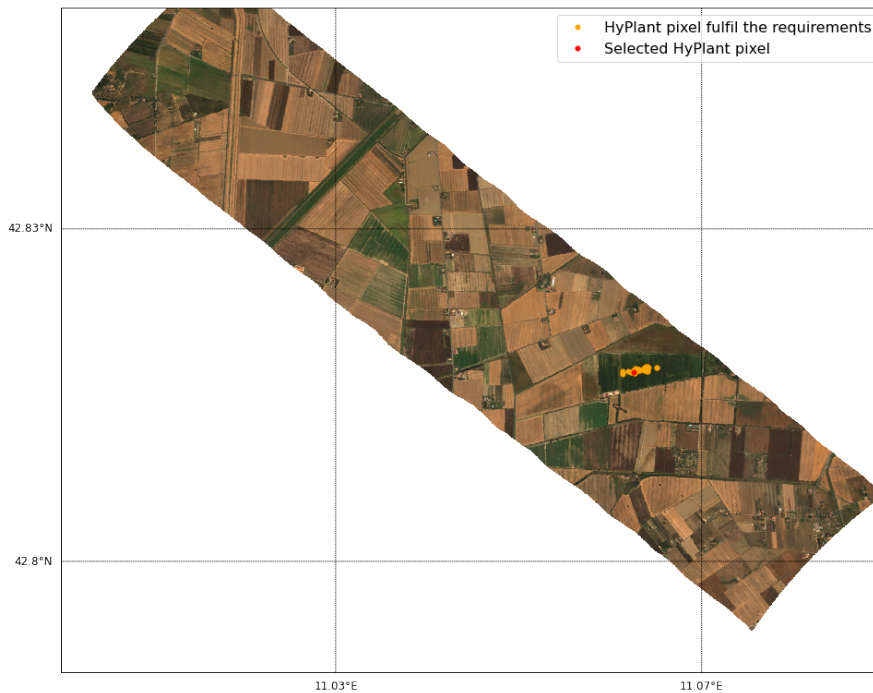
Figure 4.2   True colour image from HyPlant overpass north-west of Grosseto-Italy on 30/07/2018 with oranges point marking all pixels which fulfil the defined requirements for a ground site and in red the pixel with the smallest difference in surface reflectance due to differences in spatial resolution (Requirement 1).

correction using the commercial software Atmospheric and Topographic Correction algorithm (ATCOR) [Siegmann et al., 2019]. To estimate the uncertainty of the validation of the surface reflectance by comparing measurements with different spatial resolution, a FLEX pixel is mimicked averaging 67x67 HyPlant pixels. Those pixels cover an area of approximately 300x300 m^2. The exact point spread function of FLORIS is not yet known. Thus, we only assume the spatial resolution of 300x300 m^2, as it is given in Drusch [2018], and a quadratic shape. However, even if the actual point spread function deviates from this assumption, this method is still applicable after small adaptions. The averaged signal is compared to a HyPlant measurement that is representative for a ground-based measurement. The choice of the number of HyPlant pixel that are representative for the ground measurement is detailed in the next paragraph.

The fluorescence box (FLOX) was developed and is distributed by JB Hyperspectral Devices GmBH [2023]. It measures up- and downwelling radiance with the same spectral range as FLORIS. Thus, it is suitable for ground-based comparison measurements. FLOX has an aperture of 20 degrees facing downwards. Depending on its installation height, FLOX covers different ground areas. A FLOX mounted on a tower at 12 m height represents a 4.5x4.5 m^2 HyPlant pixel. The list of spatial coverage and the according heights are given in Table 4.1.

Table 4.1   Number of HyPlant pixel for a flight height 3050 m above ground and the height of FLOX necessary to cover the same area with FLOX measurements.

Number of HyPlant pixels	Area in m^2	FLOX height in m
1	4.5x4.5	12
3x3	13.5x13.5	38
5x5	22.5x22.5	64
7x7	31.5x31.5	89
9x9	40.5x40.5	115
67x67	301.5x301.5	850

4.3.2 Radiative transfer simulations

In order to provide a TOA radiance, the ground-based measured surface reflectance as well as the satellite based surface reflectance serve as input of radiative transfer simulations. A standard mid-latitude summer atmospheric profile [Anderson et al., 1986] and an isotropic surface are assumed for the simulations. Furthermore, no 3D effects are considered. The estimated TOA radiance for the two different spatial resolution can be set in relation to estimate the effect of the spatial resolution on the TOA radiance.

The simulations are performed with the radiative transfer model MOMO developed at Freie Universität Berlin [Fischer and Grassl, 1984, Fell and Fischer, 2001, Doppler et al., 2014a, Hollstein and Fischer, 2012]. It is based on the matrix operator method combined with adding and doubling method. The underlying surface is approximated as isotropic reflecting and the atmosphere is divided in plane-parallel homogeneous layers. The high resolution gas transmission spectrum is binned in groups of similar transmission values based on a k-binning algorithm [Doppler et al., 2014b]. A continental aerosol model is chosen from the OPAC data base [Hess et al., 1998]. The simulations are done at the 45 OLCI bands when it was in FLEX configuration.

4.3.3 Requirements for the selection of ground-based position for FLEX validation

The requirements for a ground-based measurement site are: 1) minimized uncertainty due to spatial resolution, 2) homogeneity within the satellite pixel and 3) vegetated surfaces. We estimate the uncertainty due to spatial resolution by relating the satellite like pixel areas to a FLOX pixel area. The relative difference of the averaged (satellite pixel-like) and the single pixel (ground-based like) measurement quantifies the uncertainty due to the difference in spatial resolution. We estimate the representativeness of a ground site only for a 300x300 m^2 area due to the small scale structure of our study area. The ground-based measurements should be used to validate the complete spectral range. Thus, the difference should be small across the complete spectrum. We select three wavelength sampling points to minimize the difference. We chose the spectral sampling points of HyPlant at $\lambda = 550, 670$ and 800 nm which are located at the chlorophyll

reflection peak, and right and left of the red edge. The first requirement is

$$mean(\Delta\rho) = \frac{\sum\limits_{i=0}^{n} \frac{|\rho_{4.5x4.5m^2}(\lambda_i) - \rho_{300x300m^2}(\lambda_i)|}{\rho_{4.5x4.5m^2}(\lambda_i)} * 100}{n} < 3.5\% \tag{4.1}$$

$\rho_{300x300m^2}$ and $\rho_{4.5x4.5m^2}$ are the surface reflectances of the $300x300m^2$ area and of the $4.5x4.5m^2$ area, respectively. n is the number of wavelength sample points, which is three in this study. The homogeneity within a $300x300 \ m^2$ area is quantified by the standard deviation of all N HyPlant pixels within the according area. The standard deviation should be also small across the spectral range between 500 and 800 nm. We calculated the standard deviation at the same spectral sampling points as above. The second requirement is

$$mean(\sigma) = \frac{\sum\limits_{i=0}^{n} \sqrt{\frac{\sum\limits_{j=0}^{N} (\rho_{4.5x4.5m^2,j}(\lambda_i) - \rho_{300x300 \ m^2}(\lambda_i))^2}{N}}}{n} < 0.02. \tag{4.2}$$

The third requirement allows only vegetated pixels. The normalized difference vegetation index (NDVI) is used to select vegetated pixels. Here, it is defined as

$$NDVI = \frac{\rho(650 \ nm) - \rho(800 \ nm)}{\rho(650 \ nm) + \rho(800 \ nm)} > 0.7. \tag{4.3}$$

4.4 Results

4.4.1 Selection of ground-based position for FLEX validation

Those requirements are applied to the reference flight line at 11:35 local time on 30/07/2018. Figure 4.2 shows the true colour image from HyPlant of this flight line and the pixel that fulfil all three requirements are shown in orange. The pixel with the smallest relative difference is shown in red. Within this flight line, only one agricultural field is homogeneous enough and vegetated at the same time. The red marked pixel with the smallest relative difference is selected as location of a possible ground site for further studies. Its coordinates are 42.81706^o N, 11.062584^o E.

4.4.2 Quantification of validation uncertainty due to difference in spatial resolution

The validation uncertainty due to the spatial resolution for the selected pixel is determined by taking the relative difference of the averaged surface reflectance of a $300x300 \ m^2$ area and surface reflectances of several reference areas that can be associated with ground-based measurements. Both values are measured by HyPlant at the same time and the same central position (42.81706^o N, 11.062584^o E). Thus, uncertainties due to differences in spectral calibration, ge-
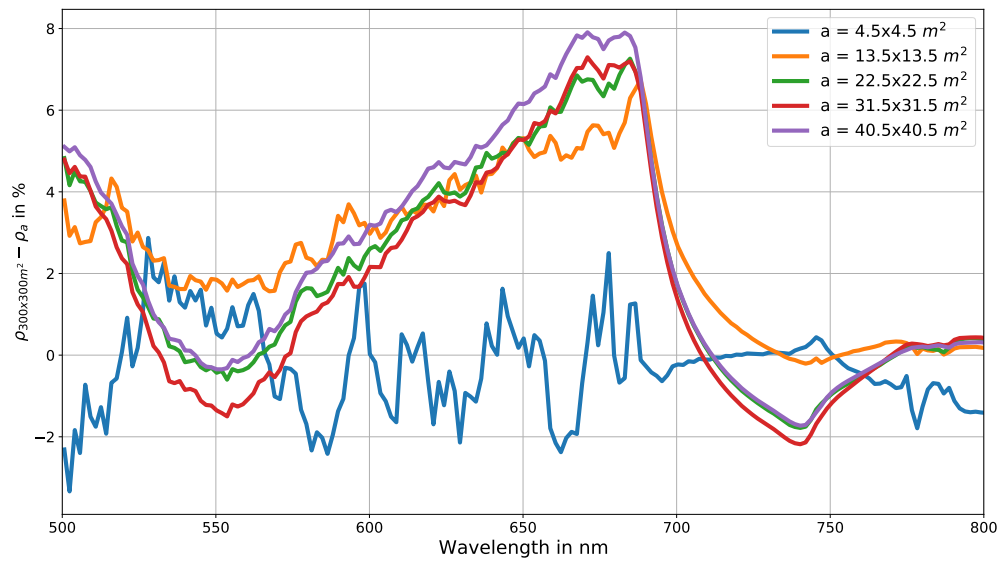
Figure 4.3   Relative difference between surface reflectance average over 300x300 m^2 and areas between 4.5x4.5 and 40.5x40.5 m^2 measured from HyPlant at 42.81706^o N, 11.062584^o E on 30/07/2018.

olocation mismatch, or atmospheric differences are eliminated. The relative differences across the spectrum are shown in Figure 4.3. The difference between the satellite like measurement and the surface reflectance from one pixel (in blue) oscillates around the zero line with largest differences of $\pm 3\%$. Thus, we found a pixel that is representative for a satellite pixel area within that specific flight line. In case of larger ground-based measurement areas, we find differences of up to 8%, which are comparable across the spectrum for the areas between 13.5x13.5m^2 and 40.5x40.5m^2. The larger reference areas show the same systematic feature with minima at 550 nm and 740 nm, a strong maximum at 680 nm and a relative difference of almost zero between 780 and 800 nm. The surface reflectance of the area of 13.5x13.5m^2 represents the satellite pixel well with differences smaller than 0.5% between 720 and 800 nm.

Even though the standard deviation across the satellite area is smaller than 0.02, the selected pixel is not representative of its surrounding pixels. Hence, the determined uncertainty is only valid for this exact position and size.

4.4.3 Quantification of validation uncertainty due to geolocation mismatch

The uncertainty due to geolocation mismatch is determined by evaluating the differences between satellite-like measurements with different central positions and the ground-based measurement. We take the average of 67x67 HyPlant pixels for all central pixels that are within the 67x67 HyPlant pixels centred at the selected position. In Figure 4.1, this area is marked in orange. All those averaged surface reflectances could be satellite measurements, that are georeferenced to the selected positions in case of perfectly known geolocations of the satellite pixels. The difference of those averaged surface reflectances to the surface reflectance of the 4.5x4.5 m^2
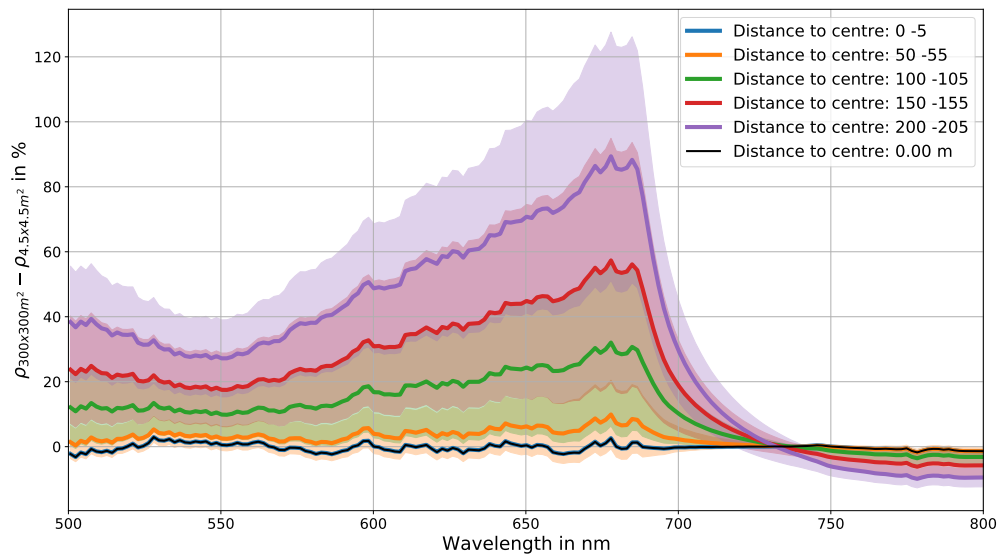
Figure 4.4 — Relative difference between surface reflectance average over 300x300 m^2 and 4.5x4.5 m^2 measured from HyPlant at 42.81706^o N, 11.062584^o E on 30/07/2018. The 300x300 m^2 area is chose with different offsets of its central position and the central position of the 4.5x4.5 m^2 area.

pixel are shown in Figure 4.4. Differences of pixels with similar distances to the selected position are binned and the mean of each bin is plotted in a different colour. The shaded areas give the standard deviation within each bin. For satellite-like pixels with a distance of the centre to the selected position between 50 and 55 m, the relative difference in surface reflectance due to spatial resolution and geolocation mismatch is smaller than 10 % with standard deviation of another 10 % at 680 nm. At those smaller wavelengths and with larger distances, the differences have maximum values of more than 80 %. For vegetated surfaces, the surface reflectance is small at wavelengths smaller than 700 nm. Thus, small absolute differences result in large relative differences. At wavelengths larger than 750 nm, the relative difference is smaller than 10 % with small standard deviations of about 2 to 5% for all distances. It is remarkable that all differences are positive on the left of the red edge and negative on the right. This patterns shows us, that we chose a particular green and vegetated ground site. Looking at the true colour image in Figure 4.2, we can see, that when choosing satellite pixels with larger distance to the ground site also non-vegetated areas are considered. Those surface reflectances are larger at wavelengths between 500 and 720 nm and smaller between 720 and 800 nm compared to the green ground site surface reflectance.

4.4.4 Temporal evolution of validation uncertainty due to difference in spatial resolution

So far, we estimated the uncertainties due to spatial resolution and geolocation mismatch only for one day. To generalize the uncertainty estimate, we calculate the uncertainty due to spatial resolution for HyPlant overpasses at different days. The true colour images of the different over-
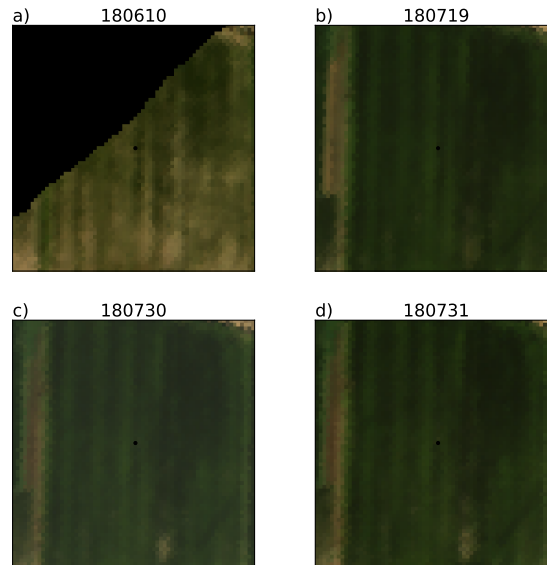
Figure 4.5 True colour image from HyPlant of 300x300 m^2 area with central position at 42.81706^o N, 11.062584^o E on a) 10/06/2018, b) 19/07/2018, c) 30/07/2018 and d) 31/07/2018.

passes at the selected position and the 300x300 m^2 surrounding area are shown in Figure 4.5. The flight path in June does not cover the complete area. However, we can observe larger differences in the vegetation coverage comparing the image from June to the ones taken in July. This differences can be easily explained by the growing season. We can further see inhomogeneity within the satellite-like area at the 30/07/2018 and the other days. Even the neighbouring field strips show different colours.

The relative differences in surface reflectance between average over 300x300 m^2 and over 4.5x4.5 - 40.5x40.5 m^2 for the 19/07/2018, 30/07/2018 and 31/07/2018 at the selected position are shown in Figure 4.6. The colours indicate the different reference areas with the same colour code as in Figure 4.3. The different days are shown with different line styles.

Comparing a single pixel to the satellite-like pixel average, the relative differences vary among the days. Even with only one day between the measurements, the difference is large for the smallest ground area. We do not assume that those differences originate from strong change in vegetation. Instead, slight shift in flight lines and thus, slightly different reference area could be the reason for them. Such shifts will not occur for a real, fixed ground station. For the larger reference areas, the relative differences are very similar across the different area sizes. We observe only little changes between the 30th and 31st July. The difference between reference area and satellite pixel on the 19/07/2018 is larger than on the other days especially around 500 and 680 nm. Thus, the determined uncertainty is not applicable to measurements taken with a time lag of two weeks.
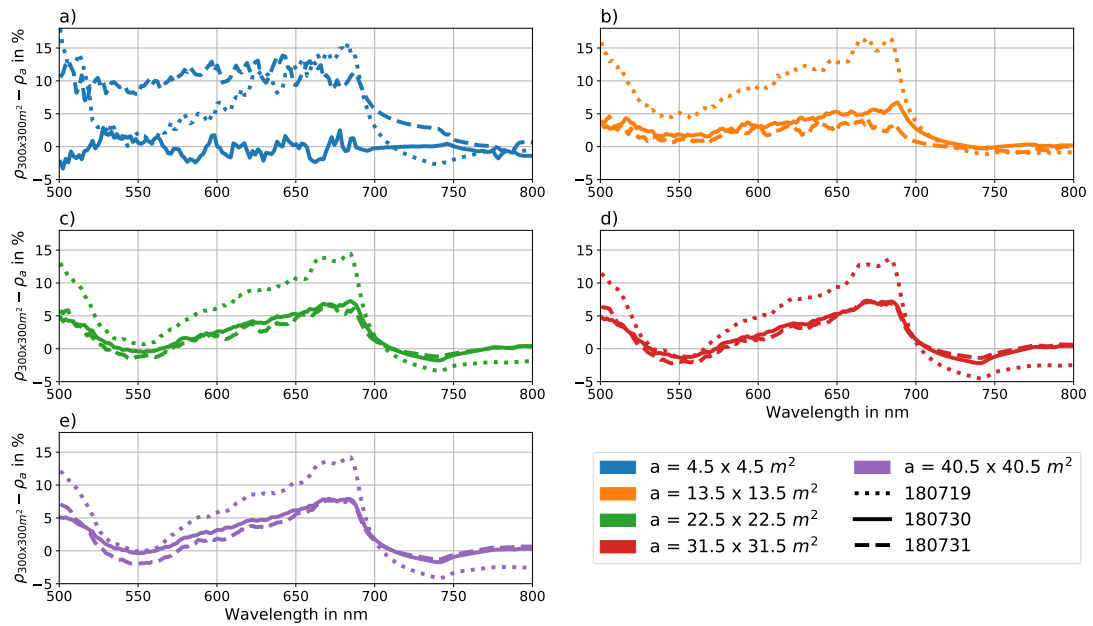
Figure 4.6   Relative difference between surface reflectance average over 300x300 m^2 and a) 4.5x4.5 m^2, b) 13.5x13.5 m^2, c) 22.5x22.5 m^2, d) 31.5x31.5 m^2 and e) 40.5x40.5 m^2 measured from HyPlant at 42.81706^o N, 11.062584^o E on 19/07/2018, 30/07/2018 and 31/07/2018.

4.4.5 Influence of surface reflectance uncertainty on TOA radiance

The surface reflectance from satellite measurements is retrieved from level 1 radiance data which have a certain measurement uncertainty. We want to evaluate the influence of the differences in surface reflectance due to difference in spatial resolution on the TOA radiance. If the effect is smaller than the measurement uncertainty, it cannot be disentangled. A forward model based on radiative transfer simulations (Section 4.3.2) can be used to simulate the TOA radiance based on the measured surface reflectance. Further necessary parameters are atmospheric parameters (aerosol properties (continental aerosol, AOT=0.05), surface pressure (1013 hPa)), and the observation geometries (azimuth angle (AZI)= 162°, viewing zenith angle (VZA)= 31°, and sun zenith angle (SZA)= 46°). The angles are similar to the ones from the simultaneous over-pass of OLCI-FLEX. In this section, we compare the forward simulated TOA radiance with the 300x300m^2 averaged surface reflectance as input against the TOA radiance based on the surface reflectance from the different ground site reference areas.

The relative differences in surface reflectance and in TOA radiance are shown in Figure 4.7. The blue filling in the background indicates the standard deviation of all areas considered in the geolocation mismatch study comparing shifted satellite pixels to the 4.5x4.5 m^2 area (Section 4.4.3). The black horizontal line in the TOA radiance subplot gives the goal of FLEX's absolute calibration uncertainty of 2 % [Drusch, 2018].

The TOA radiances at wavelengths smaller than 620 nm are less sensitive to the surface reflectance. Differences in the surface reflectance due to difference in the spatial resolution of up to 6 % translate in TOA radiance differences smaller than 2 %. At about 620 nm, this differ-
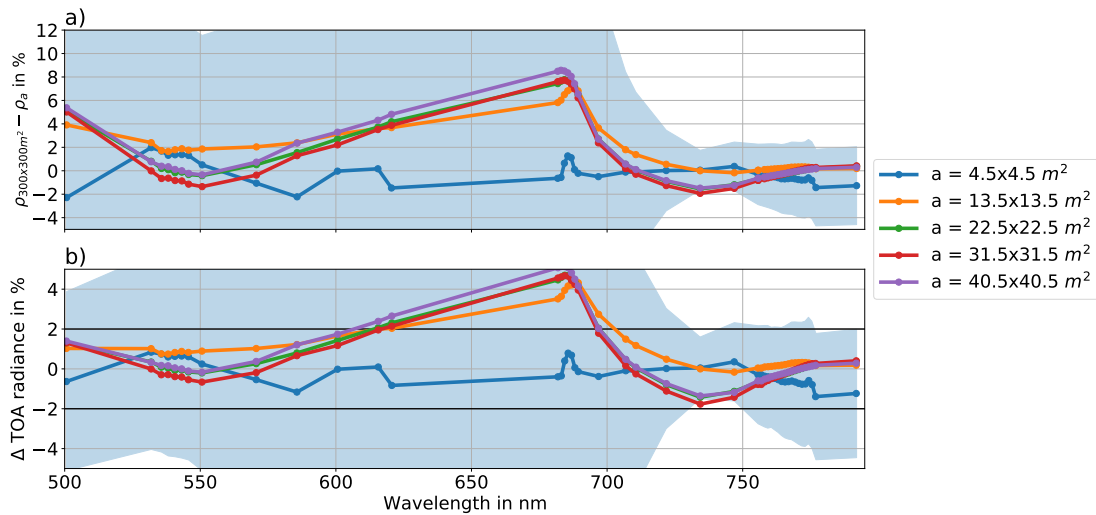
Figure 4.7 a) Relative difference between surface reflectance average over 300x300 m^2 and areas between 4.5x4.5 and 40.5x40.5 m^2 measured from HyPlant at 42.81706^o N, 11.062584^o E on 30/07/2018 convolved with OLCI-FLEX spectral response functions. The shaded blue area shows the standard deviation of differences between 300x300 m^2 and 4.5x4.5 m^2 areas considering all shifted areas. b) Relative difference for modelled TOA radiance according to the surface reflectances in top. Black lines show aimed uncertainty of FLEX and OLCI TOA radiance as given in the respective mission requirement document [Drusch, 2018, Drinkwater and Rebhan, 2007].

ence in surface reflectance is approximately 4 % and the resulting difference in TOA radiance is slightly larger than 2 %. Overall, the difference in TOA radiance is smaller than 2 % across the spectrum considering all different reference areas. Only between 620 and 700 nm, the difference is larger considering reference areas of 13.5x13.5 m^2 or larger. Here, the relative difference in surface reach up to 8.5 % and the resulting difference in TOA radiance is about 5 %.

The standard deviation due to geolocation mismatch is large for wavelengths smaller than 720 nm. Hence, also the difference in TOA radiance is large. At larger wavelengths, the influence of geolocation mismatch is almost within the uncertainty margin.

4.5 Discussion

We defined three requirements to select a ground site for validation (see 4.3.3) and applied those to HyPlant data. One flight line over central Italy was analyzed and about 50 pixel fulfilled those requirements (see Figure 4.2). All of those pixels are located in the centre of the same agricultural field. We chose the pixel with smallest difference between a ground-based like measurement of the surface reflectance and the satellite-like surface reflectance. This position is treated as possible ground site for surface reflectance validation of satellite data. Furthermore, we analyzed the following effects that impair the validation of surface reflectance at the chosen ground site:

1. Effect of the size of the ground observation area

2. Effect the geolocation mismatch between the ground site position and the satellite pixel centre

3. Temporal stability of the representativeness of the ground site

4. Effect of 1. and 2. on the TOA radiance

The smallest area shows the smallest difference between ground-based and satellite-based surface reflectance which is clear as this is the reason why we chose this position. The larger reference areas show difference of up to 8% between 500 and 700 nm which is left of the red edge. At the right of red edge, the areas between 13.5x13.5 m^2 and 40.5x40.5 m^2 have small difference in surface reflectance compared to the satellite-like observation with a maximum value of -2% (see Figure 4.3). This difference in surface reflectance across the observation areas hints to spatial inhomogeneity in the surface reflectance around the chosen site. However, the relative variability in surface reflectance of a vegetated surface is more pronounced left of the red edge in our studied case.

A similar pattern in the difference between ground-based and satellite-based surface reflectance is observed by studying the effect of the geolocation mismatch. Here, the difference between spatially shifted satellite observation with respect to the defined ground-based observation is large with values of more than 80% left of the red edge. Right of the red edge, the difference is less than -10%. Our study is limited to distances between the ground site and the satellite pixel centre of up to 205 m. Furthermore, only pixels which are aligned in a grid parallel to the ground-based reference area borders are studied. However, the differences due to those geolocation mismatches are already too high to allow a meaningful surface reflectance validation. In future studies, the requirement for spatial representativeness should be adjusted to an area of about 1x1 km^2. With such a large homogeneous area, the uncertainty due to geolocation mismatch can be reduced. However, the studied area did not have any homogeneous field of this size.

We examined the temporal evolution of the validation uncertainty due to difference in spatial resolution within two weeks. Already within this short time period, the difference in ground-based and satellite-based surface reflectance varies strongly. Only at wavelengths between 720 and 800 nm, those differences are temporally more stable and smaller than 5%. Especially the reference area of 13.5x13.5 m^2 shows differences of less than 1% within this spectral range for all examined days (see Figure 4.6). The results of the temporal evolution study for the smallest reference area cannot directly be translated to a real ground-based measurement. The chosen pixels of the different overflights varied slightly in the position and thus, the representativeness also varies not only due to the temporal changes but also due to the different spatial pointing. Nevertheless, this study showed that the temporal evolution of the uncertainty due to difference in spatial resolution must be monitored frequently e.g. using airborne measurements.

The effect of the difference in surface reflectance due to spatial resolution on the TOA radiance is examined in the last part of this study. Regardless of the reference area, the difference in TOA

radiance due to the difference in ground-based and satellite-based surface reflectance measurement is smaller than 2%. Only within the oxygen absorption band at 680 nm, the differences are up to 5%. The goal for the absolute radiometric uncertainty of FLORIS is 2% [Drusch, 2018]. Hence, the difference in TOA radiance due to the difference in spatial resolution cannot be disentangled from the radiance uncertainty of FLORIS at the wavelengths larger than 700 nm.

Gao et al. [2023] presented a similar study. They quantified the uncertainty due to different spatial resolutions in the same way as shown in this study. However, Gao et al. [2023] only showed the mean uncertainty over the wavelength for point measurements of 2x2 m^2 and satellite-like areas of 30x30 m^2. They showed a mean uncertainty of up to 5% and 1.7% averaged over different study cases. This uncertainty increases with decreasing the point measurement area and decreases by choosing more sampling points. Our selected ground-site has a validation uncertainty due to spatial heterogeneity averaged over the wavelength of 0.3% for a ground observation area of 4.5x4.5m^2. For the other reference ground-based areas, the uncertainty ranges from 1.7 to 2.5 % without a dependence on the sample area size. The results from Gao et al. [2023] cannot be applied to FLEX validation as FLORIS's spatial resolution is coarser and thus, the uncertainties are larger. Furthermore, Gao et al. [2023] did neither study the geolocation mismatch nor the temporal evolution of the uncertainty.

Wu et al. [2023] quantified the uncertainty of a multi-scale validation of surface reflectance. The multi-scale validation is based on a map which is used to upscale a ground-based point measurement to the larger spatial scale of the satellite pixel. They identified two main uncertainty sources namely, uncertainties of the upscaling map and uncertainties due to geolocation mismatch. When the uncertainty due to difference in spatial resolution is known, the ground-based measurement can be used to evaluate the satellite-based measurement. The uncertainty due to geolocation mismatch at the study site used by Wu et al. [2023] was between -10 and 25% which is smaller than the uncertainty we found. The difference in the results is due to the difference in surface type composition.

Our study is limited to the study area and the study time. Our study area covered only small homogeneous fields. Hence, the validation uncertainty due to geolocation mismatch at the identified ground-site is too large for validation purposes. The method presented here should be applied to a location with larger homogeneous fields. The requirements for identifying the best location for the ground site should be tightened to an area of more than 1x1 km^2. Furthermore, the temporal evolution of the validation uncertainty must be monitored regularly. The determined validation uncertainty is only valid if both airborne measurements and satellite measurements have the same observation geometry. Otherwise, the angular dependence of the surface reflectance could increase the validation uncertainty.

4.6 Conclusion

Both Buman et al. [2022] and Rossini et al. [2022] stated that a validation strategy for FLEX is important for the success of the mission but that it is not yet defined. Du et al. [2023] applied a

validation of fluorescence products with measurements from a tower. They identified unsolved issues due to difference in spatial resolution. Furthermore, Buman et al. [2022] identified the need of a homogeneous area that can be used as ground validation site. We showed in our study a possible strategy to identify such ground validation site. By quantifying the uncertainty due to heterogeneity and geolocation mismatch with airborne measurements of the surface reflectance, we enable a validation by the comparison between ground-based and satellite-based measurements with spatial resolution of 300x300 m^2. We applied this method to an example flight line and identified a possible ground site within this overpass. However, the heterogeneity of the surface within the studied flight line results in very high relative uncertainties for the spectral ranges between 500 and 720 nm. With this large uncertainties, neither a validation of the surface reflectance nor the underlying radiance measurement is meaningful. At wavelengths between 720 and 800 nm, the uncertainty of the surface reflectance is small, temporally consistent within two weeks, and the uncertainty due to geolocation mismatch is small too. The according uncertainties of the TOA radiance are also within the measurement uncertainty of the instrument. Thus, uncertainties due to the heterogeneity cannot be disentangled. Nevertheless, those uncertainties must be monitored frequently by airborne or unmanned automatic vehicle based missions. For a better temporal and spectral consistency, the choice of the validation site must underlie even more strict constraints. To minimize the uncertainty due to geolocation mismatch, the criteria for selecting a ground site should be fulfilled by an area of about 1x1 km^2.

5

Aerosol layer height from OLCI's O_2A bands

Authors Lena Katharina Jänicke[1], Rene Preusker[1], Nicole Docter[1] and Jürgen Fischer[1]

[1]Institute of Meteorology, Freie Universität Berlin (FUB), Carl-Heinrich-Becker-Weg 6-10, 12165 Berlin, Germany

5.1 Abstract

The aerosol layer height (ALH) is an important parameter that characterizes aerosol interaction with the environment. An estimation of the vertical distribution of aerosol is necessary for studies of those interactions, their effect on radiance and for aerosol transport models. ALH can be retrieved from satellite-based radiance measurements within the oxygen absorption band between 760 and 770 nm (O_2A band). The oxygen absorption is reduced when light is scattered by an elevated aerosol layer. The Ocean and Land Colour Imager (OLCI) has three bands within the oxygen absorption band. We show a congruent sensitivity study with respect to ALH for dust and smoke cases over oceans. Furthermore, we developed a retrieval of the ALH for those cases and an uncertainty estimation by applying linear uncertainty propagation and a bootstrap method. The sensitivity study and the uncertainty estimation are based on radiative transfer simulations. The impact of ALH, aerosol optical thickness (AOT), the surface roughness (wind speed) and the central wavelength on the top of atmosphere (TOA) radiance is discussed. The OLCI bands are sufficiently sensitive to ALH for cases with AOTs larger than 0.5 under the assumption of a known aerosol type. With an accurate spectral characterization of the OLCI O_2A bands better than 0.1 nm, ALH can be retrieved with an uncertainty of a few hundred meters. The retrieval of ALH was applied successfully on an OLCI dust and smoke scene. The found ALH is similar to parallel measurements by the Tropospheric Monitoring Instrument (TROPOMI). OLCI's high spatial resolution and coverage allow a detailed overview of the vertical aerosol distribution over oceans.

5.2 Introduction

Aerosol is a mixture of particulate matter in the atmosphere with natural or anthropogenic origin. Depending on its origin, aerosol can be distributed differently within the atmosphere. For example, industrial aerosol is rather found within the boundary layer, soil from a dust outbreak of a desert can be transported up to the free troposphere, smoke plumes from large biomass burning events can reach the upper troposphere and volcanic ash eruptions can transport the ash up to the stratosphere [Xu et al., 2018]. The main aerosol sources are on the earth's surface, and aerosol is uplifted under certain weather conditions. Thus, 70% of all aerosol particles are located in the boundary layer [Xu et al., 2018]. In contrast, dust and smoke are regularly uplifted.

The vertical distribution of aerosol is a key parameter in climate modelling and remote sensing. It is necessary for the calculation of the earth's energy budget by estimating the direct and indirect radiative forcing of aerosol [Kylling et al., 2018, Kipling et al., 2016, Pachauri et al., 2014]. Aerosol is, in addition to the greenhouse gases, the most important anthropogenic climate forcer. It has both cooling and warming effects. However, uncertainties about aerosol composition and distribution induce uncertainties in the prediction of the climate [Colosimo et al., 2016]. Large uncertainties in magnitude and sign of radiative effect originate from unknown or imprecise aerosol layer height (ALH) [Kipling et al., 2016, Pachauri et al., 2014]. An example of the impact of aerosol on the earth's environment is the current warming of the Atlantic Ocean

[Copernicus, 2023b]. We can observe a decrease in Saharan dust emissions and an increase in the temperature of the Atlantic. Saharan dust is transported westward across the Atlantic Ocean. It is assumed that those dust layers in the atmosphere above the ocean had a cooling effect, as light was reflected back to space and not absorbed by the water. A valid characterization of ALH is also important for the retrieval of numerous parameters from remote sensing data. The uncertainty of CO_2 [Houweling et al., 2005, Guerlet et al., 2013] and NO_2 [Chimot et al., 2019] retrieval can be reduced by including the aerosol vertical distribution. Furthermore, aerosol parameter retrievals themselves can be improved with a better knowledge of ALH, e.g., the aerosol retrievals of aerosol optical thickness (AOT) and the single scattering albedo (SSA) from the ultra violet spectral range [Torres et al., 2013]. In particular, the retrieval of AOT is sensitive to the aerosol height over dark surfaces [Li et al., 2020]. Eventually, with a constrained aerosol profile, the atmospheric correction is more accurate, which is important for land and ocean applications, e.g., surface retrievals like the fluorescence [Frankenberg et al., 2011] or ocean colour experiments [Duforêt et al., 2007].

The aerosol vertical distribution can be derived on a global scale with remote sensing. Active instruments like the Cloud-Aerosol Lidar with Orthogonal Polarization (CALIOP) mounted on Cloud-Aerosol Lidar and Infrared Pathfinder Satellite Observations (CALIPSO) [Winker et al., 2009] have a high accuracy of the retrieval of the aerosol height, but due to their small foot print, the global coverage is low [Xu et al., 2018]. In contrast, passive remote sensing instruments do have good global coverage but often a small sensitivity to aerosol height. However, there have been several sensitivity studies (e.g., [Kokhanovsky and Rozanov, 2010, Hollstein and Fischer, 2014, Colosimo et al., 2016]) and attempts to retrieve aerosol height, e.g., from the O_2A absorption band (760-770 nm) or the O_2-O_2 bands (470 nm). As part of a sensitivity study, Colosimo et al. [2016] investigated the possibility to retrieve aerosol profiles from O_2 absorption bands with high spectral resolution. They showed that with very high spectral resolution, up to two parameters of the aerosol extinction profile can be retrieved for measurements with a resolution of 0.003 nm. Hollstein and Fischer [2014] developed an ALH retrieval for high spectral resolution O_2 measurements with resolutions of 0.3 nm, as it is planned for the Fluorescence Explorer. Dubuisson et al. [2009] estimated the uncertainty of an ALH retrieval from MERIS oxygen absorption bands. Preusker and Lindstrot [2009] performed a sensitivity study about gaining information about the cloud top pressure from the O_2 absorption from MERIS. They also showed that the retrieval of vertical information from the O_2 band is possible even with low spectral resolution. Spectral high resolution instruments like the Scanning Imaging Absorption Spectrometer for Atmospheric Chartography (SCIMACHY) [Kokhanovsky and Rozanov, 2010, Sanghavi et al., 2012], Global Ozone Monitoring Experiment-2 (GOME-2) [Nanda et al., 2018], Orbiting Carbon Observatory 2 (OCO-2) [Zeng et al., 2020] and Tropospheric Monitoring Instrument (TROPOMI) [Nanda et al., 2019] have been used successfully for the retrieval of the aerosol height. Also, spectrally coarse top-of-atmosphere (TOA) radiance measurements hold information about the aerosol height as it is shown for ALH retrievals from the Medium Resolution Imaging Spectrometer (MERIS) and PoLarization and Directionality of the earth's Reflectances (POLDER) [Dubuisson et al., 2009]. Expected in 2024, the Ocean Colour Instru-

ment (OCI) will be launched on the National Aeronautics and Space Administration's (NASA's) Plankton, Aerosol, Cloud, Ocean Ecosystem (PACE) spacecraft combining the settings of its precursors Visible Infrared Imaging Radiometer Suite (VIIRS) and ozone monitoring instrument (OMI). OCI will have hyperspectral bands within the oxygen absorption bands (O_2A, O_2B (680 nm)) and within the ultra violet band with a spectral resolution of 5 nm and a spectral sampling of 2.5 nm [Werdell et al., 2019]. With this band combination, the OCI shall retrieve the aerosol height for aerosol layers with an AOT larger than 0.1 with an uncertainty of 0.15 km over dark surfaces [Remer et al., 2019]. The retrieval will be based on the differential optical absorption spectroscopy ratio (DOAS) using an absorbing and a non-absorbing band. A similar method is the spectral fitting method of O_2A and/or O_2B bands as it is applied on measurements of the Earth Polychromatic Imaging Camera (EPIC) sensor on the Deep Space Climate Observatory (DSCOVR) satellite [Xu et al., 2019]. The aerosol height retrieval of TROPOMI is also based on spectral fitting but with radiance simulations performed by a neural network algorithm [Nanda et al., 2019]. The third common method is the use of the O_2-O_2 band at 477 nm as presented by Chimot et al. [2017].

The existing passive remote sensing retrievals of the aerosol height have a rather coarse horizontal spatial resolution but a high spectral resolution (e.g., SCIAMACHY: 0.48 nm, GOME-2: 0.48 nm ,TROPOMI: 0.55 nm). The Ocean and Land Colour Imager (OLCI) on Sentinel-3 satellites has a spatial resolution of about $300 \times 300 \ m^2$ [Donlon et al., 2012]. OLCI has three spectral bands within the oxygen absorption band with spectral resolution of 2.5–3.75 nm [Donlon et al., 2012]. So far, those bands have not been used to derive the aerosol height. The Sentinel-3 series can be used to collect climate data over a long temporal range [Donlon et al., 2012]. The large fleet of Sentinel-3 (currently Sentinel-3A and Sentinel-3B) allows a global coverage of 2 to 3 days even without including sun glint pixels. As mentioned above, especially for trace gas-retrievals and ocean colour algorithms, the aerosol height is an important parameter. By retrieving ALH directly with OLCI, the information could be used to enhance its atmospheric correction and to provide new insight in aerosol–cloud interactions on a small spatial scale. With an ALH product from OLCI, no ALH products from other instruments are necessary, and thus, a spatial overlap of those instruments does not need to be considered.

We use OLCI's radiance measurements in the O_2 absorption band to distinguish low, medium and high aerosol over oceans. We show a sensitivity study on the retrieval of ALH from OLCI O_2A bands, a proof of concept for retrieving ALH over oceans and an uncertainty estimate for the ALH retrieved from OLCI. Due to the steep and distinct oxygen absorption lines, an exact spectral characterization of the O_2A bands is necessary. For the best possible characterization, we use the temporal evolution model of the spectral characterization of OLCI. With this characterization, we can show that OLCI's radiance measurements are sensitive to aerosol height. This is also shown in the application of an aerosol height retrieval on two case studies. For this study, the retrieval is limited to dust and smoke particles in cloud-free scenes over the ocean. It is based on radiative transfer simulations. The radiative transfer model, input data and the retrieval algorithm are described in the methods Section 5.3. The results of the sensitivity study and the application of the retrieval on the test scenes are presented in Section 5.4. The uncertainty of the

retrieval is presented in Section 5.5. The results are discussed in Section 5.6.

5.3 Methods

5.3.1 Radiative transfer model

Sensitivity studies and the look-up tables (LUTs) applied in the retrieval of ALH are based on radiative transfer simulations calculated with the vector radiative transfer model, the "matrix operator model" (MOMO), developed at the Freie Universität Berlin [Hollstein and Fischer, 2012, Fell and Fischer, 2001]. The interaction of the light that travels through the atmosphere is described with the radiative transfer equation. Its matrix form is discretized, Fourier-decomposed, and solved by a doubling and adding method [Hollstein and Fischer, 2012]. The output of MOMO is the diffuse upward and downward-directed radiance for discrete angles for each atmospheric layer.

The atmosphere is approximated with a model of plane parallel layers with homogeneously distributed particles. The ocean surface is approximated as randomly distributed planes with Fresnel properties. The distribution of the surface normals depends on the wind speed. This dependency is described by Cox and Munk [1954]. The ocean interface is described with a refractive index of 1.335 (water temperature: 20 °C; salinity: 36 PSU)with no further description of the water constituents as the studied bands are not influenced by them.

The gas absorption is described by a line-by-line model which is approximated with a k-binning solution [Doppler et al., 2014b]. The input of the line-by-line model is taken from the HITRAN16 data base [Gordon et al., 2017]. The oxygen cross sections originate from Drouin et al. [2017].

5.3.2 Setup of radiative transfer simulations

We study the sensitivity of the O_2A absorption bands of OLCI with main focus on the aerosol height. However, the bands are also sensitive to AOT, aerosol type, the surface roughness, viewing geometry and band characterization. To quantify the sensitivities, we simulate TOA radiances for various quantities of those parameters.

The basic setup describing the ocean and the atmosphere is kept constant. The atmosphere are split in 27 layers. The lower 6 km is split into layers every 25 hPa. We chose the standard Air Force Geophysical Laboratory (AFGL) Atmospheric Constituent Profile [Anderson et al., 1986] for the mid-latitude summer case with a surface pressure of 1025 hPa.

To reduce the number of simulations, the TOA radiance is calculated for four rectangular spectral response functions at 754 nm with a width of 23.5 nm; at 762 nm with a width of 10.4 nm; at 765 nm with a width of 12.9 nm; and at 768 nm with a width of 10.2 nm. From those simulations, we create look-up tables by convolving the simulations with OLCI's spectral instrument response functions.

The ocean roughness is tuned for wind speeds between 3 and 9 m/s. All simulations are made
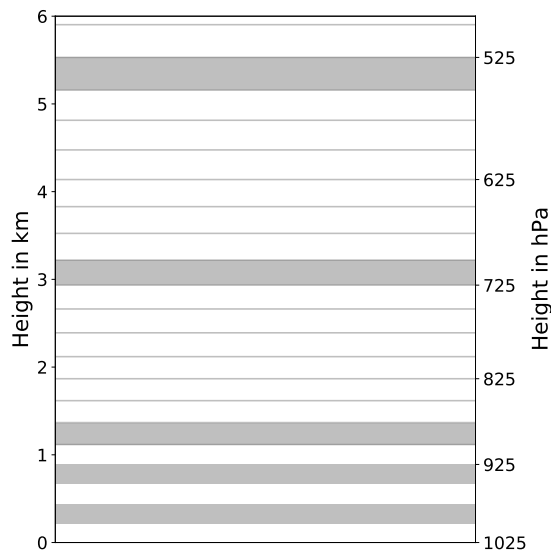
Figure 5.1   Schematic overview of aerosol vertical distributions for five cases with ALH at 327, 777, 1244, 3076 and 5255 m. The lines indicate the layer interfaces.

for different observation and sun angles covering the whole hemisphere. The aerosol is placed in one of the following layers with borders at: 1000 hPa (215 m) and 975 hPa (440 m); 950 hPa (665 m) and 925 hPa (890 m); 900 hPa (1117 m) and 875 hPa (1367 m); 725 hPa (2934 m) and 700 hPa (3219 m); 550 hPa (5157 m) and 525 hPa (5530 m). In all other layers but the one where the aerosol is placed, we assume that no aerosol is present. We define the aerosol layer height (ALH) as

$$ALH = \frac{a+b}{2} \tag{5.1}$$

with a as the lower layer boundary and b as the upper layer boundary. The ALHs of the 5 cases are 327, 777, 1244, 3076 and 5255 m (see Figure 5.1). We chose two different aerosol models, namely *dust* and *strong absorbing fine mode aerosol* (SABS), which are described in the next section (Section 5.3.3). AOT at 550 nm ranges from 0.05 up to 12 for dust and up to 5.5 for SABS.

5.3.3 Aerosol model

Elevated aerosol particles originate mostly from uplifted desert dust or smoke from biomass burning. We use models that describe those two aerosol types. The spheroid model of Dubovik et al. [2006] is used to parameterize dust particles. The model is based on LUTs with simulated size-dependent and shape-dependent optical properties for random oriented particles. The complex shape of dust particles is approximated by spheroids. The microphysical properties were chosen following the hybrid end-to-end aerosol classification model for EarthCARE (HETEAC) [Wandinger et al., 2023]. For Saharan desert dust, the refractive index at 550 nm is chosen to be $1.53 + i0.003$, the effective radius is 1.94 µm, the mode radius of the volume size distribution 2.32 µm and logarithmic mode width of 0.6.
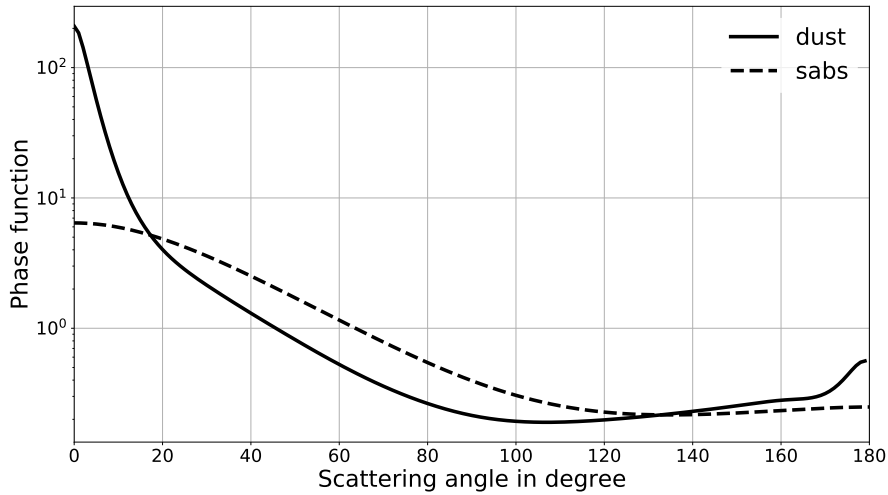
Figure 5.2 Phase function of aerosol models *dust* in solid lines and *strong absorbing aerosol* (SABS) in dashed lines at 760 nm.

Biomass burning aerosol is approximated by strong absorbing spherical fine-mode particles following HETEAC and the Aerosol-CCI approach [Wandinger et al., 2023]. This approximation is true especially for fresh smoke particles which have a large fraction of strong absorbing soot and other absorbing material. We chose a particle distribution with an effective radius of 0.14 µm and a spectrally constant refractive index of $1.5 - 0.043i$.

The phase functions are shown in Figure 5.2 for different scattering angles and depend on the sun zenith angle (SZA) ϕ_{SZA}, the viewing zenith angle (VZA) ϕ_{VZA} and the azimuth difference angle (AZI) θ_{AZI}. It is calculated with the following formula (adapted from [Liou, 2002]):

$$cos(\Theta_{scat}) = sin(\phi_{SZA}) \cdot sin(\phi_{VZA}) \cdot cos(\theta_{AZI}) - cos(\phi_{SZA}) \cdot cos(\phi_{VZA}) \tag{5.2}$$

The phase function for the spherical SABS particles is calculated with a Mie scattering algorithm [Wiscombe, 1980]. Further optical properties are shown for dust and SABS in Table 5.3.

5.3.4 OLCI data

OLCI has three bands within the O_2A absorption band, namely Oa13, Oa14 and Oa15, with nominal central wavelengths of 761.25 nm, 764.375 nm and 767.5 nm and nominal full width at half maximums (FWHM) of 2.5 nm, 3.75 nm and 2.5 nm. As a reference band without absorption, we chose the Oa12 band at 753.75 nm with nominal FWHM of 7.5 nm. The relative response functions of those four bands are shown together with the TOA transmission by oxygen in Figure 5.3. The input of the retrieval is the Level 1 (L1) data, including the radiances at the named bands, the solar flux, the wind speed and the observation and sun geometry. From the given sun and observation azimuth angle, we calculate an azimuth difference angle with 0° pointing towards the sun, marking the sun glint area, and 180° in the backscattering direction.
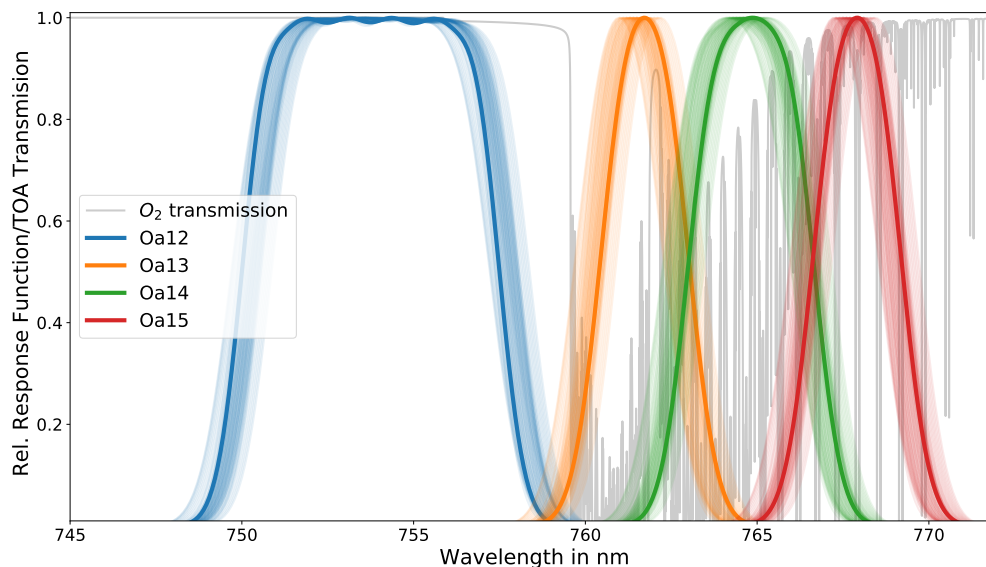
Figure 5.3   Relative spectral response functions (RSR) of OLCI-B in O_2 absorption band. Transparent colours show RSR of different detectors and non-transparent colours are the harmonized response functions. In grey, the TOA transmission is given for an air mass factor of 2.2.

Preprocessing

OLCI is built of 5 cameras with 740 across track pixels each. Each of those pixels has its own spectral response function (see Figure 5.3). In particular, for the absorption bands, it is crucial to know them as accurately as possible. Due to the deep O_2 absorption lines, only small shifts in the central wavelength result in large differences in the TOA radiance [Preusker and Lindstrot, 2009]. For the accurate choice of spectral response function, we use the model that characterizes the time evolution of OLCI's spectral responses (see [Preusker, 2021] `https://sentinels.copernicus.eu/documents/247904/2700436/LUT.zip`, accessed on 24 February 2023). Based on this band characterization and on the Sentinel Application Platform (SNAP) plugin for the O_2 harmonization of OLCI [Preusker, 2020], the data are harmonized to the nominal spectral response function for each band (Oa13, Oa14, Oa15). The harmonization is based on precalculated LUTs of transmissions [Preusker and Fischer, 2021]. First, the OLCI bands 12–16 are normalized with respect to their corresponding in-band solar irradiance. Secondly, reference window radiances are calculated by a spectral interpolation of the window band Oa12 and Oa16 to the nominal spectral position of the bands Oa13, Oa14 and Oa15. With these interpolated reference window radiances, apparent transmissions are calculated for those bands. The apparent transmission is shifted to the nominal wavelength using a combination of KD-search and an inverse distance weighted interpolation [Preusker and Fischer, 2021]. The harmonization method is described in more details in Appendix 5.7.2.

The harmonized transmissions have the same spectral response function across track, and thus, the LUTs for the ALH retrieval do not need to account for the central wavelength or FWHM. For the sensitivity study, we introduce the central wavelength as dimension of the LUT. The out-
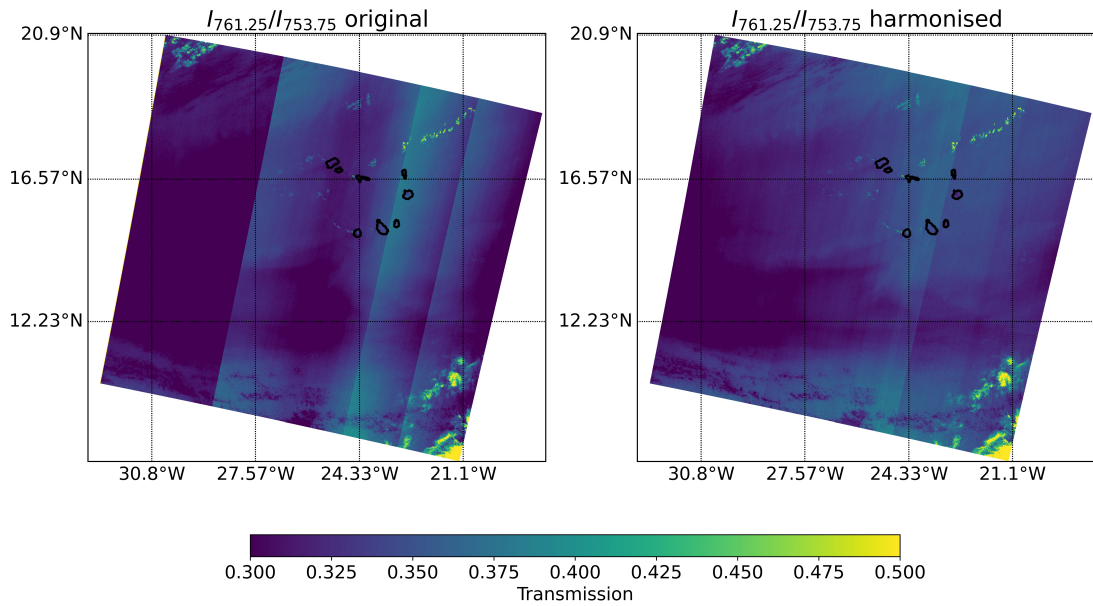
Figure 5.4 Comparison of original transmission on the **left**, calculated as ratio of OLCI-B L1 radiance at 761.25 and 753.75 nm, and harmonized transmission on the **right**.

put of the simulations is convolved with the time-evolved spectral response function, which is shown as non-transparent coloured lines in Figure 5.3. For the sensitivity study LUT, the response functions are shifted plus and minus 0.1 nm. In addition to the transmissions at the absorption bands, the radiance of the absorption-free band is used for the retrieval and the sensitivity study.

In Figure 5.4, the transmission for the band ratio at 761.25 and 753.75 nm is shown before and after the harmonization of the central wavelength. Before the harmonization, the interface between the cameras is clearly visible. The mean difference between camera 3 and 4 along the track is on average 6 % with occasional 10% peaks. The harmonized transmission shows only slight camera effects, especially between camera 3 and 4. Here, the peak differences could be eliminated and the mean difference is reduced by 1.5 %. The residual difference is set as measurement uncertainty for the band at 761.25 nm (see Section 5.3.6).

Case study and reference data

The retrieval algorithm is applied for two case study scenes: (i) during the large dust storm in summer 2020 called "Godzilla" (see e.g., [Yu et al., 2021]) and (ii) during a large wild fire at the coast of California in September 2020. Both scenes were selected to match our assumed surface pressure of 1025 hPa.

For the dust scene, we chose two sequences of Sentinel-3B on 18 June 2020 over Cape Verde at 11:35 UTC and 11:38 UTC. The scene is dominated by a large dust plume with a large range of different optical thicknesses and only very few clouds. The two sequences have a mean surface pressure according to the L1 OLCI data of 1015 and 1021 hPa.

For the smoke scene, we chose sequences of Sentinel-3A and Sentinel-3B on 8 September 2020 taken between 18:25 and 18:30 UTC. In the centre of the scene is a very thick smoke plume with clouds in the northeast and southwest. The sequences have a mean surface pressure according to the L1 OLCI data of 1011, 1024 and 1025 hPa.

As reference data set, we use the ALH product (S5P_L2__AER_LH version 1 product (`https://doi.org/10.5270/S5P-j7aj4gr`, accessed on 28 March 2023)) from TROPOMI on board of Sentinel-5P (S5P) from the overpasses on the same days about two to four hours after the Sentinel overpass: on 18 June 2020 at 14:13, 14:18 and 15:53 UTC and on 08/09/2020 between 20:24 and 20:29 UTC. TROPOMI has a spectral resolution within the O_2A band of 0.38 nm with a spectral sampling interval of 0.12 nm and a spatial resolution of 7 km $\times$ 3.5 km [Veefkind et al., 2012]. The retrieval is based on a neutral network approach [Nanda et al., 2019].

Furthermore, we compare our results with CALIOP measurements on board of CALIPSO. The active instrument provides the extinction profile at 532 nm with a vertical resolution of 60 m and a horizontal resolution of 5 km. The effective aerosol height can be approximated from the extinction profile by the weighted extinction or the cumulative extinction. Both definitions have been used for the comparison with passive remote sensing [Kylling et al., 2018, Nanda et al., 2020, Koffi et al., 2012]. We use the weighted extinction, which is defined as

$$ALH_{Cali} = \frac{\sum\limits_{i=1}^{n} \beta_{ext,i} * Z_i}{\sum\limits_{i=1}^{n} \beta_{ext,i}}, \tag{5.3}$$

with $\beta_{ext,i}$ as the aerosol extinction (km^{-1}) at 532 nm at altitude Z_i in km and n number LIDAR product layers.

We calculate the weighted extinction from the level 2 Aerosol Profile product (`https://doi.org/10.5067/CALIOP/CALIPSO/CAL_LID_L2_05kmAPro-Standard-V4-21`, accessed on 9 March 2023). For the dust case, we chose the overpass from 18 June 2020 between 03:22 and 03:45 in the morning, which was about eight hours earlier than the Sentinel overpass. For the smoke case, we chose the overpass from 8 September 2020 between 21:45 and 22:07 UTC, which was about three hours after the Sentinel overpass.

5.3.5 1D variational approach

The retrieval of ALH is based on a 1D variational approach (1Dvar). For given a surface and atmosphere description and a measurement geometry, the ALH and the AOT are optimized in order to reduce the difference between measured L1 radiances and forward-modelled radiances. Forward-modelled radiances are calculated by interpolating within the above described LUTs. Following the direction of the largest gradient, ALH and AOT are changed step-wise in an iterative process taking an a priori knowledge, with its uncertainty and the measurement uncertainty into account. The following description of the 1Dvar method and all formulas are adapted from Rodgers [2000].

The state vector is one input of the forward model. It includes the ALH and the AOT in our case. Further, fixed parameters P_a, namely the wind speed and the measurement geometry, are the input of the forward model. The state vector X_i is adjusted in each step i using the Gauss–Newton method considering the gradient in terms of the Jacobian $\mathbf{K_i}$ and the measurement error covariance $\mathbf{S_e}$:

$$
\begin{aligned}
X_{i+1} = X_i &- (\mathbf{S_a}^{-1} + \mathbf{K_i}^T \mathbf{S_e}^{-1} \mathbf{K_i})^{-1} (\mathbf{K_i}^T \mathbf{S_e}^{-1} \cdot (F(X_i, P_a) - Y) \\
&- \mathbf{S_a}^{-1} \cdot (X_a - X_i))
\end{aligned}
\tag{5.4}
$$

The difference between forward model $F(X_i, P_a)$ and measurement Y is weighted with the measurement error covariance matrix and the Jacobian. Furthermore, the difference between state vector and a priori knowledge $\mathbf{X_a}$ weighted by the a priori error covariance matrix $\mathbf{S_a}$ is taken into account.

Once the maximum number of iterations (10) is reached or the increment weighted by retrieval error covariance matrix $\hat{\mathbf{S}}$ is small, the iteration stops. The second stop criterion is given by

$$
(X_i - X_{i+1})^T \cdot \hat{\mathbf{S}}_\mathbf{i}^{-1} \cdot (X_i - X_{i+1}) < n \cdot \varepsilon
\tag{5.5}
$$

with $\varepsilon = 0.01$ and $n = 2$ is the number of parameter state dimensions and the retrieval error covariance matrix:

$$
\hat{\mathbf{S}}_\mathbf{i} = (\mathbf{S_a}^{-1} + \mathbf{K_i}^T \mathbf{S_e}^{-1} \mathbf{K_i})^{-1}.
\tag{5.6}
$$

This method assumes Gaussian probability density functions of uncertainty and bias-free measurements, priors and models.

5.3.6 Retrieval of ALH from OLCI level 1 data

We retrieve the ALH and AOT for cloud-free cases over ocean and for known aerosol types. The input of the retrieval are harmonized, normalized radiances I of the absorption-free band at 753.75 nm and of the absorption bands at i = 761.25, 764.375 and 767.5 nm on a logarithmic scale:

$$
Y_i = log(\frac{I_i}{I_{753.75}}).
\tag{5.7}
$$

The radiances at the different bands are normalized with their corresponding solar irradiances. The measurement errors are approximated with a signal-to-noise ratio of 200 for the absorption-free band and of 50 for all other bands. At band i = 764.375 nm and i = 767.5 nm, the Gaussian error propagation gives

$$
Y_{erri} = \frac{1}{200} + \frac{1}{50}.
\tag{5.8}
$$

To include residual camera effects which are strongest for the band at 761.25 nm (see Figure 5.4), the mean difference between the last detector row of camera 3 and the first detector row of camera 4 is taken as measurement error for this band.

Table 5.1   Input for retrieval of ALH for the dust and smoke test scenes.

Parameter	Values	Data Source
Y	$(I_{753.75}, log(\frac{I_{761.25}}{I_{753.75}}), log(\frac{I_{764.375}}{I_{753.75}}), log(\frac{I_{767.5}}{I_{753.75}}))$	OLCI L1
$S_e[i,i]$	$(\frac{I_{753.75}}{200})^2, (log(T_{Cam4}) - log(T_{Cam3}))^2,$ $(\frac{1}{200})^2 + (\frac{1}{50})^2, (\frac{1}{200})^2 + (\frac{1}{50})^2$	OLCI L1
P_a	wind speed, SZA, VZA, AZI	OLCI L1
$X_{a0,0}$ (AOT)	Dust case: 3.7; Smoke case: 5.5	first guess
$X_{a1,1}$ (ALH)	Dust case: 3000 m; Smoke case: 1000 m	first guess
$S_{a0,0}$ (AOT)	Dust case: $(0.1)^2$; Smoke case: $(0.1)^2$	guess
$S_{a1,1}$ (ALH)	Dust case: $(5000\ m)^2$; Smoke case: $(5000\ m)^2$	guess

All four bands are optimized simultaneously. The a priori input for the ALH and AOT is chosen for each scene (dust: ALH = 3000 m; AOT = 3.7, smoke: ALH = 1000 m; AOT = 5.5) according to other satellite, ground-based and model data. We use AERONET data for the AOT at 550 nm from Cape Verde for the dust scene, which lies in the centre of the large dust plume, and from the AERONET stations at the west coast for the smoke scene which measured AOTs between 5 and 6. The dust ALH is approximated roughly using the back trajectory model Hysplit [Stein et al., 2015] and using the average of the CALIOP data which were recorded about 12 h earlier than the OLCI data. The smoke ALH is approximated roughly using the cloud top height of MODIS [Menzel et al., 2008]. The choice of a priori parameter is restricted to these case studies. A more general assumption could be based on, e.g., Copernicus Atmosphere Monitoring Service (CAMS) data [Peuch et al., 2022]. The a priori error covariance of ALH is kept very large to ensure a free choice of the ALH. In contrast, we chose a small AOT a priori error covariance for robust convergence. The fixed input parameters are the wind speed, SZA, VZA and AZI which are taken from OLCI level 1 data. All inputs for the retrieval are listed in Table 5.1. The surface pressure, central wavelength and the FWHM are also fixed. They are 1025 hPa and the nominal central wavelengths and FWHMs.

5.4 Results

5.4.1 Sensitivity study

The TOA radiance between 760 and 770 nm is mainly determined by the strong absorption features of oxygen. It scales with the surface pressure. However, the surface pressure is a well-known parameter. Consequently, we do not include it in our sensitivity study. Instead, the sensitivity to ALH is studied. The sensitivity study is designed for the OLCI nominal bands

Oa12–Oa15 with their central wavelengths at 753.75, 761.25, 764.375 and 767.5 nm and typical observation and sun geometries with SZA of 30°, VZA at 46° and AZI at 170°. In addition to the surface pressure and the measurement geometry, the surface reflectance, aerosol properties and the characterization of the instrument determine the TOA radiance at those bands. Hence, we study the sensitivity of the TOA radiance with respect to the wind speed, which parameterizes the roughness of the ocean surface and thus, the surface reflectance over the ocean, ALH, AOT, aerosol type, and the central wavelength of the instrument bands. The sensitivity is given as derivative with respect to each of the parameters and each band. To reduce the influence of AOT on the TOA signal, we take the ratio of the absorption bands and the absorption-free band at 753.75 nm. The sensitivity study is performed for different aerosol cases with two different aerosol types, namely dust and SABS, with different AOTs (0.15, 0.55, 1) and different ALHs (1100, 3000 and 4900 m).

Results of the sensitivity study for a glint-free scene are summarized in Figure 5.5. The Jacobians are given in percent. The sensitivity to ALH is given in Figure 5.5a. The absorption-free band is not sensitive to the aerosol height. The band ratio at 761.25 nm shows the largest sensitivity with a change of more than 8% for thick and low dust layers. The sensitivity increases with AOT and decreases with ALH. The more aerosol particles are present in the atmosphere, the more the signal is changed due to scattering and absorption by the aerosol. In lower layers, the pressure is higher and the number of oxygen molecules is larger. Thus, an aerosol layer closer to the ground has a stronger effect on the TOA signal. Additionally, we observe that the ALH of dust is more sensitive, which can be explained by its optical properties (see Table 5.3). Dust is scattering more than smoke and thus, more light is reflected to TOA, reducing the interaction of the light with O_2. The largest sensitivity of the absorption-free signal can be observed for the AOT (Figure 5.5b). For small AOTs, the signal is changed by 200–380% for changes of 1 in the AOT in the absorption-free band. This strong dependence is true for both aerosol cases. The sensitivity is smaller with 80% for smoke and 60% for dust at AOT of 1. The influence of AOT on the absorption bands is reduced by taking the ratio of absorption band and absorption-free band. For the ratios, the sensitivity to the AOT is small with a maximum at 761.25 nm for small AOTs. The optical depth of dust influences the band ratio with up to 100% at small AOTs of 0.15. For larger optical thickness, the sensitivity to the AOT is reduced to less than 10 % for a change in AOT of 1 at 761.25 nm. The band ratios at 764.375 and at 767.5 nm are less sensitive for all AOTs.

The wind speed does not influence the TOA signal strongly for our study case of an off-glint case. Its sensitivity is negligible (see Figure 5.5c). For a glint observation geometry, the sensitivity is larger than for the off-glint case (see Figure 5.11). In the absorption-free band, the sensitivity can be as high as 3%, which is small compared to the sensitivity to AOT. For the glint case, the sensitivity to the ALH and the central wavelength are very similar compared to the off-glint case, and the sensitivity to AOT is reduced within the absorption-free bands. However, AOT can only be determined accurately for glint geometry with an exact description of the glint. If we assume a measurement uncertainty of about 0.5 % for OLCI and sensitivities to the ALH between 1 and 8 %, it is possible to retrieve the ALH from OLCI measurements both in off-glint
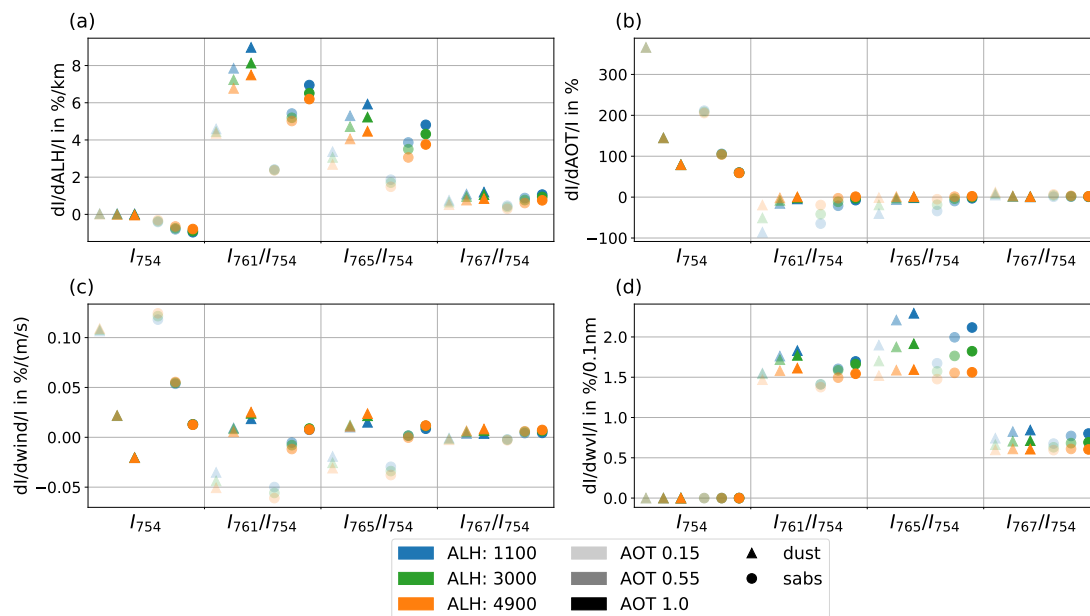
Figure 5.5   Jacobians of TOA radiance ratios at different central wavelengths relative to (**a**) ALH, (**b**) AOT, (**c**) wind speed and (**d**) central wavelength. Jacobians are given for two aerosol models (circles: SABS, triangles: dust) and for different AOTs (transparent: 0.15, non-transparent: 1.0). All results are given for SZA of 30°, VZA at 46° and AZI at 170°.

and glint geometries. Only aerosol layers with small AOTs are difficult to retrieve.

Another sensitivity parameter is the central wavelength (see Figure 5.5d). Again, the sensitivity is only high in the absorption bands, which is due to their steep and distinct nature. A change of the central wavelength of 0.1 nm changes the TOA signal between 1.5 and 2 % for both aerosol types. The sensitivity to the wavelength is larger than the uncertainty of the measurement and thus, it will be relevant in the retrieval. We use the temporal evolution model for the instrument characterization, which has an uncertainty of 0.1 nm. Hence, the accuracy of the definition of the central wavelength limits the retrieval accuracy. The wavelength uncertainty of 0.1 nm contributes to the uncertainty budget of the ALH by approximately 200 m in band Oa13, 500 m in band Oa14, and 1000 m in band Oa15. The uncertainty of the retrieval using all three bands simultaneously is further discussed in Section 5.5.

Using this sensitivity analysis, we showed that it is possible to retrieve ALH from OLCI measurements for dust and smoke with an resolution better than 1 km and with the restriction of a well known instrument characterization with a central wavelength accuracy of 0.1 nm. Additionally, the aerosol type must be known.

5.4.2 Retrieval of ALH for test cases

We apply the retrieval of the ALH to two scenes, one showing elevated dust particles over the Atlantic Ocean west of Africa and one showing smoke particles over the Pacific Ocean from a forest fire at the west coast of North America. For each scene, the LUT is chosen according to
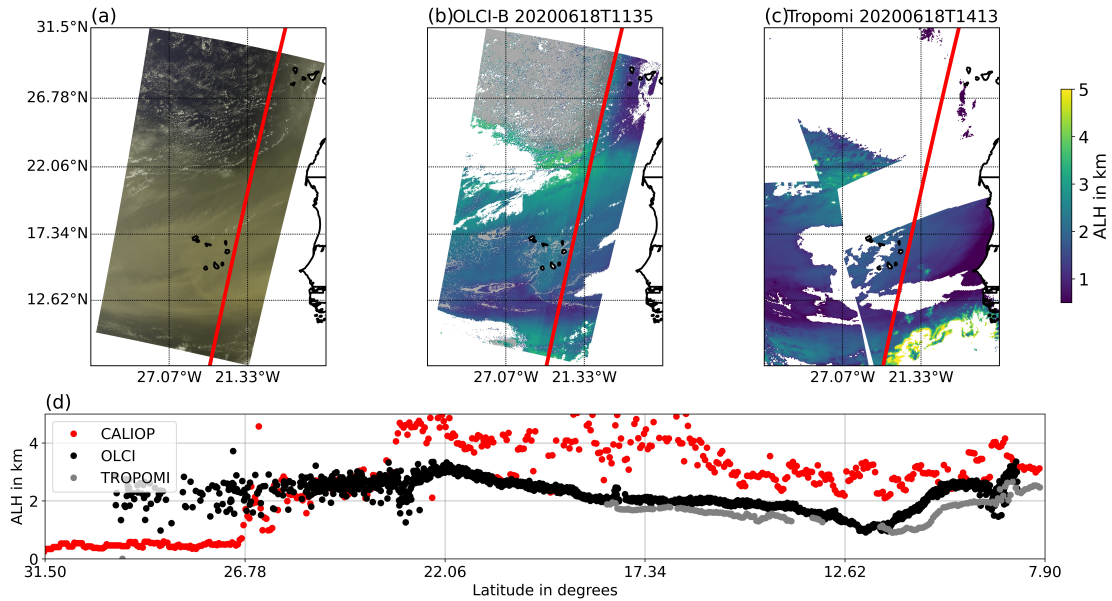
Figure 5.6 (**a**) RGB composite generated from OLCI L1 on 18/06/2020 between 11:35 and 11:38 UTC over the Atlantic west of central Africa. (**b**) Optimized ALH derived from OLCI-B measurements (**c**) TROPOMI ALH on 18/06/2020 at 14:13, 14:18 and 15:53 UTC. (**d**) CALIOP, OLCI and CALIPSO ALH along CALIPSO track on 18/06/2020 at about 03:29 UTC. White pixels are cloud flags, light grey pixels are non-convergence pixels and dark grey pixels are flagged out due to AOT smaller than 0.55. The red line in a–c shows the same CALIPSO track as in (**d**).

the known aerosol type and an a priori is assumed. We consider only pixels with a retrieved AOT larger than 0.55. This threshold is selected based on the sensitivity study and it can be further adjusted. For lower AOTs, the influence of a change in AOT by 0.1 is stronger than a change in ALH by 1 km.

Dust case

Two sequences of OLCI-B from 18/06/2020 over Cape Verde are evaluated and compared with TROPOMI and CALIOP (see Section 5.3.4). The true colour image (RGB) from OLCI-B is shown in Figure 5.6a. A thick dust cloud is visible with varying AOT. Only small parts of the images are covered by clouds. Clouds are flagged out using the IDEPIX algorithm, which is implemented in SNAP [Wevers et al., 2022]. The red line shows the CALIOP-track (of sub-satellite points) from 03:29 UTC in the upper subfigures. The two OLCI sequences are taken only 3 min apart from each other at 11:35 UTC and 11:38 UTC. Across the track, we cannot observe any camera artefacts.

Figure 5.6b shows the retrieved ALH in kilometers. Clouds are flagged out, which is indicated by white pixels. The retrieval did not converge for the light grey pixels, and the dark grey pixels are flagged out due to found AOT smaller than 0.55. The main reason for non-convergence is a low aerosol loading as present in the northwest. Comparing our results to the ALH retrieved from TROPOMI measurements (Figure 5.6c), we can observe the same distribution of

ALHs. A higher dust plume is present around 22°N, gradually decreasing southward. The lowest aerosol layers are at 12.6°N, which is true for both ALH retrievals from TROPOMI and OLCI. Higher particles are present at about 10°N. Overall, the OLCI ALH is a bit larger than the one of TROPOMI. The western TROPOMI images were recorded at 15:53 UTC and the eastern images at 14:13 and 14:18 UTC. The images fit together very well, which indicates a stable situation. Additionally, we investigated different CALIPSO overpasses at 03:29 and 15:29 UTC, which both showed a dust plume at the same height at similar latitudes. From these observations, we are confident, that we can compare our results measured between 11:35 and 11:38 UTC both with the TROPOMI data and the CALIPSO overpass at 03:29 UTC (see Figure 5.6d). The afternoon overpass of CALIPSO did not cover our study scene.

Figure 5.6d shows the weighted extinction from the CALIPSO overpass at 03:29 UTC and the co-located OLCI-B and TROPOMI ALHs. Along the CALIPSO track at 03:29 UTC, the overall ALH distribution from OLCI and TROPOMI is similar to the weighted extinction from CALIOP with the exception for higher latitudes. Here, only a few aerosol particles are present and the pixels are in the sun glint geometry (see Figure 5.12), which reduces the sensitivity of our retrieval. The TROPOMI ALH is flagged out in this part of the image. All valid TROPOMI ALH are very similar to the OLCI ALH with a slight negative median offset of about 0.5 km. Considering only latitudes between 8° and 23°N, OLCI's ALH is about 1.25 km lower than the one of CALIOP but closer to the CALIOP data than TROPOMI.

Smoke Case

We evaluate a smoke case using sequences of OLCI-A and OLCI-B from 08/09/2020 and nearest overpasses of CALIPSO and S5P. The true colour image generated from OLCI L1 measurements in Figure 5.7a shows a thick smoke plume over the Pacific Ocean west of California. The western image originates from OLCI-B. The eastern part of the image are two OLCI-A scenes. The red line marks the CALIOP track of sub-satellite points in all three upper subplots.

Figure 5.7b shows the retrieved ALH from those OLCI sequences. We did not apply the IDE-PIX cloud mask as it flagged our target smoke plume. Thus, Figure 5.7b does not show white marked pixels. The ALH retrieval flagged out the cloud pixels, e.g., in the northwest, anyway, as those pixels did not converge (see light grey pixels in Figure 5.7b). In addition to cloudy pixels, the retrieval also failed for parts of the smoke plume. Here, the L1 radiance was very bright which is not represented in our SABS LUT. However, the height of the eastern parts of the thick smoke plume (at longitudes between 124° and 130°W and latitudes between 45.5° and 41.5°N) could be estimated. The plume is low compared to the thinner plumes in the north (at longitudes between 124.5° and 132°W and latitudes between 47.5° and 46.5°N). In contrast, in the very south of the scene, the smoke plume is estimated at a high altitude of up to 5 km.

Comparing to TROPOMI's ALH given in Figure 5.7c, we can observe similar features in the ALH with high ALH in the south (at longitudes of around 123°W) and low ALH in the main plume (at longitudes between 124° and 130°W and latitudes between 45.5° and 41.5°N). Similar to our retrieval, TROPOMI flags out parts of the main plume (white pixels). Only in the
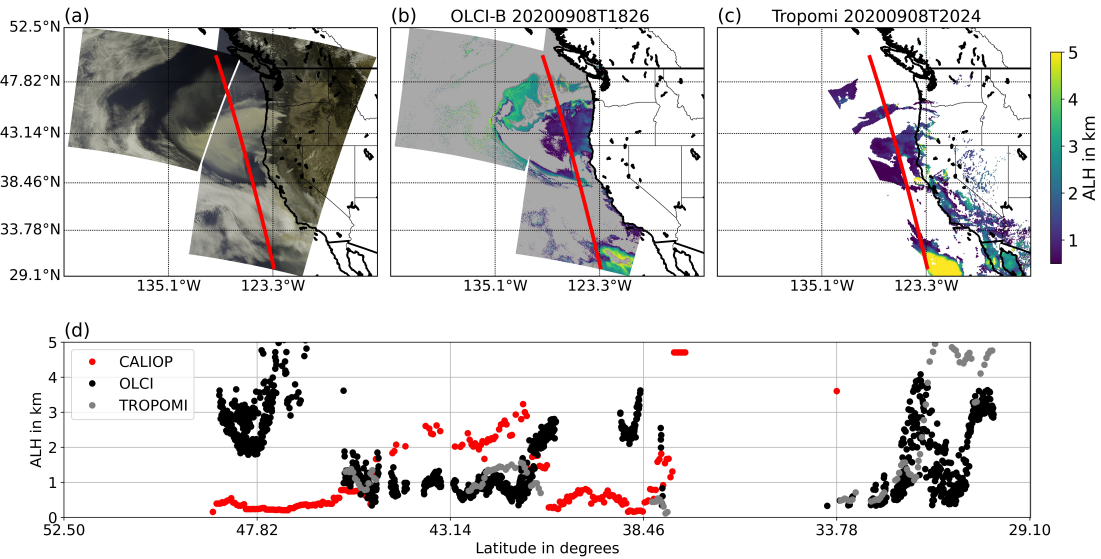
Figure 5.7   (**a**) RGB composite generated from OLCI L1 on 08/09/2020 at 18:26 UTC in west of California. (**b**) Optimized ALH derived from OLCI-B measurements. (**c**) TROPOMI ALH on 08/09/2020 at 20:24 and 20:29 UTC. (**d**) OLCI, CALIPSO and TROPOMI ALH along CALIPSO track on 08/09/2020 at 21:27 UTC. The red line in a–c shows the same CALIPSO track as in (**d**).

northwest (at longitudes between 134° and 130°W and latitudes between 47.8° and 45.5°N), our results deviate from TROPOMI's ALH. Our ALH (about 3 km) is higher than the one of TROPOMI (about 1 km). Here, the AOT is lower than in the main plume.

The direct comparison of OLCI, TROPOMI, and CALIOP in Figure 5.7d also shows a good agreement of OLCI and TROPOMI. In the south, at around 31° N, TROPOMI measures a high aerosol layer, whereas OLCI detects a low ALH. However, this area is very cloudy and the conditions could have changed slightly between 18:26 UTC (OLCI overpass) and 20:24/20:29 UTC (TROPOMI overpass). Both retrieval results show differences compared with the weighted extinction measured by CALIOP. The main smoke plume is observed between 40 and 45° N. Here, OLCI's and TROPOMI's ALH are more than 1 km lower. In the north at around 47.8° N, our estimated ALH is higher than the CALIOP one. The difference in the north could be either explained by difference in measurement time or uncertainties within our retrieval. As TROPOMI also shows lower values in the north than OLCI, the discrepancy might be the result of a high uncertainty due to the small AOT for those pixels.

5.5 Uncertainty propagation

We estimate the uncertainty of the retrieved ALH by applying a complete linear uncertainty propagation and using a bootstrap method evaluating simulated radiances with known noise. For both methods, all uncertainty sources must be quantified. For some parameters we could only guess them in all conscience. Nevertheless, by applying both methods we can give a sophisticated guess of the ALH uncertainty.

Table 5.2　Input for simulated truth and assumed uncertainty for the uncertainty propagation.

Parameter	Input Values	Uncertainty
ALH in m	450, 750, 1000, 3000, 5000	-
AOT	0.55–5.5	-
wind speed in m/s	4, 6, 8	+/− 1
SZA in Degrees	25–40	+/− 3
VZA in Degrees	0–60	+/− 3
AZI in Degrees	10–50; 130–150	+/− 3
wvl in nm	753.75, 761.25, 764.375 and 767.5	+/− 0.1

5.5.1 Linear uncertainty propagation

The linear uncertainty propagation is based on the error covariance matrix calculated with Equation (5.6). It includes the a priori error covariance, the Jacobians with partial derivatives of the radiance with respect to the ALH and the error covariance matrix $\mathbf{S_e}$, which is substituted by the sum of all known uncertainty sources (adapted from [Rodgers, 2000]):

$$\mathbf{S_e^*} = \mathbf{S_{e_{param}}} + \mathbf{S_{e_{SNR}}} + \mathbf{S_{e_{wvl}}} \tag{5.9}$$

$\mathbf{S_{e_{param}}}$ is calculated with parameter error covariance matrix $\mathbf{S_{param}}$, which is in the parameter space. $\mathbf{S_{param}}$ includes the input parameter uncertainties, which are transformed to the measurement space using the derivatives of the TOA signal with respect to the parameters (parameter Jacobian $\mathbf{K_{param}}$) (adapted from [Rodgers, 2000]):

$$\mathbf{S_{e_{param}}} = \mathbf{K_{param}}^T \mathbf{S_{param}} \mathbf{K_{param}}. \tag{5.10}$$

The diagonal elements of $\mathbf{S_{param}}$ are the approximated uncertainties of the wind speed, the SZA, VZA and AZI, which are summarized in Table 5.2. The angles have a very small uncertainty. Nevertheless, we chose perturbations up to $3°$ to change the scattering angle slightly and thus, change the sampling point of the phase function. The off-diagonal elements of $\mathbf{S_{param}}$ are set to zero because the wind speed and the observation geometry are not correlated.

$\mathbf{S_{e_{SNR}}}$ gives the contribution of the measurement uncertainty on the diagonal matrix elements (see Table 5.1). The off-diagonal elements of $\mathbf{S_{e_{SNR}}}$ are set to zero since correlations are not quantified in the instrument characterization. Hence, this uncertainty source is neglected.

The uncertainty contribution of the wavelength is estimated comparing two sets of forward simulations for which known state parameters of all valid pixels including the retrieved ALH and AOT have been applied. One set of forward simulations uses the correct central wavelength, and one set is based on a spectral response function shifted by 0.1 nm. Both sets of simulations are created for all four bands. The mean squared difference of those two sets gives an estimate of the contribution by the wavelength uncertainty. The elements of the error covariance matrix are
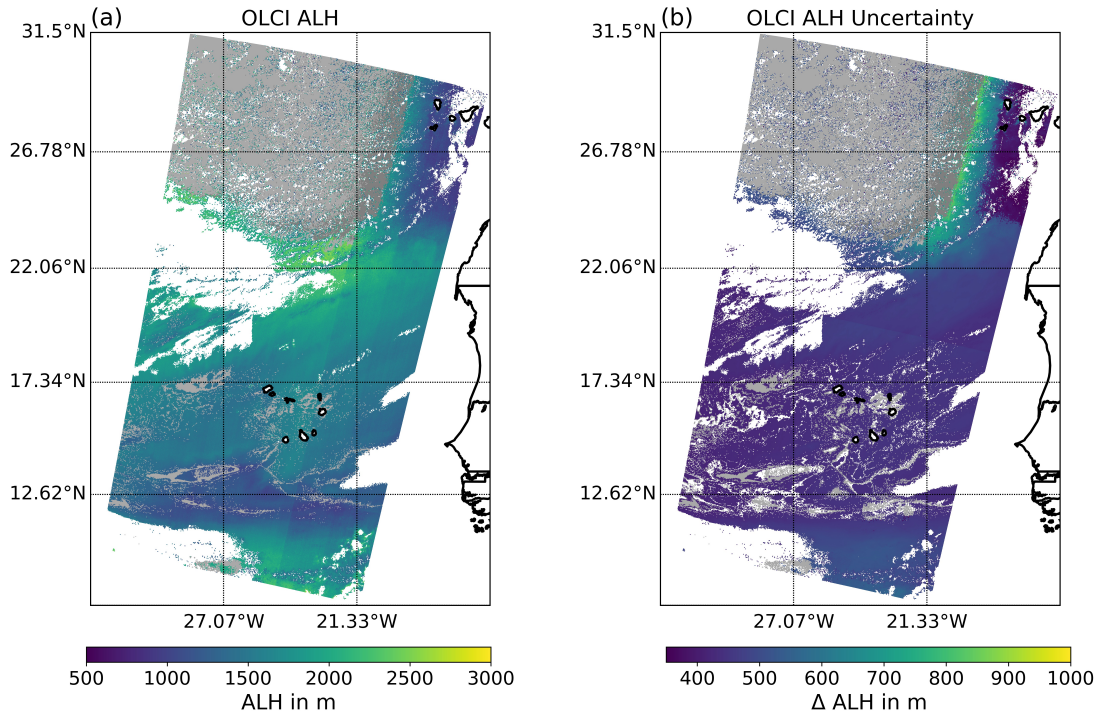
Figure 5.8   (**a**) Optimized ALH derived from OLCI-B measurements on 18 June 2020 between 11:35 and 11:38 UTC over the Atlantic west of central Africa. (**b**) Estimated pixelwise uncertainty using linear uncertainty propagation. White pixels are cloud flags, light grey pixels are non-convergence pixels and dark grey pixels are flagged out due to AOT smaller than 0.55.

calculated by multiplying the square root of mean squared differences of the bands scaled with the correlation coefficient c_{ij}:

$$\mathbf{S_{e_{wvl}}}_{ij} = \sqrt{\frac{\sum(I_i^0 - I_i^{0.1})^2}{N}} * \sqrt{\frac{\sum(I_j^0 - I_j^{0.1})^2}{N}} * c_{ij}. \tag{5.11}$$

i, j are integers between 0 and 3 counting the dimension of the used bands, and N counts all pixels.

The pixelwise uncertainty is presented in Figure 5.8 for the dust case study scene and in Figure 5.9 for the smoke case study scene. Both figures show the retrieved ALH and the corresponding uncertainty for all valid pixels. As described before, cloudy pixels are flagged out with white colour, non-converging pixels are shown in light grey, and in dark grey are all pixels with retrieved AOT smaller than 0.55. Pixels with small optical thickness have a large ALH uncertainty. In the northeast in Figure 5.8 at the border to the flagged out pixels, the uncertainty is about 1000 m. The reason for the high uncertainty in this area is the combination of a low AOT and the sun glint. The dependence of the ALH uncertainty on the AOT is discussed in more details in Figure 5.14a. A decrease in the uncertainty of the ALH is shown for decreasing AOT, which is more prominent in the sun glint area. The observation geometries and the sun glint risk
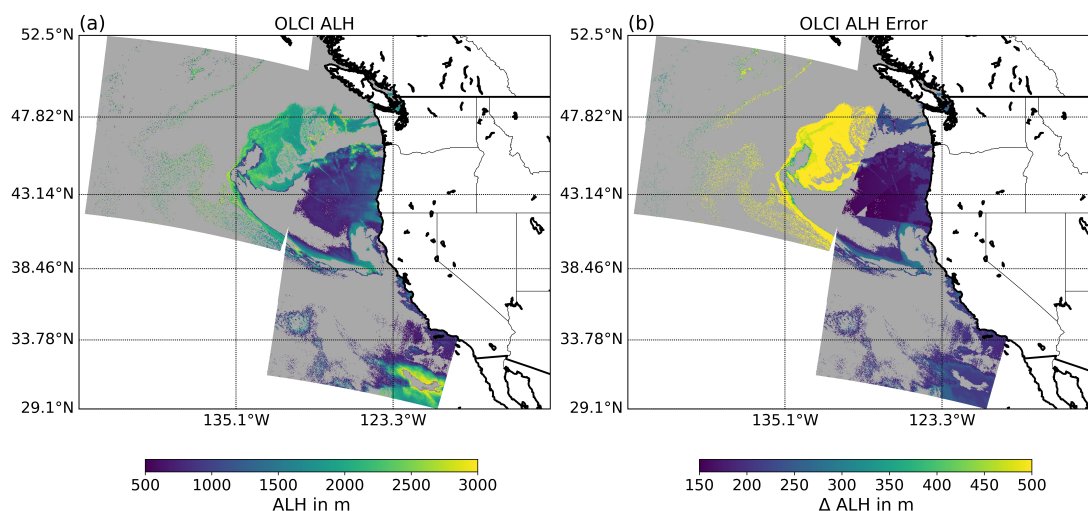
Figure 5.9   (**a**) Optimized ALH derived from OLCI measurements on 08/09/2020 at 18:26 UTC over the Pacific west of California. (**b**) Estimated pixelwise uncertainty using linear uncertainty propagation. White pixels are cloud flags, and light grey pixels are non-convergence pixels.

area according to the L1 flag are shown in Figure 5.12. In the upper right corner of the image, the uncertainty is low even though it is still in the glint area. However, the thick AOT reduces the sensitivity to the glint for this scene. The same is true for the southern glint area (east of the image). Here, the uncertainty is not higher than in the rest of the scene. The optical thick dust cloud reduces the effect of the glint and the ALH can be retrieved with a good precision. Over all, the uncertainty of the ALH for the dust scene is mostly between 400 and 600 m with no dependency on the ALH. With this precision, we can distinguish between low, medium and high aerosol layers even with OLCI's low spectral resolution.

The precision for the smoke case in Figure 5.9 is even higher. Especially in the area of large AOTs, the uncertainty ranges between 150 and 300 m. Only in the northwest, where the AOT is small, the uncertainty is up to 800 m. At the border between the OLCI-A and OLCI-B image, a jump in the uncertainty can be observed which is not present for the ALH itself. The uncertainty is high for the observations in glint geometry and low for the off-glint geometry. This effect is discussed in the Appendix (see Figure 5.14b). The jump in uncertainty in our test scene must be differentiated between the northern part, where the AOT is low in both, S3A and S3B sequence, and the southern part, where the AOT is only low in the S3B sequence. In the northern part, the jump can be explained by the difference in geometry (see Figure 5.14b). The southern part differs in the AOT strongly and thus the ALH uncertainty decreases from west to east. The glint risk areas are shown in Figure 5.13.

5.5.2 Uncertainty based on bootstrap method

In the bootstrap method, noisy simulated radiances serve as input for the retrieval. The retrieved ALH is compared to the result of the retrieval for the same simulated radiance measurement
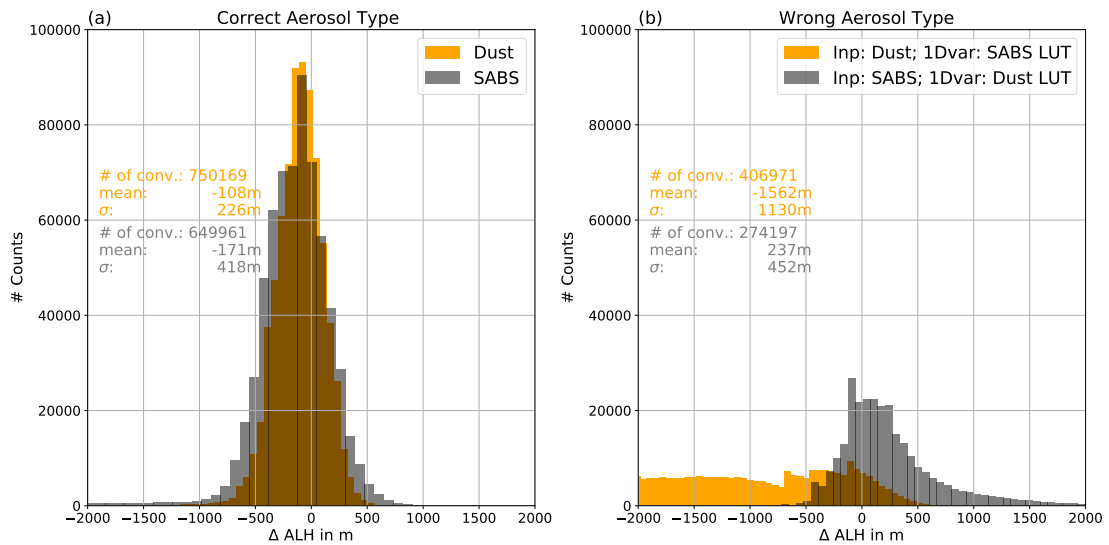
Figure 5.10   Histograms of differences of all 1,000,000 retrieved ALH with and without noise for dust in yellow and SABS in grey using the LUT (**a**) based on the correct aerosol type and (**b**) based on the wrong aerosol type.

but without noise. As a first step, about 37,000 cases were simulated to serve as truth. Those cases result from all possible combinations of chosen ALH, AOT, wind speed and measurement geometries. All simulations were performed at the nominal central wavelength and a shifted central wavelength by $+/-$ 0.1 nm. The ranges of the input parameter and the respective noise are given in Table 5.2. The a priori knowledge for the retrieval is chosen to be 1000 m for the ALH and 3.5 for the AOT in all cases. The a priori and the state error covariances are given in Table 5.1.

Our bootstrap method comprises 1,000,000 iterations. Each time one of the 37,000 truths were selected randomly. Additionally, the other input parameters were chosen randomly within their uncertainty range (Table 5.2). The retrieval is done for the perturbed pixels and the truth. The frequency distribution of the difference of both retrieved ALH is given in a histogram in Figure 5.10. The method is applied for 37,000 dust and 37,000 SABS cases. To study the uncertainty according to the aerosol type, the method is also applied on simulated truth with dust particles which are retrieved using LUTs based on SABS particles and vice versa. The corresponding frequency distributions of differences in the ALH are given in Figure 5.10b.

The histograms in Figure 5.10 show only cases in which the retrieval converged. In the case of dust, about 75% of all cases converged, and in the case of SABS, about 65% converged. Most non-converging pixels belong to low AOT cases. The distributions of the difference for retrieved truth with and without noise with the correct aerosol type show a Gaussian-like shape with a small negative bias. The dust case distribution is less wide than the SABS case as the optical properties of dust have a stronger contrast to the signal originating from the ocean surface. The standard deviation is 230 m for dust cases. The standard deviation for SABS cases is 420 m.

The investigation using the wrong aerosol types shows larger differences between perturbed

and non-perturbed retrieved ALH. In particular, the retrieval for the dust aerosol layer based on SABS LUTs does not show a Gaussian shape (yellow histogram in Figure 5.10b). Here, the AOT can not compensate due to the error in the aerosol type. The optical properties of SABS cause a saturation of the TOA radiance for AOTs larger than 5. Thus, the SABS LUT is limited to smaller radiances. The retrieval based on the dust LUT is more robust with regard to the aerosol type. The distribution is almost Gaussian with a standard deviation of 630 m. With this uncertainty, we can still find appropriate ALH even using the wrong aerosol type. However, the retrieval does not converge as frequently in both cases. Thus, our retrieval method is rather applicable for cases of a known aerosol type.

5.6 Discussion

This study contains a sensitivity analysis for the radiance in OLCI's O_2 absorption bands with respect to ALH, the application of an ALH retrieval to two OLCI test scenes over ocean and an appropriate uncertainty estimation. We found that band ratios of OLCI bands within the O_2A absorption band are sensitive to ALH. A retrieval of ALH is possible for thick dust and smoke plumes if the aerosol type is known and the spectral characterization of the instrument is considered. The sensitivity of the absorption bands to the ALH increase for increasing AOTs. Hence, we chose an AOT of 0.55 as threshold for the application of the ALH retrieval. Pixels with lower AOT are flagged out after the retrieval. This threshold was chosen to minimize the uncertainty of ALH which decreases with AOT. In a MERIS study under similar conditions and a similar accuracy of the spectral characterization by Dubuisson et al. [2009], they found a standard error on the retrieval of the altitude of 0.5 km for an AOT of 0.6. Their retrieval was limited on the ALH assuming a known AOT. Dubuisson et al. [2009] also showed that for low AOTs, the method is less accurate.

The ALH could be retrieved from OLCI for the dust and the smoke test scene with an uncertainty between 400 and 600 m for a dust scene and with uncertainty as low as 150 m for the smoke scene for off-glint pixels with a low ALH and high AOT. Our generalized uncertainty estimation using the bootstrap method based on simulated measurements resulted in uncertainties of 230 m for dust and 420 m for SABS. Those ALH uncertainties are comparable to the MERIS results shown in Dubuisson et al. [2009]. Our uncertainty analysis does not include uncertainties due to the surface pressure, which is a sensitive parameter within the O_2A absorption band. We minimized the uncertainty due to the surface pressure by selecting a matching surface pressure to the test scenes for the simulation.

The retrieval was not successful for pixels with small optical thicknesses or undetected clouds. For converging pixels, we found very similar ALHs for optical thick aerosol layers compared to the TROPOMI ALH. The median difference was about 500 m for the dust case, which lies a bit above our estimated uncertainty range. Comparing OLCI's ALH to the weighted extinction from CALIOP, the weighted extinction is about 1.25 km higher than OLCI's dust ALH. This difference could have several reasons, e.g., the definition of height or the set up of our retrieval

using a fixed aerosol model and homogeneous aerosol layer. Nevertheless, our ALH follows the pattern of the one measured by CALIOP. Thus, our aim of distinguishing low, medium and high aerosol layers from OLCI's O_2 absorption bands is achieved. Additionally, OLCI's high spatial resolution allows the observation of very fine spatial structures in the ALH.

The smoke case pixels did not converge as frequently even for large optical thicknesses. Our SABS LUT is limited to relatively small radiances due to the optical properties of SABS. Real-case smoke not only contains SABS but also other particles. For future retrievals, a more complex aerosol model could be used. Converged pixels showed similar ALHs as retrieved from TROPOMI. As for the dust case, those ALHs were lower than the ones measured by CALIOP.

Our retrieved ALH showed systematic differences compared to the height from CALIOP. Similarly, validation studies for TROPOMI's ALH resulted in differences between TROPOMI and CALIOP for thin smoke plumes of about 700 m [Griffin et al., 2020], of 1030 m for different cases [Nanda et al., 2020] and of 510 m for dust and smoke cases over ocean when comparing with a ground-based LIDAR (EARLINET) [Michailidis et al., 2023]. Generally, TROPOMI measured lower ALHs than CALIOP, which we also observed in our test scenes. Overall, the differences between OLCI's ALH and CALIOP's ALH are comparable to the ones found for TROPOMI. Chen et al. [2021] developed an improved ALH retrieval algorithm for TROPOMI, including also the O_2B band. The improved TROPOMI algorithm is applied to the same test scenes as described in this paper. Using also the O_2B band, the ALH is about 2 km higher in the dust case and about 1 km higher in the smoke case compared to the standard TROPOMI ALH product [Chen et al., 2021]. Compared to our ALH product, the improved ALH agrees better with the CALIOP observations. However, OLCI does not cover the O_2B absorption band and thus, this improvement can currently not be applied for OLCI. The planned advanced OLCI will be hyperspectral, covering both O_2A and O_2B bands. Hence, the future OLCI version could be even more suitable for ALH retrievals.

Our sensitivity study and retrieval algorithm are limited to two aerosol models, one homogeneous aerosol layer and an underlying ocean surface. We showed that the retrieval works more robustly knowing the aerosol type. However, in operational cases, it is difficult to determine the aerosol type. We showed that the retrieval based on a dust aerosol model converges for some cases without a large increase in the uncertainty. In future, either an aerosol type characterization based on the complete spectral range of OLCI or a synergy product with Sentinel-3 Sea and Land Surface Temperature Radiometer (SLSTR) could be developed to distinguish between dust and smoke aerosol. Another possibility to characterize the aerosol type is to use Copernicus Atmosphere Monitoring Service (CAMs), which delivers information about aerosol [Peuch et al., 2022]. Our retrieval is limited to scenes with large AOTs. It is successful with an uncertainty of a few hundred meters which was demonstrated for two test scenes. Further validations are necessary, e.g., compassion with ground-based measurements. We did not study the effect of different vertical distributions on the uncertainty. In nature, the vertical profile can be very complex with exponential decays or multi-layer profiles. The limited spectral resolution does not provide information about the vertical distribution. Hence, the remaining uncertainty should be estimated. Furthermore, the retrieval could be generalized also for land surfaces. For a retrieval

of the ALH over land, the surface must be very well spectrally characterized.

Overall, we could show that it is possible to retrieve the ALH from OLCI measurements, which could allow the determination of ALH for long time series, improvement of ocean colour products, improvement of atmospheric corrections and further studies of aerosol cloud interactions. Even with the limited precision due to OLCI's spectral resolution, the ALH retrieved by OLCI has a high spatial resolution and coverage. Thus, OLCI can deliver useful information about the aerosol vertical distribution.

5.7 Appendix

5.7.1 Aerosol optical properties

The optical properties at 755 nm are shown for dust and SABS in Table 5.3. Comparing dust and SABS, the SSA of dust is almost one, whereas the SSA of SABS is smaller than one. The relative extinction coefficient is given as ratio of the extinction coefficient at 550 nm and 755 nm. The dust relative extinction coefficient larger than one shows its strong scattering properties, whereas SABS absorbs more light than it scatters. The wavelength-dependency of the extinction coefficient is given by the angstrom exponent given for the wavelengths 550 nm and 755 nm. The wavelength dependence of the phase function $p(\Theta)$ is given by the asymmetry factor g [Kokhanovsky and Leeuw, 2009]:

$$g(\lambda) = \frac{1}{2} \int_{-1}^{1} p(cos\Theta)dcos\Theta \tag{5.12}$$

Table 5.3   Aerosol optical properties at 755 nm for dust and SABS.

Aerosol Property	Dust	Strong Absorbing Aerosol
SSA	0.98	0.76
Rel. Extinction coeff. to 550 nm	1.04	0.56
Angstrom exponent (755/550)	-0.11	1.748
Asymmetry factor g	0.72	0.565

5.7.2 Harmonization method

The background of the harmonization is a sensitivity factor of the apparent transmission t calculated from the normalized radiances I_i^N measured outside and within the absorption band:

$$t = \frac{I_i^N}{I_{12}^N}(i = 13, 14, 15) \tag{5.13}$$

ξ quantifies deviations due to changes of the band central wavelength and bandwidth with respect to their nominal spectral characterization. The foundation is a look-up table that has been calculated from transmissions for nominal band characteristics as well as for all sensible modifications of the band characteristics. The sensitivity factor is the ratio between the transmission with actual band characteristics to the transmission with nominal characteristics.

$$\xi = \frac{t(\lambda, FWHM)}{t_{nominal}} \tag{5.14}$$

The sensitivity factor has been calculated for a multitude of photon paths through an atmosphere, reflecting cases without clouds, with thin, thick, high and low clouds above dark and

bright surfaces. The gas absorption is based on HITRAN16 [Gordon et al., 2017]. Eventually, 30,000 different photon paths have been considered. The look-up table is utilized by a KD-search [Bentley, 1975] and an inverse distance weighted interpolation. This approach is well suited for data that cannot be structured in an hypercube.

The harmonization works as follows. First, the OLCI bands 12–16 are normalized with respect to their corresponding in-band solar irradiance F.

$$I_i^N = \frac{I_i}{F_i} (i = 12, ..., 16)$$

(5.15)

Then, the window bands 12 and 16 are interpolated to the spectral position of the bands 13, 14 and 15, respectively:

$$\tilde{I}_i^N = \frac{I_{16}^N - I_{12}^N}{\lambda_{16} - \lambda_{12}} \cdot (\lambda_i - \lambda_{12})(i = 13, 14, 15)$$

(5.16)

The apparent transmission is now calculated with

$$t_i = \frac{I_i^N}{\tilde{I}_i^N}(i = 13, 14, 15)$$

(5.17)

For every pixel and band, the sensitivity factor ξ is searched within in the look-up table, based on the following four quantities: the apparent transmission t_i, the pixel specific central wavelength λ, the bandwidth $FWHM$ and the air mass factor amf.

$$amf = \frac{1}{cos\theta_{VZA}} + \frac{1}{cos\theta_{SZA}}$$

(5.18)

The look-up table search, as well as the inverse distance weighting, uses normalized quantities, but we refrain from further indexing to maintain clarity.

$$x_{norm} = \frac{x}{x_{max} - x_{min}}$$

(5.19)

x_{max} and x_{min} are the smallest and largest values of the respective coordinate. The eight closest matches are used to calculate an estimate of ξ by an inverse distance-weighted mean.

$$\xi_i^{pixel} = \frac{1}{\sum\limits_{j=0}^{8} w_i^j} \cdot \sum_{j=0}^{8} w_i^j \cdot \xi_i^j \ (i = 13, 14, 15)$$

(5.20)

ξ_i^j is the sensitivity factor of band i of the j closest neighbours. The weight w is the inverse Euclidean distance:

$$w_i^j = \frac{1}{\varepsilon + \sqrt{(amf^{pixel} - amf_j)^2 + (\lambda_i^{pixel} - \lambda_i^j)^2 + (FWHM_i^{pixel} - FWHM_i^j)^2 + (t_i^{pixel} - t_i^j)^2}}$$

(5.21)

ε is a small number, preventing division by zero for cases where the closest distance is zero.

The final step is the calculation of the apparent transmission at nominal position:

$$t_i^{nominal} = \frac{t_i}{\xi_i^{pixel}}(i = 13, 14, 15) \tag{5.22}$$

5.7.3 Sensitivity study for glint scene
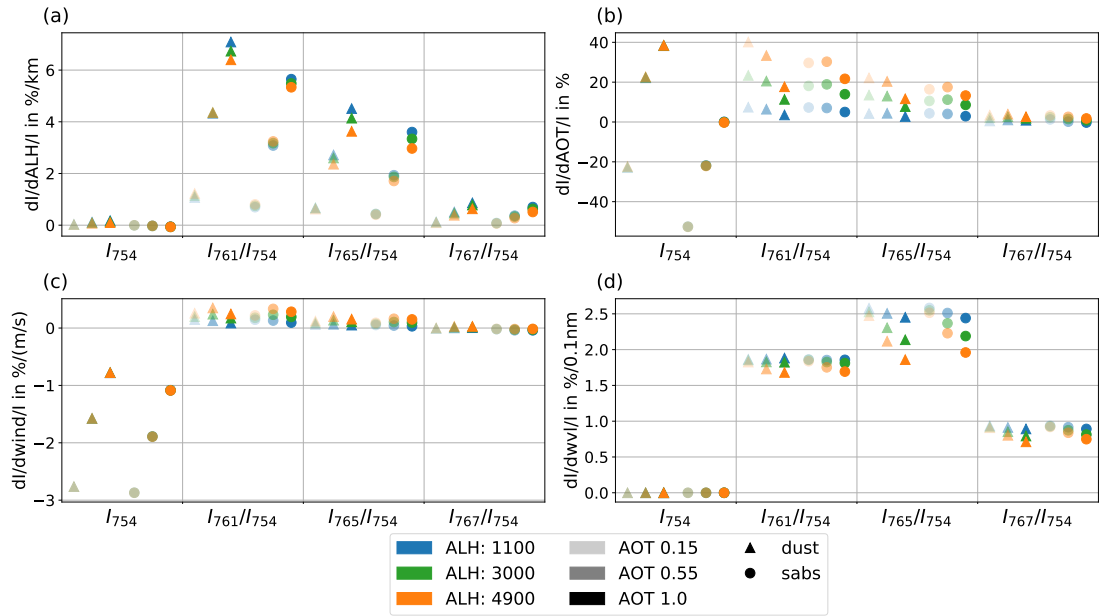
Figure 5.11 Jacobians of TOA radiance ratios at different central wavelengths relative to the ALH, AOT, wind speed and central wavelength. Jacobians are given for two aerosol models (circles: strong absorbing, triangles: dust) and for different AOTs (transparent: 0.15, non-transparent: 1.0). All results are given for SZA of 30°, VZA at 46° and AZI at 10°.

5.7.4 Sun glint geometry for test scenes

Both test scenes are over ocean surfaces under cloud-free conditions. Under certain sun and observation geometries, sun light is strongly backscattered by the ocean surface. The size of this area depends on the surface roughness and thus, the wind speed. This area is called sun glint. OLCI's L1 data includes a sun glint risk flag, which is presented in Figure 5.12a for the dust test scene and in Figure 5.13a for the SABS scene. The congruent sun and observation angles are shown in Figures 5.12b–d and 5.13b–d.
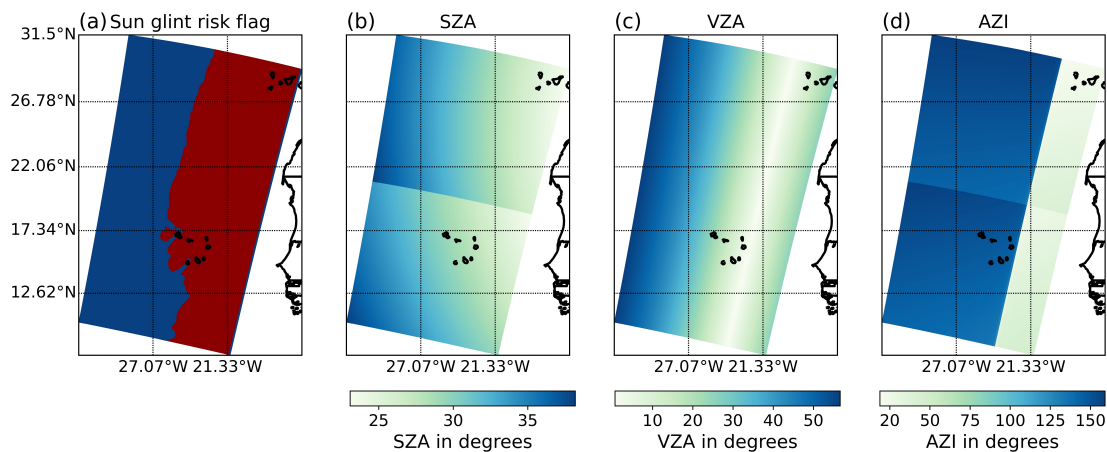
Figure 5.12   (**a**) Sun glint risk flag for dust test case on 18/06/2020 at the west coast of Africa. For the red pixels, the sun glint risk is true, and for blue pixels, it is false. (**b**) SZA in degrees for the two OLCI-B sequences. (**c,d**) VZA and AZI in degrees for the two OLCI-B sequences, respectively.
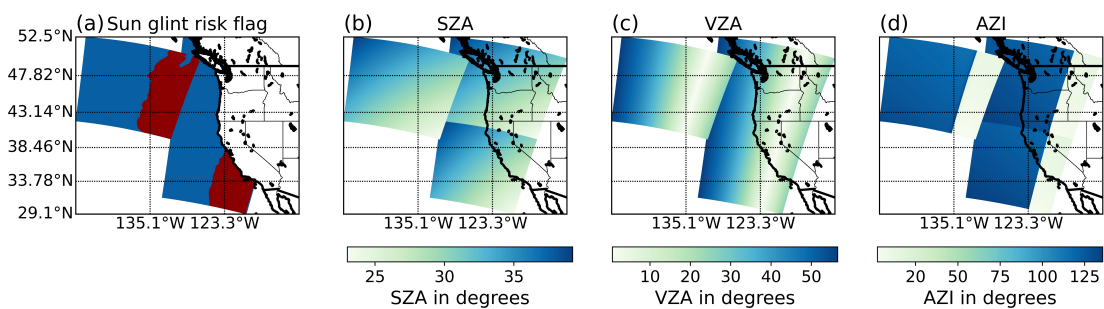
Figure 5.13   (**a**) Sun glint risk flag for dust test case on 08/09/2020 at the west coast of North America. For the red pixels, the sun glint risk is true, and for blue pixels, it is false. (**b**) SZA in degrees for the OLCI-A and OLCI-B sequences. (**c,d**) VZA and AZI in degrees for the OLCI-A and OLCI-B sequences, respectively.

5.7.5 Uncertainty of ALH depending on AOT

The uncertainty of ALH is studied with respect to AOT. We simulated cases with dust and SABS particles for different observation geometries which are representative for the geometries at the western and eastern border of the S3A and S3B sequences. The SZA was chosen according to the test scene over the west coast of north America on 08/09/2020 (Figure 5.7). The eastern geometries are a SZA of 40°, a VZA at 50° and an AZI at 150°, and the western geometries are a SZA of 40°, a VZA at 25° and an AZI at 40°. We calculated the retrieval error covariance matrix (Equation (5.6)), which includes uncertainty of the retrieval parameter ALH and AOT. To include the same uncertainty for the wind speed of 1 m/s as assumed in Section 5.5.1, we simulated the effect of the wind speed change of 1 m/s. The simulation was used to calculate corresponding uncertainty, which is added to the radiance uncertainty.

In all cases, the uncertainty of the ALH decreases with the AOT with a saturation at an AOT of about 1. For AOTs larger than 0.55, all uncertainties are below 500 m. The ALH uncertainty is similar for aerosol at different heights. The eastern, glint-influenced simulations show a larger uncertainty than the western ones. Both geometries differ in the scattering direction of the aerosol, while the western geometry is pointed in the back scattering direction and the eastern in the forward scattering direction. Additionally, the sun glint effects only the eastern simulations, which increases the ALH uncertainty further.
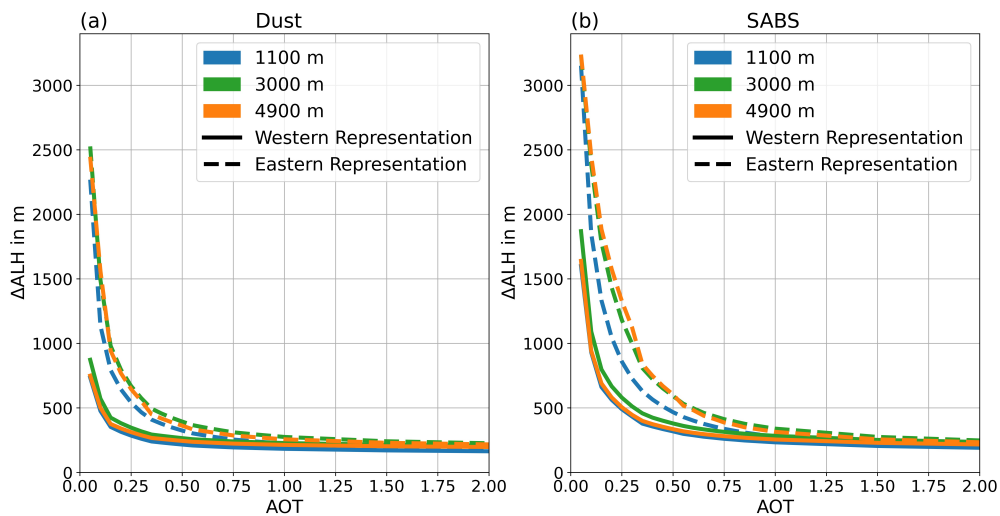
Figure 5.14   Uncertainty of ALH from retrieval error covariance matrix over AOT for different simulated dust cases (**a**) and SABS cases (**b**) with observation geometries of (i) the western representation (solid lines): SZA of 40°, VZA at 50° and AZI at 150° and (ii) the eastern representation (dashed lines): SZA of 40°, VZA at 25° and AZI at 40°. The colours show simulations with different ALHs: blue: 1100 m; green: 3000 m and orange: 4900 m.

6

Synthesis

The studies presented in this thesis serve as preparation for the challenging FLEX mission which shall be launched in 2025. They can contribute to the validation of FLEX. Two of these studies describe the validation of L1 radiance data and the validation of the retrieved surface reflectance. The L1 data can be validated by comparing FLORIS data with data from OLCI. This validation concept was tested by developing a transfer function that was applied on S3A and S3B tandem mission in which OLCI-B mimicked FLORIS. The surface reflectance contains the fluorescence signal. Thus, it is important to validate that signal in order to ensure a valid interpretation.

The surface reflectance can be validated with ground-based measurements. The ground-based instruments can be frequently calibrated in the laboratory and atmospheric correction is less challenging for measurements close to the surface. Nevertheless, the validation with ground-based measurements has also draw backs which originate mainly from heterogeneous surfaces. Airborne measurements were evaluated to identify suitable ground-based measurement sites and to quantify the uncertainty of the validation due to differences in spatial resolution and due to geolocation mismatch for an exemplary site.

The third study presented in this thesis focused on the estimation of the aerosol layer height from OLCI measurements. The aerosol layer height is crucial for the atmospheric correction within the fluorescence retrieval but also for climate and aerosol transport models.

All three studies contribute to answer the research questions expressed in the introduction of this thesis.

> **How can two TOA measurements from sensors with different spectral characteristics be compared? Is there a systematic difference of the radiometry between OLCI-A and OLCI-FLEX?**

These two questions were addressed in Chapter 3 in which TOA radiance data with different spectral responses were evaluated. The data were measured by OLCI-A and OLCI-B in FLEX configuration while S3A and S3B were flying in a tandem constellation. This constellation ensured that both instruments were observing the same geographic target within a few seconds.

Hence, the environmental conditions of the atmosphere and the surface which influence the TOA radiance were the same for both measurements. If this requirement is not fulfilled, a comparison of two TOA signals is significantly more complex. Another requirement is the observation with the same spatial resolution, which is fulfilled for both the S3 tandem mission in 2018 and the future S3-FLEX tandem mission.

Knowing the environmental conditions, the difference in spectral response can be overcome by applying a transfer function. Furthermore, the transfer function could also overcome differences in observation and sun geometries which also influence the TOA radiance. Information about the atmosphere and the surface are gained from the higher resolution instrument (OLCI-FLEX). The information is shifted to the central wavelengths of the second instrument and convolved with its spectral response function. Using radiative transfer simulations, this information is then used to forward simulate TOA radiance at the spectral bands of the low resolution instrument (OLCI-A) with the correct observation and sun geometry. The simulated TOA radiance based on the high resolution measurement can be compared with the low resolution measurements for validation purpose.

The transfer function has been applied successfully to the tandem data set of OLCI-A and OLCI-FLEX. Systematic differences of about 2 % have been quantified with OLCI-A measured brighter radiances than OLCI-FLEX. At longer wavelengths, the differences reached up to 5 % with opposite sign. The results from the method were verified by a similar comparison of OLCI-A and OLCI-B in nominal configuration. Lamquin et al. [2020] showed systematic differences of 2 % between OLCI-A and OLCI-B. As the 5 % difference only occurs in the FLEX configuration, we assumed that this difference results from issues within the processing. Furthermore, artefacts within the weak absorption bands were observed which might result from band filling with spectral stray light. Comparing to the results of Lamquin et al. [2020], less strong fluctuations of the bias within the oxygen absorption band were found. This improvement is accomplished by using the temporal evolution model of the spectral response function of OLCI and OLCI-FLEX. Hence, an accurate knowledge of the spectral response is necessary to compare two TOA radiances with different spectral responses.

For the FLEX and S3 tandem constellation, a validation of FLORIS measurements with OLCI data is possible. The difference in spectral resolution can be overcome by convolving the FLORIS data with OLCI spectral response functions within the spectral range between 500 and 700 nm. Between 700 and 800 nm, a transfer functions as described in this thesis must be applied to overcome the difference in spectral characterization.

With the application of the transfer function, a band by band validation is not possible. Instead, it results in an estimation of systematic differences at the lower resolution bands only. Another limitation is that a statistical evaluation of the systematic bias is necessary to overcome uncertainties in the georeferencing which is up to 0.5 pixels for OLCI and FLORIS [Drinkwater and Rebhan, 2007, Drusch, 2018]. Hence, a pixel-wise estimation of the systematic biases is not possible. Furthermore, the method is limited to tandem missions.

Which surface and atmospheric parameters are necessary for an adequate description of the radiative transfer at wavelengths between 500 and 780 nm to enable comparison of sensors with different spectral response?

For a successful comparison of two sensors with different spectral characteristics, the sharp and distinct spectral features of the considered spectral range must be well described by the higher resolution measurements. Between 500 and 800 nm, those spectral features are the oxygen absorption bands at 680 and 760 nm, the water vapour absorption at around 710 and 800 nm and the complex spectra of the surface reflectance of vegetation. The TOA radiance is also influenced by aerosol. Thus, it must be characterized. However, its spectral pattern is very smooth which allows simple interpolation algorithms.

For the comparison of the OLCI-A/OLCI-FLEX data set, it was shown that the accuracy of the comparison depends on the position of the two spectral band sets. The spectral bands of the higher resolution sensors must cover the above mentioned spectral features well. Furthermore, the bands should be close to the bands of the lower resolution sensor. The largest influence on TOA radiance has the surface reflectance. The surface description of vegetated surfaces from OLCI-FLEX was not sufficient to reproduce the OLCI-A surface reflectance with high accuracy. To fill this gap of information, a PCR was implemented which was based on additional information from surface reflectance data bases. Nonetheless, the uncertainty due to the transfer of the surface reflectance data from OLCI-FLEX to OLCI-A bands was up to 0.5 %. For the high resolution instrument FLORIS, the surface reflectance information can be convolved with OLCI's spectral response function. The difference between convolved and true OLCI spectrum is smaller than 0.3 %. The effect on the TOA radiance of this difference will be even smaller.

Furthermore, it was shown that the optimization of the surface reflectance from OLCI-FLEX worked well when all other atmospheric parameters were chosen correctly. If the aerosol type or the AOD was assumed incorrectly, the resulting surface reflectance was also fundamentally wrong with errors between 40 and 80 % for optical thick aerosol layers. In combination with the wrong aerosol assumptions, the found description of the environment resulted in a TOA radiance which reproduced the measured TOA radiance with an uncertainty of up to 1.2 %. The maximum uncertainty was found at 665 nm. Here, the lack of information due to the band distribution induced the large uncertainty. At the other bands, the uncertainty was small. The inaccurate description of aerosol and surface influenced the O_2A absorption band with uncertainties of up to 0.5 % in the TOA radiance.

Overall, the uncertainty analysis for the method showed no systematic biases. The studied uncertainties do neither explain the systematic bias of 2 % between OLCI-A and OLCI-FLEX at wavelengths between 500 and 700 nm nor the difference of 5 % at the longer wavelengths. Hence, the comparison of the TOA with sensors with two different spectral settings is only slightly effected by an inaccurate description of the surface and the aerosol as long the combination reproduces the high resolution TOA radiance. In contrast, an uncertainty of the central wavelength of +/-0.1 nm results in TOA radiance differences of up to 5 %. Thus, a large effort must be put into the accurate description of the band characteristics.

It was shown that a perfect aerosol characterization is not essential for the success of the transfer function. Thus, the transfer function can be applied even for bright surface types like land surfaces for which the estimation of the aerosol type from OLCI is very challenging [Chen et al., 2022].

How does spatial resolution and geolocation mismatch compromise the comparison of ground truth and satellite surface reflectance measurements?

At an exemplary location in central Italy, as presented in Chapter 4, the geolocation mismatch has a large negative effect on the comparability between a ground-based surface reflectance measurement and the satellite surface reflectance. In the studied case, the ground site instrument had a spatial resolution of a few meters and the surface reflectance retrieved from a satellite sensor had a spatial resolution of 300x300 m^2. The relative difference due to geolocation mismatch reached up to 120 %. However, the geolocation mismatch is unavoidable. It is determined by the orbit position and the uncertainty of the geo-coordinates of the satellite sensor. The centre of satellite pixel closest to the ground site can be shifted more than 200 m away from the ground site for a 300x300 m^2 pixel. Furthermore, the geo-coordinates of the satellite pixels from OLCI and FLORIS have an uncertainty of up to 0.5 pixels [Drinkwater and Rebhan, 2007, Drusch, 2018]. The uncertainty due to geolocation mismatch can be only reduced by selecting a homogeneous surface and a ground site which is representative for the surrounding field. The homogeneous area should cover at least 1x1 km^2 (see Figure 4.1). Such area could not be found in our studied case. In our test scene, the largest homogeneous field that fulfilled our requirements of representativeness and of the surface type was too small to minimize the difference due to the geolocation mismatch. In future studies, the requirement of representativeness should be adapted to an area of more than 1x1 km^2.

The difference in surface reflectance due to different spatial resolutions could be minimized by identifying an area that is representative of a satellite pixel. For a 4.5x4.5 m^2 area, the difference due to spatial resolution dissolves in the uncertainty of the TOA radiance from OLCI or FLORIS of 2 %. Thus, the difference cannot be disentangled from the sensor uncertainty.

The surface reflectance changes with the vegetation period and thereby, the representativeness changes. The temporal evolution of the validation uncertainty was studied within a study period of two weeks. The change in the validation uncertainty of a 4.5x4.5 m^2 reference area over time did not originate from changes in the surface cover but originate from different pointing of the sensor during the different overpasses. Hence, the results are not applicable for a true ground site with a fixed position. When studying a reference area of 13.5x13.5 m^2, the difference due to the spatial resolution was small and temporally stable between 720 and 800 nm. Within this spectral range and with this reference area, the chosen ground site could be used for an accurate validation of the surface reflectance retrieved from OLCI or FLORIS. The rest of the spectrum showed differences between the ground measurement and the satellite measurement of up to 8 % in the surface reflectance which translated to a difference in TOA radiance of 5 %.

Only a small fraction of the vegetation period was investigated. When using a suitable ground

site for direct satellite validation, the uncertainty must be verified by regular overpasses with aeroplanes or unmanned aerial vehicles.

Is it possible to estimate the aerosol layer height from OLCI O_2A bands over ocean and how large is the uncertainty?

The TOA radiances at OLCI's O_2A bands are sensitive to the ALH for ocean cases and aerosol layers of dust and smoke. Thus, it is possible to estimate the ALH from the OLCI O_2A bands. An ALH retrieval for scenes with a known aerosol type, either dust or smoke, and a high AOT was developed. The retrieval was applied to two test scenes: a dust scene at the west coast of Africa and a smoke scene at the west coast of America. The uncertainty for the dust case was between 400 and 600 m and for the smoke case, it was approximately 150 m.

The application of the retrieval to the two test scenes resulted in lower ALH compared to results from an active instrument which is commonly handled as truth. However, measurements from the passive instrument TROPOMI showed lower ALH even though the instrument has a higher spectral resolution and thus, higher information contents. Overall, the ALH from OLCI showed good agreement with TROPOMI ALH. This comparison indicates a good performance of the temporal evolution model of the band characterization and the harmonization of the central wavelengths to one common wavelength for each band applied to OLCI.

Studies from TROPOMI showed that the sensitivity to ALH could be even increased when considering also the O_2B band [Chen et al., 2021]. However, the spectral bands of OLCI do not cover the O_2B band. In contrast, FLORIS will cover both oxygen absorption bands with a very high spectral resolution. Thus, FLORIS will be very suitable for an ALH retrieval. The tandem mission of FLEX and Sentinel-3 would then allow a direct comparison of the ALH from OLCI and from FLORIS. Hence, the ALH from OLCI can be validated during the life time of FLEX. Compared to FLEX, Sentinel-3 has a long life time and a global coverage. A validated time series of ALH data from OLCI would be valuable for the Sentinel-3 atmospheric service CAMS, for climate models and for aerosol transport models. For an operational ALH product, an automated classification of the aerosol type and a description of land surface are necessary. Furthermore, the ALH can only be estimated for thick aerosol layers.

Summarizing all lessons learned from the presented studies, I can give the following recommendations for the validation strategy of the products from the FLEX mission:

Recommendations for validation strategy

- The advantages of S3/FLEX tandem mission should be used for solid, global and continuous satellite-satellite validation of L1 data from FLORIS.

- A transfer function should be applied to overcome differences in the spectral response of OLCI and FLORIS within the O_2A band and to reduce differences in observation geometries depending of the chosen orbit.

- A large number of simultaneous measurements are needed for a significant statistical evaluation which is necessary to reduce the uncertainty of geolocation mismatch.

- The temporal evolution of OLCI's spectral characteristics must be considered in all validation activities especially when evaluating the O_2A band.

- Within the transfer function for the TOA radiance, the accuracy of the aerosol description is less important as long as it is consistent with used surface description.

- For an accurate surface reflectance retrieval, as it is the goal of the FLEX mission, an accurate description of the aerosol type is of utmost importance.

- Both the spatial heterogeneity and the geolocation mismatch have strong impact on comparability between ground-based and satellite based measurements. Their effect on the representativeness of ground-based measurements must be quantified.

- The chosen ground site must be surrounded by a homogeneous area of more than 1x1 km^2 to minimize both, the effect of the spatial mismatch and the uncertainty of the geolocation of the satellite pixels.

- Our identified site is suitable for validation purposes at wavelengths between 720 and 800 nm if regular aeroplane overpasses confirm the quantified uncertainty of the validation due to differences in spatial resolution and the geolocation mismatch.

Bibliography

ACRI-ST. Preprocessing required to generate IPF compatible data from S09/S08 OLCI acquisitions: delivery content and Level 0 to Level 1 processing guidelines. Technical report, MPC, 2019. Reference: S3MPC.ACR.MEM.064.

G. P. Anderson, S. A. Clough, F. X. Kneizys, J. H. Chetwynd, and E. P. Shettle. AFGL Atmospheric Constituent Profiles (0.120km). Technical Report AFGL-TR-86-0110, AIR FORCE GEOPHYSICS LAB HANSCOM AFB MA, 1986. URL `https://apps.dtic.mil/docs/citations/ADA175173`. Latest access: 2022-09-05.

K. Anderson, B. Ryan, W. Sonntag, A. Kavvada, and L. Friedl. Earth observation in service of the 2030 agenda for sustainable development. *Geo-spatial Information Science*, 20(2):77–96, 2017. URL `https://doi.org/10.1080/10095020.2017.1333230`.

A. Angal, X. Xiong, K. Thome, and B. N. Wenny. Cross-Calibration of Terra and Aqua MODIS Using RadCalNet. *IEEE Geoscience and Remote Sensing Letters*, 18(2):188–192, 2021. ISSN 1545-598X, 1558-0571. doi: 10.1109/LGRS.2020.2973535. URL `https://ieeexplore.ieee.org/document/9013044/`.

A. Ač, Z. Malenovský, J. Olejníčková, A. Gallé, U. Rascher, and G. Mohammed. Meta-analysis assessing potential of steady-state chlorophyll fluorescence for remote sensing detection of plant water, temperature and nitrogen stress. *Remote Sensing of Environment*, 168:420–436, 2015. ISSN 0034-4257. URL `https://doi.org/10.1016/j.rse.2015.07.022`.

A. Baldridge, S. Hook, C. Grove, and G. Rivera. The ASTER spectral library version 2.0. *Remote Sensing of Environment*, 113(4):711–715, 2009. ISSN 00344257. doi: 10.1016/j.rse.2008.11.007. URL `https://linkinghub.elsevier.com/retrieve/pii/S0034425708003441`.

J. L. Bentley. Multidimensional binary search trees used for associative searching. *Communications of the ACM*, 18(9):509–517, 1975.

L. Bourg. OLCI Level 1 Algorithm Theoretical Basis Document. Technical report, ACRI, Dec 2014.

B. Buman, A. Hueni, R. Colombo, S. Cogliati, M. Celesti, T. Julitta, A. Burkart, B. Siegmann, U. Rascher, M. Drusch, and A. Damm. Towards consistent assessments of in situ radiometric

measurements for the validation of fluorescence satellite missions. *Remote Sensing of Environment*, 274:112984, Jun 2022. ISSN 0034-4257. doi: 10.1016/j.rse.2022.112984. URL `https://www.sciencedirect.com/science/article/pii/S0034425722000980`.

K. Calvin, D. Dasgupta, G. Krinner, A. Mukherji, P. W. Thorne, C. Trisos, J. Romero, P. Al-dunce, K. Barrett, G. Blanco, W. W. Cheung, S. Connors, F. Denton, A. Diongue-Niang, D. Dodman, M. Garschagen, O. Geden, B. Hayward, C. Jones, F. Jotzo, T. Krug, R. Lasco, Y.-Y. Lee, V. Masson-Delmotte, M. Meinshausen, K. Mintenbeck, A. Mokssit, F. E. Otto, M. Pathak, A. Pirani, E. Poloczanska, H.-O. Pörtner, A. Revi, D. C. Roberts, J. Roy, A. C. Ruane, J. Skea, P. R. Shukla, R. Slade, A. Slangen, Y. Sokona, A. A. Sörensson, M. Tignor, D. Van Vuuren, Y.-M. Wei, H. Winkler, P. Zhai, Z. Zommers, J.-C. Hourcade, F. X. Johnson, S. Pachauri, N. P. Simpson, C. Singh, A. Thomas, E. Totin, P. Arias, M. Bustamante, I. Elgizouli, G. Flato, M. Howden, C. Méndez-Vallejo, J. J. Pereira, R. Pichs-Madruga, S. K. Rose, Y. Saheb, R. Sánchez Rodríguez, D. Ürge Vorsatz, C. Xiao, N. Yassaa, A. Alegría, K. Armour, B. Bednar-Friedl, K. Blok, G. Cissé, F. Dentener, S. Eriksen, E. Fischer, G. Garner, C. Guivarch, M. Haasnoot, G. Hansen, M. Hauser, E. Hawkins, T. Hermans, R. Kopp, N. Leprince-Ringuet, J. Lewis, D. Ley, C. Ludden, L. Niamir, Z. Nicholls, S. Some, S. Szopa, B. Trewin, K.-I. Van Der Wijst, G. Winter, M. Witting, A. Birt, M. Ha, J. Romero, J. Kim, E. F. Haites, Y. Jung, R. Stavins, A. Birt, M. Ha, D. J. A. Orendain, L. Ignon, S. Park, Y. Park, A. Reisinger, D. Cammarano, A. Fischlin, J. S. Fuglestvedt, G. Hansen, C. Ludden, V. Masson-Delmotte, J. R. Matthews, K. Mintenbeck, A. Pirani, E. Poloczanska, N. Leprince-Ringuet, and C. Péan. IPCC, 2023: Climate Change 2023: Synthesis Report. Contribution of Working Groups I, II and III to the Sixth Assessment Report of the Intergovernmental Panel on Climate Change [Core Writing Team, H. Lee and J. Romero (eds.)]. IPCC, Geneva, Switzerland. Technical report, Intergovernmental Panel on Climate Change (IPCC), July 2023. URL `https://www.ipcc.ch/report/ar6/syr/`. Edition: First.

P. K. E. Campbell, E. M. Middleton, L. A. Corp, and M.-S. Kim. Contribution of chlorophyll fluorescence to the apparent vegetation reflectance. *Science of The Total Environment*, 404(2): 433–439, 2008. ISSN 0048-9697. URL `https://doi.org/10.1016/j.scitotenv.2007.11.004`.

G. Chander, T. J. Hewison, N. Fox, X. Wu, X. Xiong, and W. J. Blackwell. Overview of Inter-calibration of Satellite Instruments. *IEEE Transactions on Geoscience and Remote Sensing*, 51(3):1056–1080, 2013a. ISSN 1558-0644. doi: 10.1109/TGRS.2012.2228654.

G. Chander, N. Mishra, D. L. Helder, D. B. Aaron, A. Angal, T. Choi, X. Xiong, and D. R. Doelling. Applications of Spectral Band Adjustment Factors (SBAF) for Cross-Calibration. *IEEE Transactions on Geoscience and Remote Sensing*, 51(3):1267–1281, 2013b. ISSN 1558-0644. doi: 10.1109/TGRS.2012.2228007.

C. Chen, O. Dubovik, P. Litvinov, D. Fuertes, A. Lopatin, T. Lapyonok, C. Matar, Y. Karol, J. Fischer, R. Preusker, A. Hangler, M. Aspetsberger, L. Bindreiter, D. Marth, J. Chimot, B. Fougnie, T. Marbach, and B. Bojkov. Properties of aerosol and surface derived

from OLCI/Sentinel-3A using GRASP approach: Retrieval development and preliminary validation. *Remote Sensing of Environment*, 280:113142, 2022. ISSN 00344257. doi: 10.1016/j.rse.2022.113142. URL `https://linkinghub.elsevier.com/retrieve/pii/ S0034425722002565`.

X. Chen, J. Wang, X. Xu, M. Zhou, H. Zhang, L. Castro Garcia, P. R. Colarco, S. J. Janz, J. Yorks, M. McGill, J. S. Reid, M. de Graaf, and S. Kondragunta. First retrieval of absorbing aerosol height over dark target using TROPOMI oxygen B band: Algorithm development and application for surface particulate matter estimates. *Remote Sensing of Environment*, 265:112674, Nov 2021. ISSN 00344257. doi: 10.1016/j.rse.2021.112674. URL `https: //linkinghub.elsevier.com/retrieve/pii/S0034425721003941`.

J. Chimot, J. P. Veefkind, T. Vlemmix, J. F. de Haan, V. Amiridis, E. Proestakis, E. Marinou, and P. F. Levelt. An exploratory study on the aerosol height retrieval from omi measurements of the 477 nm o2-o2 spectral band using a neural network approach. *Atmospheric Measurement Techniques*, 10(3):783–809, Mar 2017. ISSN 1867-1381. doi: 10.5194/amt-10-783-2017. URL `https://amt.copernicus.org/articles/10/783/2017/`.

J. Chimot, J. P. Veefkind, J. F. de Haan, P. Stammes, and P. F. Levelt. Minimizing aerosol effects on the omi tropospheric no 2 retrieval–an improved use of the 477 nm o 2-o 2 band and an estimation of the aerosol correction uncertainty. *Atmospheric Measurement Techniques*, 12 (1):491–516, 2019.

R. N. Clark, G. A. Swayze, R. A. Wise, K. E. Livo, T. M. Hoefen, R. F. Kokaly, and S. J. Sutley. USGS digital spectral library splib06a. Technical report, US Geological Survey, 2007.

S. Clerc, C. Donlon, F. Borde, N. Lamquin, S. E. Hunt, D. Smith, M. McMillan, J. Mittaz, E. Woolliams, M. Hammond, C. Banks, C. Moreau, B. Picard, M. Raynal, P. Rieu, and A. Guérou. Benefits and lessons learned from the sentinel-3 tandem phase. *Remote Sensing*, 12(17):2668, 2020.

CMEMS. About - copernicus marine service, 2021. URL `https://marine.copernicus.eu/ about`. Latest access: 27/10/2023.

S. Cogliati, W. Verhoef, S. Kraft, N. Sabater, L. Alonso, J. Vicent, J. Moreno, M. Drusch, and R. Colombo. Retrieval of sun-induced fluorescence using advanced spectral fitting methods. *Remote Sensing of Environment*, 169:344–357, 2015. ISSN 0034-4257. URL `https://doi. org/10.1016/j.rse.2015.08.022`.

S. Cogliati, M. Celesti, I. Cesana, F. Miglietta, L. Genesio, T. Julitta, D. Schuettemeyer, M. Drusch, U. Rascher, P. Jurado, and R. Colombo. A Spectral Fitting Algorithm to Retrieve the Fluorescence Spectrum from Canopy Radiance. *Remote Sensing*, 11(16):1840, 2019. ISSN 2072-4292. doi: 10.3390/rs11161840. URL `https://www.mdpi.com/2072-4292/11/16/ 1840`.

S. F. Colosimo, V. Natraj, S. P. Sander, and J. Stutz. A sensitivity study on the retrieval of aerosol vertical profiles using the oxygen A-band. *Atmospheric Measurement Techniques*, 9(4):1889–1905, 2016. ISSN 1867-8548. doi: 10.5194/amt-9-1889-2016. URL `https://amt.copernicus.org/articles/9/1889/2016/`.

Copernicus. Copernicus climate change service, 2021a. URL `https://www.copernicus.eu/en/copernicus-services/climate-change`. Latest access: 27/10/2023.

Copernicus. Copernicus emergency service, 2021b. URL `https://www.copernicus.eu/en/copernicus-services/emergency`. Latest access: 27/10/2023.

Copernicus. Copernicus security service, 2021c. URL `https://www.copernicus.eu/en/copernicus-services/security`. Latest access: 27/10/2023.

Copernicus. Copernicus: Europe's eyes on earth, 2023a. URL `https://www.copernicus.eu/sites/default/files/2023-07/Copernicus%20General%20EN.pdf`. Latest access: 27/10/2023.

Copernicus. Record-breaking north atlantic ocean temperatures contribute to extreme marine heatwaves, 2023b. https://climate.copernicus.eu/record-breaking-north-atlantic-ocean-temperatures-contribute-extreme-marine-heatwaves; Latest access: 02/08/2023.

P. Coppo, A. Taiti, L. Pettinato, M. Francois, M. Taccola, and M. Drusch. Fluorescence Imaging Spectrometer (FLORIS) for ESA FLEX Mission. *Remote Sensing*, 9(7):649, 2017. ISSN 2072-4292. doi: 10.3390/rs9070649. URL `http://www.mdpi.com/2072-4292/9/7/649`.

C. Cox and W. Munk. Measurement of the roughness of the sea surface from photographs of the sun's glitter. *Journal of the Optical Society of America*, 44(11):838–850, 1954.

C. De Grave, L. Pipia, B. Siegmann, P. Morcillo-Pallarés, J. P. Rivera-Caicedo, J. Moreno, and J. Verrelst. Retrieving and Validating Leaf and Canopy Chlorophyll Content at Moderate Resolution: A Multiscale Analysis with the Sentinel-3 OLCI Sensor. *Remote Sensing*, 13(8):1419, Apr 2021. ISSN 2072-4292. doi: 10.3390/rs13081419. URL `https://www.mdpi.com/2072-4292/13/8/1419`.

C. Donlon, B. Berruti, A. Buongiorno, M.-H. Ferreira, P. Féménias, J. Frerick, P. Goryl, U. Klein, H. Laur, C. Mavrocordatos, J. Nieke, B. Seitz, J. Stroede, and R. Sciarra. The global monitoring for environment and security (GMES) sentinel-3 mission. *Remote Sensing of Environment*, 120:37–57, 2012.

L. Doppler, C. Carbajal-Henken, J. Pelon, F. Ravetta, and J. Fischer. Extension of radiative transfer code MOMO, matrix-operator model to the thermal infrared – Clear air validation by comparison to RTTOV and application to CALIPSO-IIR. *Journal of Quantitative Spectroscopy and Radiative Transfer*, 144:49–67, 2014a. ISSN 00224073. doi: 10.1016/j.jqsrt.2014.03.028. URL `https://linkinghub.elsevier.com/retrieve/pii/S0022407314001447`.

L. Doppler, R. Preusker, R. Bennartz, and J. Fischer. k-bin and k-IR: k-distribution methods without correlation approximation for non-fixed instrument response function and extension to the thermal infrared—Applications to satellite remote sensing. *Journal of Quantitative Spectroscopy and Radiative Transfer*, 133:382–395, 2014b. ISSN 0022-4073. doi: 10.1016/j.jqsrt.2013.09.001. URL http://www.sciencedirect.com/science/article/pii/S0022407313003567.

R. Dragani, S. Abdalla, R. Engelen, A. Inness, and J.-N. Thépaut. Ten years of envisat observations at ecmwf: a review of activities and lessons learnt. *Quarterly Journal of the Royal Meteorological Society*, 141(687):598–610, 2015.

M. R. Drinkwater and H. Rebhan. Sentinel-3: Mission Requirements Document, Feb 2007. URL https://earth.esa.int/eogateway/documents/20142/1564943/Sentinel-3-Mission-Requirements-Document-MRD.pdf. Reference: EOP-SMO/1151/MD-md.

B. J. Drouin, D. C. Benner, L. R. Brown, M. J. Cich, T. J. Crawford, V. M. Devi, A. Guillaume, J. T. Hodges, E. J. Mlawer, F. Robichaud, David J.and Oyafusoa, K. Paynea, Vivienne H.and Sunga, and S. Wishnowf, Edward H.and Yua. Multispectrum analysis of the oxygen A-band. *Journal of Quantitative Spectroscopy and Radiative Transfer*, 186:118–138, 2017. Publisher: Elsevier.

M. Drusch. FLEX Earth Explorer 8 Mission Requirements Document, Jun 2018. URL https://download.esa.int/docs/FLEX/FLEX_MRD_v3.0_20180605_issued.pdf. Reference: ESAEOP-SM/2221/MDru-md.

M. Drusch, J. Moreno, U. Del Bello, R. Franco, Y. Goulas, A. Huth, S. Kraft, E. M. Middleton, F. Miglietta, G. Mohammed, L. Nedbal, U. Rascher, D. Schüttemeyer, and W. Verhoef. The FLuorescence EXplorer Mission Concept—ESA's Earth Explorer 8. *IEEE Transactions on Geoscience and Remote Sensing*, 55(3):1273–1284, 2017. ISSN 0196-2892, 1558-0644. doi: 10.1109/TGRS.2016.2621820. URL http://ieeexplore.ieee.org/document/7795187/.

S. Du, X. Liu, J. Chen, W. Duan, and L. Liu. Addressing validation challenges for tropomi solar-induced chlorophyll fluorescence products using tower-based measurements and an nirv-scaled approach. *Remote Sensing of Environment*, 290:113547, 2023. ISSN 0034-4257. URL https://doi.org/10.1016/j.rse.2023.113547.

O. Dubovik, A. Sinyuk, T. Lapyonok, B. N. Holben, M. Mishchenko, P. Yang, T. F. Eck, H. Volten, O. Muñoz, B. Veihelmann, W. J. van der Zande, J.-F. Leon, M. Sorokin, and I. Slutsker. Application of spheroid models to account for aerosol particle nonsphericity in remote sensing of desert dust. *Journal of Geophysical Research: Atmospheres*, 111(D11), 2006. URL https://doi.org/10.1029/2005JD006619.

P. Dubuisson, R. Frouin, D. Dessailly, L. Duforêt, J.-F. Léon, K. Voss, and D. Antoine. Estimating the altitude of aerosol plumes over the ocean from reflectance ratio measurements in the O2 A-band. *Remote Sensing of Environment*, 113(9):1899–1911, September 2009. ISSN 00344257. doi: 10.1016/j.rse.2009.04.018. URL `https://linkinghub.elsevier.com/retrieve/pii/S0034425709001333`.

L. Duforêt, R. Frouin, and P. Dubuisson. Importance and estimation of aerosol vertical structure in satellite ocean-color remote sensing. *Applied optics*, 46(7):1107–1119, 2007.

Earthdata NASA. What is remote sensing?, Aug 2019. URL `https://www.earthdata.nasa.gov/learn/backgrounders/remote-sensing`. Latest access: 20/11/2023.

ECMWF. Copernicus atmosphere monitoring service, 2021. URL `https://atmosphere.copernicus.eu/`. Latest access: 27/10/2023.

D. Efremenko and A. Kokhanovsky. Introduction to Remote Sensing. In *Foundations of Atmospheric Remote Sensing*, pages 1–35. Springer Cham, 2021. ISBN 978-3-030-66744-3 978-3-030-66745-0. URL `https://link.springer.com/10.1007/978-3-030-66745-0_1`.

ESA. Earth observation science strategy for esa: a new era for scientific advances and societal benefits. *Earth Observation Science Strategy*, SP-1329/1, 2015. (2 volumes). European Space Agency, Noordwijk, the Netherlands.

ESA. Olci instrument calibration, 2016. URL `https://sentinels.copernicus.eu/web/sentinel/technical-guides/sentinel-3-olci/olci-instrument/calibration`. Latest access: 01/11/2023.

ESA. Technical Note: Sentinel-3 OLCI-A spectral response functions, Reference: S3-TN-ESA-OL-660. Technical Report 2, European Space Agency, 2016.

ESA. Soyflex 2015, 2020a. URL `https://doi.org/10.5270/ESA-50a3dd4`. Latest access: 27/10/2023.

ESA. Flex, 2020b. URL `https://earth.esa.int/eogateway/missions/flex`. Latest access: 27/09/2023.

ESA. Copernicus land monitoring service, 2021a. URL `https://land.copernicus.eu/en`. Latest access: 27/10/2023.

ESA. Sentinel-3 OLCI Tandem 2018, 2021b. URL `https://doi.org/10.5270/ESA-624426c`. Latest access: 09/01/2024.

ESA. Earth explorers, 2023a. URL `https://earth.esa.int/eogateway/missions/earth-explorers`. Latest access: 27/09/2023.

ESA. Esa-developed earth observation missions, 2023b. URL `https://www.esa.int/Applications/Observing_the_Earth/Earth_observing_missions`. Latest access 21/11/2023.

ESA. Sentinel overview, 2023c. URL `https://sentinels.copernicus.eu/web/sentinel/missions`. Latest access: 27/10/2023.

ESA. Flexsense 2018, 2024. URL `https://doi.org/10.57780/esa-ae7953d`. Latest access 24/01/2024.

ESA and P. Carril. Sentinel-3 satellite in space, 2023. URL `https://www.dlr.de/en/images/2020/3/copernicus-sentinel-3-in-space-artists-impression`. Latest access: 27/10/2023.

F. Fell and J. Fischer. Numerical simulation of the light field in the atmosphere–ocean system using the matrix-operator method. *Journal of Quantitative Spectroscopy and Radiative Transfer*, 69(3):351–388, 2001.

C. Fernández. Sentinel-3 kml orbit files. Technical report, GMV, 2016. URL `https://sentinels.copernicus.eu/documents/247904/685098/S3-relative-ground-track-file-transfer-document.pdf`. Latest access 08/01/2024.

J. Fischer and H. Grassl. Radiative transfer in an atmosphere–ocean system: an azimuthally dependent matrix-operator approach. *Applied Optics*, 23(7):1032–1039, 1984.

C. Frankenberg, A. Butz, and G. C. Toon. Disentangling chlorophyll fluorescence from atmospheric scattering effects in O2 A-band spectra of reflected sun-light. *Geophysical Research Letters*, 38(3), 2011. ISSN 1944-8007. doi: 10.1029/2010GL045896. URL `https://agupubs.onlinelibrary.wiley.com/doi/abs/10.1029/2010GL045896`.

H. Gao, Q. Wang, X. Gu, J. Yang, Q. Liu, Z. Tao, X. Qiu, W. Zhang, X. Shi, and X. Zhao. Study on Surface Reflectance Sampling Method and Uncertainty Based on Airborne Hyperspectral Images. *Remote Sensing*, 15(21):5090, Oct 2023. ISSN 2072-4292. doi: 10.3390/rs15215090. URL `https://www.mdpi.com/2072-4292/15/21/5090`.

D. M. Giles, A. Sinyuk, M. G. Sorokin, J. S. Schafer, A. Smirnov, I. Slutsker, T. F. Eck, B. N. Holben, J. R. Lewis, J. R. Campbell, E. J. Welton, S. V. Korkin, and A. I. Lyapustin. Advancements in the aerosol robotic network (aeronet) version 3 database – automated near-real-time quality control algorithm with improved cloud screening for sun photometer aerosol optical depth (aod) measurements. *Atmospheric Measurement Techniques*, 12(1):169–209, 2019. doi: 10.5194/amt-12-169-2019. URL `https://amt.copernicus.org/articles/12/169/2019/`.

M. Goldberg, G. Ohring, J. Butler, C. Cao, R. Datla, D. Doelling, V. Gärtner, T. Hewison, B. Iacovazzi, D. Kim, T. Kurino, J. Lafeuille, P. Minnis, D. Renaut, J. Schmetz, D. Tobin, L. Wang, F. Weng, X. Wu, F. Yu, P. Zhang, and T. Zhu. The Global Space-Based Inter-Calibration System. *Bulletin of the American Meteorological Society*, 92:467–475, 2011.

I. Gordon, L. Rothman, C. Hill, R. Kochanov, Y. Tan, P. Bernath, M. Birk, V. Boudon, A. Campargue, K. Chance, B. Drouin, J.-M. Flaud, R. Gamache, J. Hodges, D. Jacquemart, V. Perevalov, A. Perrin, K. Shine, M.-A. Smith, J. Tennyson, G. Toon, H. Tran, V. Tyuterev, A. Barbe, A. Császár, V. Devi, T. Furtenbacher, J. Harrison, J.-M. Hartmann, A. Jolly, T. Johnson, T. Karman, I. Kleiner, A. Kyuberis, J. Loos, O. Lyulin, S. Massie, S. Mikhailenko, N. Moazzen-Ahmadi, H. Müller, O. Naumenko, A. Nikitin, O. Polyansky, M. Rey, M. Rotger, S. Sharpe, K. Sung, E. Starikova, S. Tashkun, J. V. Auwera, G. Wagner, J. Wilzewski, P. Wcisło, S. Yu, and E. Zak. The HITRAN2016 molecular spectroscopic database. *Journal of Quantitative Spectroscopy and Radiative Transfer*, 203:3–69, 2017. ISSN 00224073. doi: 10.1016/j.jqsrt.2017.06.038. URL https://linkinghub.elsevier.com/retrieve/pii/S0022407317301073.

D. Griffin, C. Sioris, J. Chen, N. Dickson, A. Kovachik, M. de Graaf, S. Nanda, P. Veefkind, E. Dammers, C. A. McLinden, P. Makar, and A. Akingunola. The 2018 fire season in north america as seen by tropomi: aerosol layer height intercomparisons and evaluation of model-derived plume heights. *Atmospheric Measurement Techniques*, 13(3):1427–1445, 2020. doi: 10.5194/amt-13-1427-2020. URL https://amt.copernicus.org/articles/13/1427/2020/.

S. Guerlet, A. Butz, D. Schepers, S. Basu, O. Hasekamp, A. Kuze, T. Yokota, J.-F. Blavier, N. Deutscher, D. T. Griffith, F. Hase, E. Kyro, I. Morino, V. Sherlock, R. Sussmann, A. Galli, and I. Aben. Impact of aerosol and thin cirrus on retrieving and validating xco2 from gosat shortwave infrared measurements. *Journal of Geophysical Research: Atmospheres*, 118(10):4887–4905, 2013.

M. Hess, P. Koepke, and I. Schult. Optical properties of aerosols and clouds: The software package OPAC. *Bulletin of the American meteorological society*, 79(5):831–844, 1998.

T. J. Hewison, D. R. Doelling, C. Lukashin, D. Tobin, V. O. John, S. Joro, and B. Bojkov. Extending the Global Space-Based Inter-Calibration System (GSICS) to Tie Satellite Radiances to an Absolute Scale. *Remote Sensing*, 12(11):1782, 2020. ISSN 2072-4292. doi: 10.3390/rs12111782. URL https://www.mdpi.com/2072-4292/12/11/1782.

A. Hollstein and J. Fischer. Radiative transfer solutions for coupled atmosphere ocean systems using the matrix operator technique. *Journal of Quantitative Spectroscopy and Radiative Transfer*, 113(7):536–548, 2012. ISSN 0022-4073. doi: 10.1016/j.jqsrt.2012.01.010. URL http://www.sciencedirect.com/science/article/pii/S002240731200026X.

A. Hollstein and J. Fischer. Retrieving aerosol height from the oxygen A band: a fast forward operator and sensitivity study concerning spectral resolution, instrumental noise, and surface inhomogeneity. *Atmospheric Measurement Techniques*, 7(5):1429–1441, 2014. ISSN 1867-8548. doi: 10.5194/amt-7-1429-2014. URL https://amt.copernicus.org/articles/7/1429/2014/.

S. Houweling, W. Hartmann, I. Aben, H. Schrijver, J. Skidmore, G.-J. Roelofs, and F.-M. Breon. Evidence of systematic errors in sciamachy-observed co 2 due to aerosols. *Atmospheric Chemistry and Physics*, 5(11):3003–3013, 2005.

H. C. Hulst. *A new look at multiple scattering*. NASA Institute for Space Studies, Goddard Space Flight Center, 1963.

L. K. Jänicke, R. Preusker, M. Celesti, M. Tudoroiu, J. Fischer, D. Schüttemeyer, and M. Drusch. OLCI-A/B tandem phase: evaluation of fluorescence explorer (FLEX)-like radiances and estimation of systematic differences between OLCI-A and OLCI-FLEX. *Atmospheric Measurement Techniques*, 16(12):3101–3121, 2023. URL `https://doi.org/10.5194/amt-16-3101-2023`.

JB Hyperspectral Devices GmBH. Fluorescence box, 2023. URL `https://www.jb-hyperspectral.com/products/flox/`. Latest acess 07/12/2023.

S. Jutz and M. P. Milagro-Pérez. Copernicus: the european earth observation programme. *Revista de Teledetección*, -:5–11, 11 2020. doi: 10.4995/raet.2020.14346.

S. M. Kim and R. Mendelsohn. Climate change to increase crop failure in u.s. *Environmental Research Letters*, 18(1):014014, 2023. URL `https://dx.doi.org/10.1088/1748-9326/acac41`.

Z. Kipling, P. Stier, C. E. Johnson, G. W. Mann, N. Bellouin, S. E. Bauer, T. Bergman, M. Chin, T. Diehl, S. J. Ghan, T. Iversen, A. Kirkevag, H. Kokkola, X. Liu, G. Luo, T. van Noije, K. J. Pringle, K. von Salzen, M. Schulz, O. Seland, R. B. Skeie, T. Takemura, K. Tsigaridis, and K. Zhang. What controls the vertical distribution of aerosol? Relationships between process sensitivity in HadGEM3–UKCA and inter-model variation from AeroCom Phase II. *Atmospheric Chemistry and Physics*, 16(4):2221–2241, February 2016. ISSN 1680-7324. doi: 10.5194/acp-16-2221-2016. URL `https://acp.copernicus.org/articles/16/2221/2016/`.

B. Koffi, M. Schulz, F.-M. Bréon, J. Griesfeller, D. Winker, Y. Balkanski, S. Bauer, T. Berntsen, M. Chin, W. D. Collins, F. Dentener, T. Diehl, R. Easter, S. Ghan, P. Ginoux, S. Gong, L. W. Horowitz, T. Iversen, A. Kirkevåg, D. Koch, M. Krol, G. Myhre, P. Stier, and T. Takemura. Application of the caliop layer product to evaluate the vertical distribution of aerosols estimated by global models: Aerocom phase i results. *Journal of Geophysical Research: Atmospheres*, 117(D10), 2012. URL `https://doi.org/10.1029/2011JD016858`.

A. A. Kokhanovsky and G. Leeuw. *Satellite aerosol remote sensing over land*, volume 1. Springer, 2009.

A. A. Kokhanovsky and V. V. Rozanov. The determination of dust cloud altitudes from a satellite using hyperspectral measurements in the gaseous absorption band. *International Journal of Remote Sensing*, 31(10):2729–2744, 2010. URL `https://doi.org/10.1080/01431160903085644`.

S. Kraft, U. Del Bello, M. Bouvet, M. Drusch, and J. Moreno. FLEX: ESA's Earth Explorer 8 candidate mission. In *2012 IEEE International Geoscience and Remote Sensing Symposium*, pages 7125–7128, Munich, Germany, 2012. IEEE. ISBN 978-1-4673-1159-5 978-1-4673-1160-1 978-1-4673-1158-8. doi: 10.1109/IGARSS.2012.6352020. URL `http://ieeexplore.ieee.org/document/6352020/`.

A. Kylling, S. Vandenbussche, V. Capelle, J. Cuesta, L. Klüser, L. Lelli, T. Popp, K. Stebel, and P. Veefkind. Comparison of dust-layer heights from active and passive satellite sensors. *Atmospheric Measurement Techniques*, 11(5):2911–2936, 2018.

A. M. Laine, L. Mehtätalo, A. Tolvanen, S. Frolking, and E.-S. Tuittila. Impacts of drainage, restoration and warming on boreal wetland greenhouse gas fluxes. *Science of The Total Environment*, 647:169–181, 2019. ISSN 0048-9697. URL `https://doi.org/10.1016/j.scitotenv.2018.07.390`.

W. F. Lamb, T. Wiedmann, J. Pongratz, R. Andrew, M. Crippa, J. G. Olivier, D. Wiedenhofer, G. Mattioli, A. Al Khourdajie, J. House, S. Pachauri, M. Figueroa, Y. Saheb, R. Slade, K. Hubacek, L. Sun, S. Kahn Ribeiro, S. Khennas, S. de la Rue du Can, L. Chapungu, S. J. Davis, I. Bashmakov, H. Dai, S. Dhakal, X. Tan, Y. Geng, B. Gu, and J. Minx. A review of trends and drivers of greenhouse gas emissions by sector from 1990 to 2018. *Environmental research letters*, 16(7):073005, 2021.

N. Lamquin, S. Clerc, L. Bourg, and C. Donlon. Olci a/b tandem phase analysis, part 1: Level 1 homogenisation and harmonisation. *Remote Sensing*, 12(11):1804, 2020.

C. Le Quéré, M. R. Raupach, J. G. Canadell, G. Marland, L. Bopp, P. Ciais, T. J. Conway, S. C. Doney, R. A. Feely, P. Foster, et al. Trends in the sources and sinks of carbon dioxide. *Nature Geoscience*, 2(12):831–836, 2009. URL `https://doi.org/10.1038/ngeo689`.

C. Li, J. Li, O. Dubovik, Z.-C. Zeng, and Y. L. Yung. Impact of aerosol vertical distribution on aerosol optical depth retrieval from passive satellite sensors. *Remote Sensing*, 12(9):1524, 2020. ISSN 2072-4292. doi: 10.3390/rs12091524. URL `https://www.mdpi.com/2072-4292/12/9/1524`.

K.-N. Liou. *An introduction to atmospheric radiation*, volume 84. Elsevier, 2002.

E. J. McCartney. Optics of the atmosphere: scattering by molecules and particles. *New York*, 1: 408, 1976.

W. P. Menzel, R. A. Frey, H. Zhang, D. P. Wylie, C. C. Moeller, R. E. Holz, B. Maddux, B. A. Baum, K. I. Strabala, and L. E. Gumley. Modis global cloud-top pressure and amount estimation: Algorithm description and results. *Journal of Applied Meteorology and Climatology*, 47 (4):1175 – 1198, 2008. URL `https://doi.org/10.1175/2007JAMC1705.1`.

K. Michailidis, M.-E. Koukouli, D. Balis, J. P. Veefkind, M. de Graaf, L. Mona, N. Papagianopoulos, G. Pappalardo, I. Tsikoudi, V. Amiridis, E. Marinou, A. Gialitaki, R.-E. Mamouri, A. Nisantzi, D. Bortoli, M. Costa, V. Salgueiro, A. Papayannis, M. Mylonaki, L. Alados-Arboledas, S. Romano, M. R. Perrone, and H. Baars. Validation of the TROPOMI/S5P aerosol layer height using EARLINET lidars. *Atmospheric Chemistry and Physics*, 23(3):1919–1940, February 2023. ISSN 1680-7324. doi: 10.5194/acp-23-1919-2023. URL `https://acp.copernicus.org/articles/23/1919/2023/`.

J. J. Miranda, I. Scholz, J. Agard, K. Al-Ghanim, S. N. Bobylev, O. P. Dube, I. Hathie, N. Kanie, N. J. Madise, S. Malekpour, J. C. Montoya, J. Pan, P. Asa, A. Sagar, and N. Shackell. Global sustainable development report 2023: Times of crisis, times of change: Science for accelerating transformations to sustainable development. *United Nations*, -:–, 2023.

M. I. Mishchenko and L. D. Travis. T-matrix computations of light scattering by large spheroidal particles. *Opt. Commun.*, 109:16–21, 1994. doi: 10.1016/0030-4018(94)90731-5.

S. Nanda, J. P. Veefkind, M. De Graaf, M. Sneep, P. Stammes, J. F. De Haan, A. F. Sanders, A. Apituley, O. Tuinder, and P. F. Levelt. A weighted least squares approach to retrieve aerosol layer height over bright surfaces applied to gome-2 measurements of the oxygen a band for forest fire cases over europe. *Atmospheric Measurement Techniques*, 11(6):3263–3280, 2018.

S. Nanda, M. de Graaf, J. P. Veefkind, M. ter Linden, M. Sneep, J. de Haan, and P. F. Levelt. A neural network radiative transfer model approach applied to the tropospheric monitoring instrument aerosol height algorithm. *Atmospheric Measurement Techniques*, 12(12):6619–6634, 2019.

S. Nanda, M. de Graaf, J. P. Veefkind, M. Sneep, M. ter Linden, J. Sun, and P. F. Levelt. A first comparison of TROPOMI aerosol layer height (ALH) to CALIOP data. *Atmospheric Measurement Techniques*, 13(6):3043–3059, June 2020. ISSN 1867-8548. doi: 10.5194/amt-13-3043-2020. URL `https://amt.copernicus.org/articles/13/3043/2020/`.

NASA. Space science data coordinated archive - spacecraft query, Oct 2022. URL `https://nssdc.gsfc.nasa.gov/nmc/spacecraft/query`. Latest access: 21/11/2023.

National Oceanic and Atmospheric Administration (NOAA). Carbon cycle, 2019. URL `https://www.noaa.gov/education/resource-collections/climate/carbon-cycle`. Latest access 04/12/2023.

M. Neneman, S. Wagner, L. Bourg, L. Blanot, M. Bouvet, S. Adriaensen, and J. Nieke. Use of moon observations for characterization of sentinel-3b ocean and land color instrument. *Remote Sensing*, 12(16):2543, 2020. ISSN 2072-4292. doi: 10.3390/rs12162543. URL `https://www.mdpi.com/2072-4292/12/16/2543`.

F. Niro, P. Goryl, S. Dransfeld, V. Boccia, F. Gascon, J. Adams, B. Themann, S. Scifoni, and G. Doxani. European Space Agency (ESA) Calibration/Validation Strategy for Optical Land-

Imaging Satellites and Pathway towards Interoperability. *Remote Sensing*, 13(15):3003, 2021. doi: 10.3390/rs13153003. URL `https://www.mdpi.com/2072-4292/13/15/3003`.

D. Nuzzi, L. Pettinato, E. Fossati, R. Gabrieli, P. Coppo, M. Baroni, E. De Luca, L. Giunti, A. Cavanna, J. Romano, G. Postiglione, F. Galeotti, C. Pompei, M. Barilli, M. Barillot, and M. Taccola. Improving stray-light characterization beyond blooming: the experience of the FLORIS Optical Model Refurbished. In K. Minoglou, N. Karafolas, and B. Cugny, editors, *International Conference on Space Optics — ICSO 2022*, page 15, Dubrovnik, Croatia, Jul 2023. SPIE. ISBN 978-1-5106-6803-4 978-1-5106-6804-1. doi: 10.1117/12.2689042. URL `https://www.spiedigitallibrary.org/conference-proceedings-of-spie/12777/2689042/Improving-stray-light-characterization-beyond-blooming--the-experience-of/10.1117/12.2689042.full`.

G. Ohring, B. Wielicki, R. Spencer, B. Emery, and R. Datla. Satellite instrument calibration for measuring global climate change: Report of a workshop. *Bulletin of the American Meteorological Society*, 86(9):1303 – 1314, 2005. URL `https://doi.org/10.1175/BAMS-86-9-1303`.

R. K. Pachauri, M. R. Allen, V. R. Barros, J. Broome, W. Cramer, R. Christ, J. A. Church, L. Clarke, Q. Dahe, P. Dasgupta, et al. *IPPC, 2014: Climate change 2014: synthesis report. Contribution of Working Groups I, II and III to the fifth assessment report of the Intergovernmental Panel on Climate Change*, volume -. Ipcc, 2014. [Core Writing Team, R.K. Pachauri and L.A. Meyer (eds.)]. IPCC, Geneva, Switzerland.

F. Pedregosa, G. Varoquaux, A. Gramfort, V. Michel, B. Thirion, O. Grisel, M. Blondel, P. Prettenhofer, R. Weiss, V. Dubourg, J. Vanderplas, A. Passos, D. Cournapeau, M. Brucher, M. Perrot, and E. Duchesnay. Scikit-learn: Machine learning in Python. *Journal of Machine Learning Research*, 12:2825–2830, 2011.

G. W. Petty. *A first course in atmospheric radiation*, volume -. Sundog Plublishing, Madison, Wisconsin, 2006.

V.-H. Peuch, R. Engelen, M. Rixen, D. Dee, J. Flemming, M. Suttie, M. Ades, A. Agustí-Panareda, C. Ananasso, E. Andersson, D. Armstrong, J. Barré, N. Bousserez, J. J. Dominguez, S. Garrigues, A. Inness, L. Jones, Z. Kipling, J. Letertre-Danczak, M. Parrington, M. Razinger, R. Ribas, S. Vermoote, X. Yang, A. Simmons, J. G. Marcilla, and J.-N. Thépaut. The Copernicus Atmosphere Monitoring Service: From Research to Operations. *Bulletin of the American Meteorological Society*, 103(12):E2650–E2668, Dec 2022. ISSN 0003-0007, 1520-0477. doi: 10.1175/BAMS-D-21-0314.1. URL `https://journals.ametsoc.org/view/journals/bams/103/12/BAMS-D-21-0314.1.xml`.

G. N. Plass, G. W. Kattawar, and F. E. Catchings. Matrix operator theory of radiative transfer. 1: Rayleigh scattering. *Applied Optics*, 12(2):314–329, 1973.

R. W. Preisendorfer. Radiative transfer on discrete spaces. *Oxford, Pergamon Press, LTD.*, 74: 459, 1965.

R. Preusker. Snap data processors - olci o2a harmonisation algorithm specification, 2020. URL `https://seadas.gsfc.nasa.gov/help-8.3.0/harmonisation/OlciO2aHarmonisationAlgorithmSpecification.html`. Latest access: 03/07/2023.

R. Preusker. Sentinel-3 olci temporal model of spectral characteristics, 2021. URL `https://sentinel.esa.int/documents/247904/2700436/S3MPC_OLCI_spectral_characterisation_SD_RP_EUM_SD_v1.1.pdf`. Latest access: 03/07/2023.

R. Preusker and J. Fischer. Study on the cloud top pressure development from sentinel-3 olci octpo2 - algorithm theoretical basis document (atbd). Technical report, EUMETSAT, 2021. URL `https://www-cdn.eumetsat.int/files/2021-09/OCTPO2_ATBD_CTP_v2-2.pdf`. Latest access: 03/07/2023.

R. Preusker and R. Lindstrot. Remote sensing of cloud-top pressure using moderately resolved measurements within the oxygen a band—a sensitivity study. *Journal of applied meteorology and climatology*, 48(8):1562–1574, 2009.

U. Rascher, L. Alonso, A. Burkart, C. Cilia, S. Cogliati, R. Colombo, A. Damm, M. Drusch, L. Guanter, J. Hanus, et al. Sun-induced fluorescence–a new probe of photosynthesis: First maps from the imaging spectrometer hyplant. *Global change biology*, 21(12):4673–4684, 2015.

H. Rebhan, P. Goryl, C. Donlon, P. Féménias, H. Bonekamp, V. Fournier-Sicre, E. Kwiatkowska, F. Montagner, C. Nogueira-Loddo, and A. O'Carroll. Sentinel-3 Calibration and Validation Plan. Technical report, ESA, EUMETSAT, May 2014.

R. Redheffer. On the relation of transmission-line theory to scattering and transfer. *J. Math. Phys.*, 41:1–41, 1962.

W. G. Rees. *Interaction of electromagnetic radiation with matter*, page 42–109. Cambridge University Press, 3 edition, 2012. doi: 10.1017/CBO9781139017411.004.

M. Reichstein, M. Bahn, P. Ciais, D. Frank, M. D. Mahecha, S. I. Seneviratne, J. Zscheischler, C. Beer, N. Buchmann, D. C. Frank, et al. Climate extremes and the carbon cycle. *Nature*, 500:287–295, 2013.

O. Reitebuch. The spaceborne wind lidar mission adm-aeolus. In *In: Schumann, U. (eds) Atmospheric physics: Background–methods–trends*, pages 815–827. Springer Berlin, Heidelberg, 2012. URL `https://doi.org/10.1007/978-3-642-30183-4`.

L. A. Remer, A. B. Davis, S. Mattoo, R. C. Levy, O. V. Kalashnikova, O. Coddington, J. Chowdhary, K. Knobelspiesse, X. Xu, Z. Ahmad, E. Boss, B. Cairns, H. M. Dierssen, D. J. Diner, B. Franz, R. Frouin, B.-C. Gao, A. Ibrahim, J. V. Martins, A. H. Omar, O. Torres, F. Xu,

and P.-W. Zhai. Retrieving aerosol characteristics from the pace mission, part 1: Ocean color instrument. *Frontiers in Earth Science*, 7:152, 2019.

C. D. Rodgers. *Inverse methods for atmospheric sounding: theory and practice*. World scientific, 2000.

R. A. Rohde, 2013. URL `https://en.wikipedia.org/wiki/Solar_irradiance#/media/File:Solar_spectrum_en.svg`. Latest acess 10/01/2024.

M. Rossini, M. Celesti, G. Bramati, M. Migliavacca, S. Cogliati, U. Rascher, and R. Colombo. Evaluation of the Spatial Representativeness of In Situ SIF Observations for the Validation of Medium-Resolution Satellite SIF Products. *Remote Sensing*, 14(20):5107, Oct 2022. ISSN 2072-4292. doi: 10.3390/rs14205107. URL `https://www.mdpi.com/2072-4292/14/20/5107`.

N. Sabater, J. Vicent, L. Alonso, J. Verrest, and J. Moreno. An atmospheric correction algorithm for the FLEX/S3 tandem mission. *5th International workshop on remote sensing of vegetation fluorescence*, -:6, 2014.

N. Sabater, J. Vicent, L. Alonso, S. Cogliati, J. Verrelst, and J. Moreno. Impact of atmospheric inversion effects on solar-induced chlorophyll fluorescence: Exploitation of the apparent reflectance as a quality indicator. *Remote Sensing*, 9(6), 2017. ISSN 2072-4292. doi: 10.3390/rs9060622. URL `https://www.mdpi.com/2072-4292/9/6/622`.

S. Sanghavi, J. Martonchik, J. Landgraf, and U. Platt. Retrieval of the optical depth and vertical distribution of particulate scatterers in the atmosphere using o 2 a-and b-band sciamachy observations over kanpur: a case study. *Atmospheric Measurement Techniques*, 5(5):1099–1119, 2012.

P. J. Sellers, D. S. Schimel, B. Moore, J. Liu, and A. Eldering. Observing carbon cycle–climate feedbacks from space. *Proceedings of the National Academy of Sciences*, 115(31):7860–7868, Jul 2018. doi: 10.1073/pnas.1716613115. URL `https://www.pnas.org/doi/full/10.1073/pnas.1716613115`. Publisher: PNAS.

B. Siegmann, L. Alonso, M. Celesti, S. Cogliati, R. Colombo, A. Damm, S. Douglas, L. Guanter, J. Hanuš, K. Kataja, T. Kraska, M. Matveeva, J. Moreno, O. Muller, M. Pikl, F. Pinto, J. Quirós Vargas, P. Rademske, F. Rodriguez-Morene, N. Sabater, A. Schickling, D. Schüttemeyer, F. Zemek, and U. Rascher. The High-Performance Airborne Imaging Spectrometer HyPlant—From Raw Images to Top-of-Canopy Reflectance and Fluorescence Products: Introduction of an Automatized Processing Chain. *Remote Sensing*, 11(23):2760, 2019. ISSN 2072-4292. doi: 10.3390/rs11232760. URL `https://www.mdpi.com/2072-4292/11/23/2760`.

A. F. Stein, R. R. Draxler, G. D. Rolph, B. J. B. Stunder, M. D. Cohen, and F. Ngan. NOAA's HYSPLIT Atmospheric Transport and Dispersion Modeling System. *Bulletin of the American*

Meteorological Society, 96(12):2059–2077, December 2015. ISSN 0003-0007, 1520-0477. URL `https://journals.ametsoc.org/doi/10.1175/BAMS-D-14-00110.1`.

A. J. Tatem, S. J. Goetz, and S. I. Hay. Fifty Years of Earth-observation Satellites. *American Scientist*, 96(5):390, 2008. ISSN 0003-0996, 1545-2786. doi: 10.1511/2008.74.390. URL `https://www.americanscientist.org/article/fifty-years-of-earth-observation-satellites`.

K. J. Thome, J. S. Czapla-Myers, and S. F. Biggar. Vicarious calibration of aqua and terra modis. In *Earth Observing Systems VIII*, volume 5151, pages 395–405, 2003.

O. Torres, C. Ahn, and Z. Chen. Improvements to the omi near uv aerosol algorithm using a-train caliop and airs observations. *Atmospheric Measurement Techniques*, 6(3):3257–3270, 2013.

S. Twomey, H. Jacobowitz, and H. Howell. Matrix methods for multiple-scattering problems. *Journal of Atmospheric Sciences*, 23(3):289–298, 1966.

U. N. F. C. o. C. C. UNFCCC. The paris agreement - what is the paris agreement?, 2016. URL `https://unfccc.int/process-and-meetings/the-paris-agreement`. Last acess: 08/01/2024.

S. Van Wittenberghe, N. Sabater, M. P. Cendrero-Mateo, C. Tenjo, A. Moncholi, L. Alonso, and J. Moreno. Towards the quantitative and physically-based interpretation of solar-induced vegetation fluorescence retrieved from global imaging. *Photosynthetica*, 59(SPECIAL IS-SUE):438–457, 2021. ISSN 03003604, 15739058. doi: 10.32615/ps.2021.034. URL `http://ps.ueb.cas.cz/doi/10.32615/ps.2021.034.html`.

J. Veefkind, I. Aben, K. McMullan, H. Förster, J. de Vries, G. Otter, J. Claas, H. Eskes, J. de Haan, Q. Kleipool, M. van Weele, O. Hasekamp, R. Hoogeveen, J. Landgraf, R. Snel, P. Tol, P. Ingmann, R. Voors, B. Kruizinga, R. Vink, H. Visser, and P. Levelt. Tropomi on the esa sentinel-5 precursor: A gmes mission for global observations of the atmospheric composition for climate, air quality and ozone layer applications. *Remote Sensing of Environment*, 120: 70–83, 2012. ISSN 0034-4257. URL `https://doi.org/10.1016/j.rse.2011.09.027`.

J. Vidot and E. Borbas. Land surface VIS/NIR BRDF atlas for RTTOV-11: model and validation against SEVIRI land SAF albedo product. *Quarterly Journal of the Royal Meteorological Society*, 140(684):2186–2196, 2014. ISSN 00359009. URL `http://doi.wiley.com/10.1002/qj.2288`.

U. Wandinger, A. A. Floutsi, H. Baars, M. Haarig, A. Ansmann, A. Hünerbein, N. Docter, D. Donovan, G.-J. van Zadelhoff, S. Mason, and J. Cole. Heteac – the hybrid end-to-end aerosol classification model for earthcare. *Atmospheric Measurement Techniques*, 16(10): 2485–2510, 2023. doi: 10.5194/amt-16-2485-2023. URL `https://amt.copernicus.org/articles/16/2485/2023/`.

P. J. Werdell, M. J. Behrenfeld, P. S. Bontempi, E. Boss, B. Cairns, G. T. Davis, B. A. Franz, U. B. Gliese, E. T. Gorman, O. Hasekamp, K. D. Knobelspiesse, A. Mannino, J. V. Martins, C. R. McClain, G. Meister, and L. A. Remer. The Plankton, Aerosol, Cloud, Ocean Ecosystem Mission: Status, Science, Advances. *Bulletin of the American Meteorological Society*, 100(9):1775–1794, 2019. ISSN 0003-0007, 1520-0477. doi: 10.1175/BAMS-D-18-0056.1. URL `https://journals.ametsoc.org/view/journals/bams/100/9/bams-d-18-0056.1.xml`.

J. Wevers, D. Müller, G. Kirches, R. Quast, and C. Brockmann. IdePix for Sentinel-3 OLCI Algorithm Theoretical Basis Document. Technical report, Brockmann Consult GMBH, 2022. URL `https://zenodo.org/record/6517333`. Publisher: Zenodo.

D. M. Winker, M. A. Vaughan, A. Omar, Y. Hu, K. A. Powell, Z. Liu, W. H. Hunt, and S. A. Young. Overview of the calipso mission and caliop data processing algorithms. *Journal of Atmospheric and Oceanic Technology*, 26(11):2310 – 2323, 2009. URL `https://doi.org/10.1175/2009JTECHA1281.1`.

W. J. Wiscombe. Improved mie scattering algorithms. *Applied optics*, 19(9):1505–1509, 1980.

X. Wu, Q. Xiao, J. Wen, D. You, and A. Hueni. Advances in quantitative remote sensing product validation: Overview and current status. *Earth-Science Reviews*, 196:102875, Sep 2019. ISSN 00128252. doi: 10.1016/j.earscirev.2019.102875. URL `https://linkinghub.elsevier.com/retrieve/pii/S001282521830151X`.

X. Wu, J. Wen, R. Tang, J. Wang, Q. Zeng, Z. Li, D. You, X. Lin, B. Gong, and Q. Xiao. Quantification of the uncertainty in multiscale validation of coarse-resolution satellite albedo products: A study based on airborne CASI data. *Remote Sensing of Environment*, 287:113465, Mar 2023. ISSN 00344257. doi: 10.1016/j.rse.2023.113465. URL `https://linkinghub.elsevier.com/retrieve/pii/S0034425723000160`.

X. Xu, J. Wang, Y. Wang, and A. Kokhanovsky. Passive remote sensing of aerosol height. In *Remote Sensing of Aerosols, Clouds, and Precipitation*, pages 1–22. Elsevier, 2018.

X. Xu, J. Wang, Y. Wang, J. Zeng, O. Torres, J. S. Reid, S. D. Miller, J. V. Martins, and L. A. Remer. Detecting layer height of smoke aerosols over vegetated land and water surfaces via oxygen absorption bands: hourly results from epic/dscovr in deep space. *Atmospheric Measurement Techniques*, 12(6):3269–3288, 2019.

H. Yu, Q. Tan, L. Zhou, Y. Zhou, H. Bian, M. Chin, C. L. Ryder, R. C. Levy, Y. Pradhan, Y. Shi, Q. Song, Z. Zhang, P. R. Colarco, D. Kim, L. A. Remer, T. Yuan, O. Mayol-Bracero, and B. N. Holben. Observation and modeling of the historic "Godzilla" African dust intrusion into the Caribbean Basin and the southern US in June 2020. *Atmospheric Chemistry and Physics*, 21 (16):12359–12383, August 2021. ISSN 1680-7316. doi: 10.5194/acp-21-12359-2021. URL `https://acp.copernicus.org/articles/21/12359/2021/`.

Z.-C. Zeng, S. Chen, V. Natraj, T. Le, F. Xu, A. Merrelli, D. Crisp, S. P. Sander, and Y. L. Yung. Constraining the vertical distribution of coastal dust aerosol using oco-2 o2 a-band measurements. *Remote Sensing of Environment*, 236:111494, 2020. ISSN 0034-4257. URL `https://doi.org/10.1016/j.rse.2019.111494`.

List of Figures

List of Tables

Acronyms

1Dvar 1 dimensional variational approach.

AATSR Advanced Along-Track Scanning Radiometer.

ADA Azimuth difference angle.

AERONET Aerosol Robotic Network.

AFGL Air Force Geophysical Laboratory.

ALH Aerosol layer height.

AOD Aerosol optical depth.

AOT Aerosol optical thickness.

ASTER Advanced Spaceborne Thermal Emission Reflection Radiometer.

ATCOR Atmospheric and Topographic Correction algorithm.

AZI Azimuth difference angle.

BOA Bottom of atmosphere.

BRDF Bidirectional reflectance distribution function.

C3S Copernicus Climate Change Service.

CALIOP Cloud-Aerosol Lidar with Orthogonal Polarization.

CALIPSO Cloud-Aerosol Lidar and Infrared Pathfinder Satellite Observations.

CAMS Copernicus Atmospheric Monitoring Service.

CCD Charge-coupled device.

CEMS Copernicus Emergency Management Service.

CGASA Coefficients of Gas Absorption.

CLMS Copernicus Land Monitoring Service.

CMEMS Copernicus Marine Environmental Monitoring Service.

CO2 Carbon dioxide.

CSS Copernicus Security Service.

DOAS Differential optical absorption spectroscopy.

DSCOVR Deep Space Climate Observatory.

ECMWF European Centre for Medium-Range Weather Forecasts.

ENVISAT Environmental Satellite.

EPIC Earth Polychromatic Imaging Camera.

ESA European Space Agency.

EUMETSAT European Organisation for the Exploitation of Meteorological Satellite.

FLEX Fluorescence Explorer.

FLORIS Fluorescence Imaging Spectrometer.

FLOX Fluorscence box.

FWHM Full width at half maximum.

GMES Global Monitoring for Environment and Security.

GOME-2 Global Ozone Monitoring Experiment-2.

HETEACT Hybrid End-To-End Aerosol Classification model for EarthCARE.

HITRAN High-resolution transmission molecular absorption database.

HyPlant High-Performance Airborne Imaging Spectrometer.

IDEPIX Identification of Pixel.

L1 Level 1.

LIDAR Light detection and ranging instrument.

LUT Look-up table.

MERIS Medium Resolution Imaging Spectrometer.

MODIS Moderate Resolution Imaging Spectroradiometer.

MODTRAN MODerate resolution atmospheric TRANsmission.

MOMO Matrix operation model.

NASA National Aeronautics and Space Administration.

NDVI Normalized difference vegetation index.

NIR Near infrared.

NOAA National Oceanic and Atmospheric Administration.

O2 Oxygen.

OCI Ocean Colour Instrument.

OCO-2 Orbiting Carbon Observatory 2.

OHP Haute-Provence Observatory.

OLCI Ocean and Land Colour Imager.

OLCI-FLEX Ocean and Land Color imager in FLEX configuration.

OMI Ozone monitoring instrument.

OPAC Optical Properties of Aerosols and Clouds.

PACE Plankton, Aerosol, Cloud, ocean Ecosystem.

PCR Principle component regression.

POLDER PoLarization and Directionality of the Earth's Reflectances.

RA-2 Radar Altimeter-2.

RADAR Radio detection and ranging instrument.

RadCalNet Radiometric Calibration Network.

RGB True colour image.

RSR Relative spectral response function.

RTE Radiative transfer equation.

S3 Sentinel-3.

S5P Sentinel-5P.

SABS strong absorbing aerosol.

SCIMACHY Scanning Imaging Absorption Spectrometer for Atmospheric Chartography.

SCOPE Soil Canopy Observation of Photosynthesis and Energy fluxes model.

SFM Spectral Fitting Method.

SIF Sun-induced fluorescence.

SLSTR Sea and Land Surface Temperature Radiometer.

SNAP Sentinel Application Platform.

SRAL Radar altimeter, microwave radiometer.

SSA single scattering albedo.

SZA Sun zenith angle.

TOA Top of atmosphere.

TOC Top of canopy.

TROPOMI Tropospheric Monitoring Instrument.

USGS United States Geological Survey.

UTC Coordinated Universal Time.

VIIRS Visible Infrared Imaging Radiometer Suite.

VZA Viewing zenith angle.

wvl Wavelength.

Acknowledgement

Ich möchte mich ganz herzlich bei Herrn Prof. Dr. Jürgen Fischer für die Betreuung und Begutachtung meiner Doktorarbeit bedanken. Nur durch sein Vertrauen in meine Fähigkeiten und sein Angebot für eine Anstellung als wissenschaftliche Mitarbeiterin in seiner Arbeitsgruppe habe ich die Herausforderung einer Promotion angenommen. Unsere fachlichen Diskussionen haben zum Gelingen dieser Arbeit beigetragen. Meinem Zweitgutachter, Prof. Dr. Fabian Fassnacht, möchte ich für die Übernahme dieser Aufgabe und der unkomplizierten, schnellen und angenehmen Kommunikation danken.

Ein besonderer Dank gilt Rene Preusker, der mir während meiner gesamten Zeit als Doktorandin immer mit Rat und Tat zur Seite stand. Ich danke ihm für unsere inspirienden Gespräche, die fachlichen Diskussionen und für seine ausführlichen und zielführenden Kommentare zum Inhalt dieser Arbeit. Auch alle anderen Kollegen haben mir durch unsere Diskussionen in unserem wöchentlichen Seminar oder bei Gesprächen auf dem Flur sehr geholfen. Vielen Dank für die angenehme Arbeitsatmosphäre, die ihr geschaffen habt durch gemeinsames Tischtennis oder Darts spielen und natürlich unserer gemeinsamen Mittagessen. Insbesondere möchte ich mich bei Nicole bedanken, die mit mir ihre Aerosol-Expertise geteilt hat und die mich immer wieder ermutigt und aufgebaut hat. Vielen Dank an Jan für den unermütlichen Technik-Support und vor allem für seine Python-Skripte zur Georeferenzierung, zur Erstellung von RGBs und zum Einlesen von Daten. Ich konnte auch stark von Cintias Erfahrungen als Post-Doc profitieren, die mich immer motiviert hat, meine Arbeit zu veröffentlichen und mich bestärkt hat, dass meine Doktorarbeit fertig werden wird. Außerdem bedanke ich mich bei allen, die Teile und die ganze Arbeit gelesen haben, für die wertvollen Kommentare.

Abschließend möchte ich mich bei meiner Familie bedanken, die mich während meines gesamten Studiums unterstützt hat und mir stets ihr vollstes Vertrauen zugesprochen hat. Von ganzem Herzen möchte ich mich bei Fabi bedanken, der in dieser intensiven Zeit als Doktorandin immer an meiner Seite war. Er hat immer an mich geglaubt, mich motiviert, mich bestärkt, geduldig meine Ergebnisse bestaunt und mich abgelenkt, wenn ich eine Pause brauchte.